EXPERIMENTAL INVESTIGATION OF A VIBRATING AXIAL TURBINE CASCADE IN PRESENCE OF UPSTREAM GENERATED AERODYNAMIC GUSTS

THÈSE N^{O} 2758 (2003)

PRÉSENTÉE À LA FACULTÉ DES SCIENCES ET TECHNIQUES DE L'INGÉNIEUR

SECTION DE GÉNIE MÉCANIQUE

ÉCOLE POLYTECHNIQUE FÉDÉRALE DE LAUSANNE

POUR L'OBTENTION DU GRADE DE DOCTEUR ÈS SCIENCES TECHNIQUES

PAR

Fabrice ROTTMEIER

ingénieur mécanicien diplômé EPF
de nationalité suisse et originaire de Märstetten (TG)

acceptée sur proposition du jury:

Prof. A. Bölcs, directeur de thèse
Prof. R. Ainsworth, rapporteur
Prof. F. Avellan, rapporteur
Prof. T. Fransson, rapporteur

Lausanne, EPFL
2003

ACKNOWLEDGEMENTS

This work was conducted during my employment at the Laboratoire de Thermique Appliqueé et de Turbomachines (LTT), École Polytechnique Fédérale de Lausanne (EPFL) under the direction of Professor Albin Bölcs. I would like to begin by thanking him for his support, encouragements and the high-level of confidence he provided me; even after his retirement.

This dissertation is “the cherry on the cake” of my work as task leader at EPFL of the challenging european project “Aeromechanical Design of Turbine Blades”. It has been a great pleasure to work in collaboration with people from around Europe, with different technical backgrounds, and all working at a high research level, either in the industry or in leading european universities. Exchanges and discussions between the partners have become very fruitful, both on a technical and on a human level, creating a strong team spirit. I would like to thank all partners for it and wish them all good luck on the follow-up programme. Special thanks go to: Jeff Green, coordinator of the project for his great work; Dr. Holger Hennings for proofing this dissertation and for sharing his great experience in experimental research in turbomachines with me; Dr. Joachim Belz for his technical advice; Professor Torsten Fransson for his expertise in aeroelasticity; Professor Rodger Ainsworth for his collaboration in unsteady wake measurements, his encouragements and his great sense of humor; Dr. Gerhard Kahl for his support and Dr. Markus Jöcker for maintaining a common database, the heart of effective results utilization. As the only non-european partner involved in this european programme, the financial support of the Swiss Federal Office for Education and Science is gratefully acknowledged. Hopefully, this will not be necessary in the near future!

Next, I would like to offer my most sincere gratitude to all the research technicians who made this experimental investigation possible. It has been a fruitful collaboration that has led to a modern and unique test facility they can be really proud of. Special thanks go to: Pascale Zbinden for his important contributions on the fabrication of the measuring cascade and his passion for research and computer-assisted machining (*I am still really impressed by the complicated programming he has been doing at home on the week-ends*); Jean-Pierre “Fifi” Mottier for the fabrication of the steady aerodynamic probes and blade instrumentations; Jean-Pierre “ouuuuais!” Rudaz for his contributions, Urbano “Polo” Polongini for welding the mainframe of the test facility, always with joy; Christophe “Cri-cri” Zurmühle for the good laughs we had working together and the good job he has been doing in maintaining the test facility, and finally, Jean-Pierre “jipi” Rougnon for his effective work with a funky attitude. Thanks guys!

It was also a great pleasure to work with engineers and post-docs at the LTT or in other labs. A few individuals deserve a special mention for their contributions in this work: Matt “Master” Nowinski for teaching me all he knew about the non-rotating annular test facility, the measuring technique and for opening my ears to “the only real funk” (*I was a little disappointed when you joined “Asses Anonymous” and published your scanned portrait on the web: kids do stare at the moon, bro.!*); Bernd “deux-dents” Hagenah for assisting me on this project and for all the visual jokes that he made during the incredibly loud measurements; Dr. Philippe “Pino” Muellhaupt for his expertise in signal processing and for sharing his toys (nonlinear differential equations, the “toy-copter”,...); Gregory “Cooling Mac Greg” Vogel for his availability (24/7), for changing his religion from Mac to PC, for his great knowledge of Labview and for showing all the new electronic gadgets he purchased before their official release

in Europe; Arrigo “9 mm” Beretta for being a fast learning assistant who is always available (*the follow-up project is in good hands, Minime!*) and finally Annick Despont, our secretary, who has efficiently swept away administrative tasks from my path with a smile.

I would also like to thank the members of my thesis defence committee. Their sincere encouragements have really touched me.

The final version of this thesis has been reviewed by an international spell-checking consortium I would like to thank: Lauren Woolf from South Africa, Douglas Robinson from the U.S. and Klaus Hubrich from Germany for writing the german abstract.

Moving to more personal acknowledgments, I would like to thank my family and my friends for their support. My wife, Sylvie, deserves all my gratitude for following me to Switzerland, finding a job and for giving birth to our beloved daughter Manon. I love you girls!

This dissertation is dedicated to my uncle, Jacques Huguenin-Dumittan, who passed away during summer 2002. He didn’t have the chance I had in having a stable and enriching environment in which to grow up and the opportunity to carry on studies as I did. Nevertheless, he was a cheerful chap whom I still miss!

That’s all folks!

The experimental data used in this thesis was acquired in the research programme ADTurB, funded by the European Community under the Industrial and Material Technologies Programme (BriteEuRam III), contract no. BPR-CT95-0124. The permission to publish is gratefully acknowledged.

ABSTRACT

An experimental investigation has been conducted in the non-rotating annular test facility of the “Laboratoire de Thermique Appliquée et de Turbomachines” (LTT), “École Polytechnique Fédérale de Lausanne” (EPFL). During this investigation, the unsteady aerodynamic response of a turbine cascade was investigated for three different cases: (1) the clamped blades subjected to periodic, upstream generated aerodynamic gusts, (2) the cascade forced to vibrate in the travelling wave mode in a uniform flow, and (3) the cascade forced to vibrate in the presence of the upstream generated aerodynamic gusts, with a common excitation frequency and a constant gust-vibration phasing. These measurements were aimed at identifying important aspects of the unsteady aeroelastic behavior of the blades. Particular attention was focused on the relationship between the time-dependent flows of (1) and (2) and that of (3) in an effort to better understand aerodynamic forced response phenomena in turbomachinery.

The experimental tasks detailed above have been performed in a non-rotating annular test facility using a test rig composed of rotating wake generators and a fixed turbine cascade. There are two rotating wake generators: one possesses 13 elliptical struts and the other has 22. Each one is designed to generate wake profiles similar to a blade row. The turbine cascade consist of 20 blades attached to separate torsion suspension system, with a magnetic excitation feature, allowing the control of the cascade’s vibration mode. Several blades are instrumented to measure the resulting surface steady pressures, unsteady pressures and blade vibration mode.

The specific objectives of this investigation were:

- measure the unsteady aerodynamic blade response to: (1) imposed cascade vibration modes (travelling wave mode), (2) upstream generated aerodynamic gusts, and (3) combinations of these two effects.
- using the above experimental results, address the local validity of the assumptions inherent in linearized treatments of the forced response problem. Specifically, can the local unsteady blade loading be considered as a linear superposition of the unsteady forces derived individually from the cascade’s vibration mode and from the aerodynamic gusts?

The final conclusions of this work were:

- the simultaneous measurements have demonstrated the important influence of the gust-vibration phase angle Φ on the blade surface time-dependent pressure distribution and has identified it as the key parameter. For a given test configuration and flow condition, the selection of the gust-vibration phase angle allows a local constructive or destructive interaction between the main harmonics of both excitation sources. Generally, this suggest that the gust-vibration phase angle has an important effect on the excitation levels and excited modes of the cascade. The practical implication of this phenomenon is that the judicious choice of a gust-vibration phase angle can diminish significantly the aerodynamic excitation levels for a given cascade vibration mode, flow condition and test configuration of a single stage. It is even possible that certain periodic variations of this phase angle produces another excitation source in turbomachinery.

- the simultaneous vibrating cascade and upstream generated aerodynamic gusts excitations can be accurately predicted by the linear superposition of the individual gust-induced and vibration-induced unsteady flow fields. This principle was shown to be applicable locally for various test configurations, including different engine orders, inter-blade phase angles, gust-vibration phase angles, and flow conditions. The only significant discrepancies were observed in the presence of shocks, but these were limited to a localized region reducing their importance in terms of the overall unsteady aerodynamic loading of the blade. It has been shown that these discrepancies were mainly due to the variation of the shock's mean location between gust-response only, controlled-vibration only and simultaneous measurements. The main practical advantage of this linear superposition principle is that the numerical and experimental investigation of the aerodynamic forced response problem can be separated into: (1) the identification of the local forcing-function due to upstream generated gusts only, (2) a local aerodynamic stability analysis of the cascade alone.
- The simultaneous measurements have shown that measurement errors vary significantly as the local pressure disturbance contributions due to the gusts and the cascade's vibration mode interact constructively or destructively. Particular attention is needed in simultaneous measurements in order to separate measurement error effects and physical phenomena.

RÉSUMÉ

Dans le stand annulaire du “Laboratoire de Thermique Appliquée et de Turbomachines” (LTT) de “l'Ecole Polytechnique Fédérale de Lausanne” (EPFL), une série de mesures expérimentales dans le domaine de l'aéroélasticité a été réalisée. Lors de cette dernière, la réponse aérodynamique instationnaire d'une grille d’aubes de turbine a été étudiée dans trois cas distincts: (1) la grille d’aube fixes a été soumise au passage périodique de sillages amonts (2) la grille d’aubes a été mise en vibration de manière contrôlée (modes “d’onde tournante”) dans un écoulement uniforme, et finalement (3) les aubes, forcées à vibrer, ont été soumises en plus au passage des sillages amonts avec une fréquence d'excitation commune et un déphasage constant entre ces deux sources d'instabilités; le but de ces essais étant d'identifier les effets aéroélastiques de ce type de grille. Un soin tout particulier a été apporté à l'étude de la relation entre les écoulements instationnaires des cas (1) et (2), ainsi qu'à l'étude de leur combinaison (3), avec le dessein de mieux comprendre le phénomène aérodynamique de réponse forcée dans les turbomachines.

Les mesures expérimentales associées aux essais sus-mentionnées ont été réalisées dans un stand d’essai annulaire non-rotatif à l’aide de générateurs de sillages tournants et d’une grille d’aubes de turbine fixe. Les générateurs de sillages consistent en un assemblage de 13, respectivement 22 barres elliptiques conçues de manière à génerer des sillages similaires à un grille d’aubes directrices. La grille d’aubes de turbine est composée de 20 aubes possédant chacun un mécanisme de suspension en combinaison avec un système d’excitation magnétique, permettant ainsi le contrôle du mode vibratoire de la grille d’aubes.

Les objectifs détaillés de ce travail de recherche ont été:

- de mesurer la réponse aérodynamique instationnaire de l’aubage due: (1) au passage de sillages amonts, (2) à la vibration forcée de la grille d’aubes dans des modes “d’onde tournante”, (3) à la présence simultanée de ces deux effets.
- à partir des résultats susmentionnées, de vérifier la validité des hypothèses inhérentes à la linéarisation du problème de réponse forcée. Plus spécifiquement: Est-ce que la réponse forcée locale et combinée d’une aube (3) peut être considérée comme la superposition linéaire des forces aérodynamiques instationnaires issues séparément de la vibration de la grille d’aubes (2) et du passage de sillages amonts (1)?

Les conclusions de ce travail de recherche sont:

- les mesures simultanées ont démontré l’importante influence de l’angle de phase Φ, défini entre les deux sources d’excitations aérodynamiques, sur la distribution de la pression instationnaire sur l’aubage, et l’ont identifié comme paramètre-clé. Dans des conditions d’écoulement et une configuration données, le choix de cet angle de phase permet d’obtenir localement une interaction constructive ou destructive entre les premières harmoniques de chacune de ces sources d’excitation aérodynamique. En général, cela suggère que cet angle de phase a un effet important sur les niveaux d’excitations et sur les modes excités de la grille d’aubes mobile d’un étage axial. Il est même envisageable que des variations périodiques de cet angle de phase produisent une nouvelle source d’excitation aérodynamique combinée. Pratiquement, l’avantage de ce phénomène est que le

choix judicieux de cet angle de phase peut permettre une diminution significative des niveaux d'excitations aérodynamiques pour un mode vibratoire, des conditions d'écoulement et une configuration donnés.

- L'excitation simultanée de l'aubage au passage des sillages amonts et à la vibration de la grille d'aubes peut être prédite de manière très précise par la superposition linéaire des champs d'écoulement instationnaires produit isolement par le passage des sillages amonts et, respectivement par la vibration de la grille d'aubes. Ce principe de superposition linéaire a été démontré localement pour un grand nombre de configurations, comprenant la variation de l'ordre d'excitation, la variation de l'angle de phase inter-aubes, la variation de l'angle de phase entre les deux sources d'excitation, ainsi que la variation des conditions d'écoulement. Les seules limitations significatives de ce principe furent constatées en présence de fort chocs. Néanmoins, dans ces cas, les erreurs de prévisions furent limitées à des zones très localisées, n'influençant ainsi que faiblement la charge aérodynamique instationnaire globale. L'analyse de ces erreurs a montré que la variation de la position moyenne du choc entre les mesures de réponse aux sillages, les mesures de réponse à la vibration des aubes et les mesures combinant ces deux effets, est leur source principale. Pratiquement, le principe de superposition linéaire de ces deux sources d'excitations permet une étude, numérique ou expérimentale, séparée de ces deux phénomènes: (1) identification des forces d'excitation locales dues au passage de sillages amonts sur une grille fixe, (2) une analyse de la stabilité aérodynamique de la grille d'aube isolée.
- Les mesures simultanées ont montré que les erreurs de mesures varient de manière importante en fonction de l'interaction constructive ou destructive des pressions fluctuantes générées par les sillages et le mode vibratoire de la grille d'aubes. Dans les mesures simultanées, une attention particulière est nécessaire pour séparer les phénomènes physiques des effets d'erreurs de mesures.

ZUSAMMENFASSUNG

Die vorliegende Arbeit beschäftigt sich mit einer experimentellen Untersuchung im Ringgitterprüfstand (RGP 400 SE) des “Laboratoire de Thermique Appliquée et de Turbomachines” (LTT) der Eidgenössischen Technischen Hochschule Lausanne (EPFL).

Ziel der Studie ist die Untersuchung der instationären aerodynamischen Antwort eines Turbinengitters für drei unterschiedliche Konfigurationen: (1) fixierte Schaufeln, die einer stromaufwärts erzeugten aerodynamischen Störung ausgesetzt werden, (2) das Schaufelgitter wird bei ungestörter Strömung zu einer periodischen Schwingung zwangsbewegt (3) und das Schaufelgitter wird zu einer periodischen Schwingung bei gleichzeitiger Präsenz einer stromaufwärts erzeugten aerodynamischen Störung gleicher Frequenz zwangsbewegt, wobei die Phasenlage Störung - Schwingung konstant gehalten wird. Das Ziel dieser Messungen war die Untersuchung des instationären aeroelastischen Verhaltens des Gitters mit seinen Schaufeln. Im Rahmen dieser Untersuchung wurde insbesondere der Zusammenhang zwischen der zeitabhängigen Strömung der Konfigurationen (1) und (2) und deren Kombination (3) untersucht.

Die oben angeführte Untersuchung wurde in einem nichtrotierenden Ringgitterprüfstand, bestehend aus einem rotierenden Nachlaufgenerator und dem eigentlichen stehenden Turbinengitter, durchgeführt. Es kamen zwei unterschiedliche Nachlaufgeneratoren mit 13 und 22 elliptischen Streben, die jeweils einen für eine Schaufelreihe repräsentativen Nachlauf erzeugen, zum Einsatz. Das Turbinegitter besteht aus zwanzig einzeln gelagerten Schaufeln, die mittels eines magnetischen Anregungsmechanismuses in kontrollierte Schwingungen versetzt werden können. Um detaillierte Informationen über die Zusammenwirkung der oben beschriebenen Effekte zu erhalten, wurden die Turbinenschaufeln teilweise mit statischen Druckbohrungen, instationären Druckaufnehmern und mit Beschleunigungsaufnehmern zur Bestimmung der Schwingungsform instrumentiert.

Die spezielle Zielsetzung für die Untersuchung war:

- Messung der instationären Schaufelantwort bei (1) stromaufwärts erzeugten aerodynamischen Störungen, (2) zwangserregten Schaufelschwingungen, und (3) der Kombination dieser beiden Effekte.
- Beantwortung der Frage, ob die getroffenen Annahmen bei einer linerarisierten Behandlung des Zwangserregungsproblems Gültigkeit haben. Hierbei wird insbesondere die Annahme, ob die Gesamtantwort der Zwangsanregung (3) durch eine linearisierte Überlagerung der individuellen instationären Belastung durch Schaufelschwingung (2) und aerodynamischer Störung (1), betrachtet.

Die Schlussfolgerungen dieser Arbeit sind insbesondere:

- Die simultanen Messungen zeigen den außerordentlichen Einfluß des Phasenwinkels zwischen aerodynamischer Störung und Schwingung auf die zeitabhängige Druckverteilung an der Schaufeloberfläche, und haben diesen Winkel als Hauptparameter zur Beschreibung dieses Problems identifiziert. Die Wahl dieses Phasenwinkels erlaubt für eine gegebene Strömungsbedingung und Testkonfiguration lokal ein additives oder subtraktives Zusammenwirken zwischen den 1. Harmonischen beider Erregerquellen. Im allgemeinen heißt das, dass der Phasenwinkel Störung - Schwingung entscheidenden Einfluß auf den

Anregungsgrad und -moden des Gitters hat. Die praktische Folge dieses Phänomens ist, dass durch eine geeignete Wahl dieses Phasenwinkels der aerodynamische Anregungsgrad für gegebene Gitterschwingungsform, Strömungs- und Testbedingungen signifikant abgesenkt werden kann. Es wäre somit auch vorstellbar, dass bestimmte periodische Variationen dieses Phasenwinkels als neue Anregungsquelle in Turbomaschinen wirken könnten.

- Durch lineare Superposition des störungsinduzierten und des schwingungsinduzierten instationären Strömungsfeldes lässt sich das Strömungsfeld unter Einfluß beider Effekte genau vorhersagen. Dieses Prinzip der linearen Überlagerung wurde auf unterschiedliche Testfälle mit variierender Anregungsordnung, unterschiedlichen Phasendifferenzwinkeln zwischen den Schaufeln, unterschiedlichen Phasenlagen von aerodynamischer Störung zu Schaufelschwingung und für verschiedene Strömungsbedingungen erfolgreich bestätigt. Eine Einschränkung für die generelle Anwendbarkeit der linearen Superposition betrifft die Überlagerung im Bereich von Verdichtungsstößen. Da hier aber nur die lokale Übereinstimmung der Ergebnisse betroffen ist, die hauptsächlich durch eine unterschiedliche mittlere Stosslage zwischen den Messungen mit aerodynamischer Störung (1), periodischer Schwingung (2) und, Überlagerung von (1) und (2) hervorgerufen wird, kann deren Bedeutung für die globale aerodynamische Last vernachlässigt werden. Das Verfahren der linearen Superposition vereinfacht somit die Behandlung des Problems der aerodynamischen Zwangserregung für den numerischen und experimentellen Bereich durch die Aufspaltung in zwei einfach zu behandelnde Probleme: (1) Bestimmung der lokalen Anregung durch stromaufwärts erzeugte aerodynamische Störungen, (2) eine lokale aerodynamische Stabilitätsanalyse des isolierten Gitters.
- Die simultanen Messungen zeigen, dass die Messfehler je nach additiver oder subtraktiver Wechselwirkung von Nachläufen und Schwingungsform stark variieren können. Somit muß bei simultanen Messungen den Fehlereinflussmöglichkeiten besondere Beachtung geschenkt werden, um die physikalischen Effekte in der Strömung von Messfehlern unterscheiden zu können.

TABLE OF CONTENTS

0.1 Nomenclature

Abbreviations

CFD	computational fluid dynamics
CV	controlled vibration
DAQ	data acquisition
EO	engine order
FFT	fast Fourier transform
FS	full scale
GR	gust response
HCF	high cycle fatigue
IBPA	inter-blade phase angle (definition in Figure 46 on page 88)
LE	leading edge of a blade
LEO	low engine order
PS	pressure side of a lifting surface
SB	single blade vibration experiment
SS	suction side of a lifting surface
TE	trailing edge of a blade
TF	transfer function
TTL	transistor-transistor logic
TW	travelling wave vibration mode
UPT	unsteady pressure transducer

Latin

A	amplitude of a signal	
C_t	center of torsion	
C_g	center of gravity	
G(s)	transfer function	
L	influence coefficient (complex)	
M	Mach number	
N	total number of blades assembled on the cascade	
R	cross-correlation	
$\vec{R}$	vector from center of torsion to a blade surface location	
S	signal	
T	temperature	[K]
U	velocity	[m/s]
U(s)	discrete input in the frequency domain	
X, Y	discrete time signals	
Y(s)	discrete output signal in frequency domain	
a,b,c,d,e,f	complex parameters	
a	main length of elliptical strut	[m]
b	thickness of elliptical strut	[m]
c	chord length	[m]
$\tilde{c}_M(t)$	non-dimensional moment coefficient	

$\vec{e}_j$	radial unit vector	
$\vec{e}_p$	unit blade surface pressure vector	
f	frequency	[Hz]
g	axial distance between rotor and stator	[m]
i	index	
j	index	
k	reduced frequency / time lag	[Hz] / [s]
m	index	
n	index	
p	pressure	[mbar]
$\tilde{p}(s, t)$	unsteady pressure	[mbar]
r	non-dimensional cross-correlation	
s	complex variable / stator or rotor step	[] / [m]
s*	non-dimensional curvilinear location	
t	time	[s]
t*	time non-dimensionalized on a period	
x(t), y(t)	time signals	
x,y,z	cartesian coordinate system	

Greek

Φ	gust-vibration phase angle	[°]
Ξ	aerodynamic damping coefficient	
α	harmonic movement of the blade / absolute flow angle	[°]
β	relative flow angle	[°]
ε	relative error	[%]
γ	stagger angle / ratio of specific heat	[°] / []
θ	circumferential angle (in cylindrical coordinates)	[°]
φ	radial deflection angle	[°]
τ	period / time lag variable	[s]
ω	circular frequency	[radians/s]

Superscripts

i	blade surface location index

Subscripts

ax	axial
comb	combined
k	blade number index
ref	reference
sim	simultaneous
s	static value
t	stagnation value
1	upstream conditions
2	conditions downstream of wake generator
3	conditions upstream of measuring cascade
4	downstream conditions

CHAPTER 1 Introduction

This chapter introduces the topic of aeroelasticity and describes its role in turbomachinery applications. Special emphasis is placed on forced response vibrations and on aerodynamic excitations. A literature survey is included which summarizes experimental, analytical and numerical research conducted in this field to date. The chapter concludes with a statement of the objectives of this work, as well as a description of the technical approach employed to address these goals. The last section gives an overview of the framework of this dissertation: the Brite-Euram “Aeromechanical Design of Turbine Blades” project.

1.1 Aeroelasticity

“Aeroelasticity” is a term applied to the study of fluid-structure interactions. This field encompasses a wide range of engineering disciplines and applications, including flows around airplane wings, buildings, turbomachinery blades, heat exchanger vanes, etc. The first documented observations of aeroelastic phenomena date back to the early 1800's. Reports drafted by Scottish engineers during this time describe in detail the vibration of span bridges as the result of wind loading (see ref. [52]). Approximately one hundred years later, aeroelastic problems plagued the early development of the airplane. Försching [30] and Fung [33] attribute several occurrences of mechanical wing failure, including that of the Langley monoplane in 1903, to aeroelastic interactions. Perhaps the most notorious example of aeroelastic phenomena is the collapse of the Tacoma Narrows Bridge in 1940 in the State of Washington, USA. During the first four months it was open to traffic, the bridge exhibited wind-induced vibrations, earning the nickname “Galloping Gertie”. On November 7, in the presence of wind speeds near 70 kilometers per hour, the undulating motion of the bridge caused a midspan cable to break. Torsional vibrations ensued resulting in the rapid destruction of the bridge. This event, captured in an extensive series of photographs and film, was highly publicized around the world and served to highlight the need for an improved physical understanding of aeroelastic phenomena. Six years after the collapse of the Tacoma Narrows Bridge, Collar [19] published a paper describing the state-of-the-art aviation-related flutter and vibration research. In this landmark paper, he introduced a pneumonic device, later to be known as the Collar triangle, which describes the interdisciplinary nature of aeroelasticity. As shown in Figure 1, the vertices of the Collar triangle correspond to: (1) structural mechanics/elastic forces, (2) dynamics/inertial forces, and (3) fluid mechanics/aerodynamic forces.

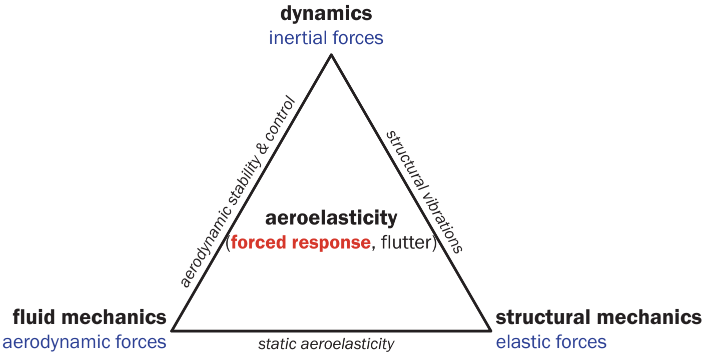

FIGURE 1. the Collar triangle of forces

The legs of the triangle represent sub-domains of aeroelasticity, as defined by the pairing of two forces. For example, the bottom leg, which connects the aerodynamic and elastic forces, corresponds to the study of static aeroelasticity problems, such as airfoil divergence. Today, the conventional Collar definition has been expanded to include forces derived from other sources as well, such as temperature induced stresses and control system inputs.

1.1.1 Aeroelasticity in Turbomachinery

In the turbomachinery domain, aeroelasticity typically refers to the study of dynamic fluid-structure interactions, and hence encompasses all three disciplines represented in Figure 1. In general, aeroelastic phenomena in turbomachinery can be divided into two groups: (1) self-excited vibrations or flutter, and (2) forced response vibrations, also referred to as resonant forced vibrations. In the case of flutter, a blade row enters into a self-excited vibration at a natural frequency of the mechanical system. The term “self-excited” indicates that flutter requires no imposed flow disturbance to sustain itself. Instead, the vibrating blade draws energy from the surrounding flow through a positive feedback relationship. For flutter, hence, the unsteady aerodynamic forces are generated solely by the blade motion.

Forced response vibrations arise when the blade row is subjected to a periodic flow disturbance whose frequency corresponds to a natural frequency of the system. In contrast to flutter, forced vibrations dissipate energy into the flow and therefore depend on the presence of the imposed perturbation to be sustainable. For forced response, therefore, the primary contribution to the unsteady aerodynamic forces is made by this external flow disturbance. A secondary contribution, however, is also derived from the blade motion. Besides the periodic wake/potential excitations, other sources of aerodynamic excitation comprise, for example, non-uniformities of the blades, vane distress or burner non-uniformities producing more complicated low engine order (LEO) excitations.

The importance of aeroelastic phenomena in turbomachinery applications is linked to the accompanying structural vibrations. The unsteady forces associated with forced response can result in high cycle fatigue (HCF) and eventually in structural failure of the blade. Such failures clearly risk significant damage to other turbomachinery components as well. It follows that this problem represents an important consideration in both the design and operation of turbomachinery. As an example, it is estimated that up to 40% of the problems encountered during the development of modern aircraft gas turbine engines are related to high cycle fatigue. A significant percentage of these HCF problems involve flow-induced blade vibrations. Furthermore, HCF problems account for approximately 5% of commercial sector maintenance costs. In the military sector, HCF related maintenance costs are estimated to total billions of dollars over the next 20 years [48]. More importantly, these types of blade failures in aircraft applications, though rare, pose an obvious risk to passenger safety.

The high cycle fatigue problems described above have fueled recent research efforts to improve aeroelastic analyses in turbomachinery. These efforts have been further motivated by the increasing prevalence of aeroelasticity-related problems, a trend which can be attributed to the ever more stringent demands for higher performance and lighter, more compact designs. These demands have pushed modern turbomachinery towards higher aerodynamic loading, lower blade stiffness, and closer blade row spacing, each which acts to increase the susceptibility of the blading to aeroelastic phenomena, and therefore to HCF issues.

An excellent overview of the state-of-the-art in aeroelastic research in turbomachinery in the late 1980's can be found in the *“AGARD Manual on Aeroelasticity in Turbomachinery in Axial Flow Turbomachines”*, edited by Platzer and Carta ([67], [68]). This collection of papers provides an extensive introduction to the subject, as well as detailed descriptions of many of the experimental, analytical, and numerical approaches used to investigate aeroelasticity in turbomachinery. Other good introductory references include Carta [17], Sisto [71], Verdon [77] and Bisplinghoff [5].

1.1.2 Forced Response Vibrations in Turbomachinery

The work presented in this thesis is concerned with forced response vibrations. As briefly described in the previous section, these vibrations result from the coincidence of an aerodynamic excitation in the machine with a natural vibration mode of the blade row. Unlike flutter, the risk of structural damage due to forced response is generally not immediate. Instead, the threat to the blading is typically from high cycle fatigue. Furthermore, although the occurrence of forced response phenomena is generally easier to predict than for flutter, it is significantly more difficult to avoid all such occurrences. Hence, the efforts of researchers in this field over the years have been necessarily focused on the challenging task of predicting the blade vibration amplitudes resulting from such interactions.

The first documented occurrence of resonant forced vibrations in turbomachinery was described by Campbell in 1924 ([13]). In this report, he details the existence of blade vibrations in a steam impulse turbine operating at partial speed. While this problem was correctly addressed as flow-induced forced resonance, only a limited emphasis was placed on the aeroelastic nature of the phenomenon. In fact, it was not until the time of the Second World War, with the introduction of the gas turbine engine, that a broader understanding of flow-induced vibrations in turbomachinery began to emerge. Regardless, the importance of Campbell's pioneering work is commemorated today by the Campbell diagram, an example of which is shown in Figure 2.

The Campbell diagram provides a convenient method to identify the coincidence of an aerodynamic excitation and a natural blade vibration mode. It plots rotor speed on the x-axis, versus frequency on the y-axis. The straight lines passing through the origin correspond to the various harmonics of the shaft frequency, commonly referred to as engine orders (EO), and represent possible aerodynamic excitation frequencies. The nearly horizontal lines represent natural blade vibration modes. The variations in natural frequency with rotor speed are due to the effects of centrifugal loading. Where the engine order lines and natural frequency lines cross, there exists the potential for resonant forced vibrations.

As implied from the above description, the aerodynamic excitations typically associated with forced response vibrations have frequencies corresponding to integral multiples of the rotor speed. This is because the majority of these interactions arise from the movement of the rotor blade through stationary flow non-uniformities. Sources of these disturbances include flow distortions created at the engine inlet or downstream of the combustor, as well as the presence of nearby non-rotating components, such as support struts and stator vanes. These particular sources enter in the category of low engine order (LEO) excitations.

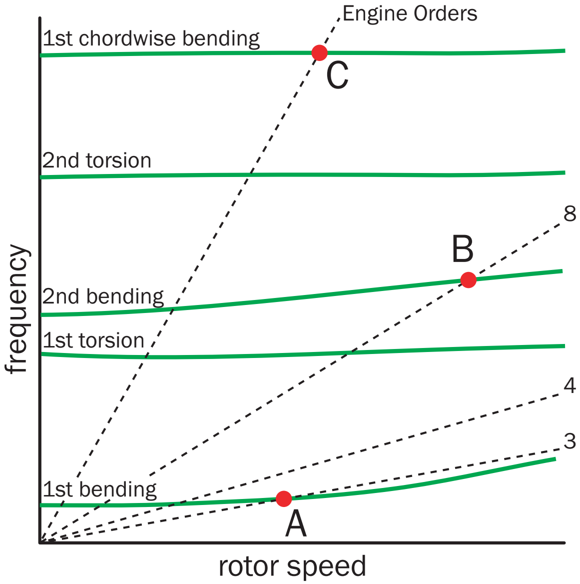

FIGURE 2. the Campbell diagram

In the Campbell diagram shown in Figure 2, the circles represent conditions under which high stresses were encountered due to resonant vibrations. Coincident points at low engine orders (e.g. A, B in Figure 2) typically involve engine inlet distortion, flow perturbations downstream of the combustor, or the effects of nearby air bleed slots or support struts. Coincident points at higher engine orders (e.g. C in Figure 2) typically indicate rotor-stator interactions.

The interaction between rotor and stator (point C in Figure 2) is a particularly common cause of forced vibrations, in large part due to the close proximity of these two components. Figure 3 illustrates the important characteristics of this type of interaction. Upstream of the rotor, the incoming disturbance consists of the stator vane wakes, as well as the stator potential flow field. Downstream of the rotor, the interaction with the opposing stator vane is purely potential in nature. As the rotor passes through the upstream and downstream spatial disturbances, a time-varying flow in the rotor passage results, giving rise to unsteady forces on the blades. The resulting blade vibrations will introduce additional unsteady effects that have a damping influence on the blade motion. It is the combination of these two flow fields that will ultimately define the aeroelastic behavior of the blade.

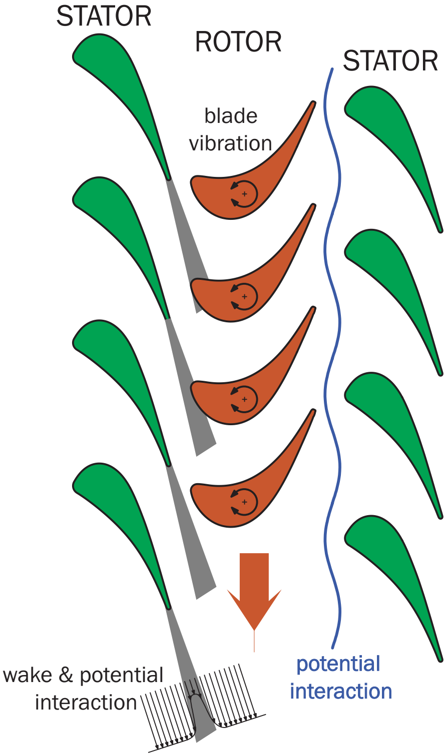

FIGURE 3. rotor-stator aerodynamic interactions

Two important parameters typically associated with the forced response problem are the reduced frequency, k, and the inter-blade phase angle, IBPA. The reduced frequency is defined as follows:

$$k = \frac{\pi \cdot c \cdot f}{U} \tag{2.1}$$

where f is the circular excitation frequency, and U is the upstream (compressor) or downstream (turbine) velocity. This parameter is a measure of the ratio between the inertial forces associated with the flow unsteadiness, i.e. the incoming flow perturbation or the blade motion, and those due to fluid convection. Jay and Fleeter [37] provide a range of reduced frequencies where forced vibration problems have been encountered in various compressor and turbine designs. These values are given in Table 1.

vibration modes	k
first bending	0.15 - 1.00
first torsion	0.40 - 2.00
second bending	0.50 - 3.00
second torsion	0.80 - 5.00
chordwise bending	1.00 - 10.0

TABLE 1. reduced frequency ranges for forced response

For resonant forced vibrations, there exists an inherent phasing between the unsteady forces applied to neighboring blades. This phase difference depends on both the number of circumferential flow distortions (e.g. the number of stator vanes or engine order, EO) and the number of rotor blades. In an ideal case, this phase lag will translate directly to the motion of the blades, where it is referred to as the inter-blade phase angle (IBPA). In a blade row, the blade surface unsteady forces are highly dependent on inter-blade coupling effects, and hence the IBPA. Not surprisingly, the aerodynamic damping resulting from the motion of the blades has also been shown to be strongly dependent on IBPA, introducing the notion of aerodynamic coupling.

While the Campbell diagram provides the basis to develop a turbomachine free from synchronous resonant vibrations, it is nearly impossible to conceive a design that circumvents all such coincident points. Hence, the designer must identify those conditions that pose the most serious risk of structural damage or HCF. This assessment requires an accurate knowledge of:

- the structural characteristics of the blading.
- the unsteady forces exerted on the blade by the imposed periodic flow disturbances.
- the aerodynamic damping applied by the flow to the vibrating blade.

For the structural characterization of a bladed disk assembly, the most difficult part is the determination of the structural damping and coupling. Up to now most developments supposed that the blade assembly was tuned. Recent simulations have demonstrated the importance of mistuning effects (frequency, damping, mode shape) that can lead to a scatter of blade vibrations amplitudes of up to a factor of ten. To date, detailed information about the last two items is rarely available during component design. Hence, the designer is often obliged to make his assessments based on various empirical design guidelines, and the impact of those coincident points which remain is determined during the development stages.

Motivated by the need to improve the accuracy of aeroelastic design methods, a significant research effort has been devoted over the years to both the analytical and experimental investigation of forced response vibrations. An overview of these efforts is presented in the following sections.

1.1.3 Analytical/Numerical Methods for Forced Response

The primary objective of the analytical/numerical work in this field is to develop accurate and efficient predictive methods. From a design perspective, the efficiency aspect is particularly critical. Hence, a substantial effort has been devoted to optimizing these methods by isolating the important physical aspects of the problem. Linearized methods, in particular, have received considerable attention. This approach and others are described in more detail below.

Early analytical methods applied to aeroelasticity in turbomachinery were based on classical linearized methods. In this approach, the blades are represented by flat plates at zero flow incidence. The unsteady flow is then considered to be a small perturbation about the uniform steady flow field, and hence the two can be completely decoupled. The flow perturbations themselves are expressed as combinations of potential and vortical disturbances. These methods are essentially limited to thin, straight airfoils with low steady loading. Nonetheless, they have been applied extensively in turbomachinery airfoil design. Excellent overviews of this technique and its variations are provided by Verdon [76] and Whitehead [80].

The above approach can be extended to account for the effects of realistic blade geometry and mean flows. This is accomplished by considering the unsteady disturbance as a small fluctuation relative to the fully non-uniform steady flow field. Examples of this approach applied to potential flow include Ni and Sisto [59], Whitehead [79], and Verdon and Caspar [75]. The coupling of the unsteady and steady flows, accounts for the effects of the steady flow gradients on the incoming perturbations.

Hall and Crawley [39] and Holmes and Chuang [44] describe similar linearizations applied to the 2-D Euler equations. Hall and Lorence [40] extended this technique to 3-D Euler flow. Finally, Holmes, Mitchell, and Lorence [45] introduced a linearized computational method based on the 3-D Navier-Stokes equations.

For these methods, the resulting set of unsteady equations is linear and coupled only to the steady solution. Hence, an important advantage of these techniques is that the unsteady effects arising from the blade motion and the various incoming flow disturbances (both of which are present in the forced response problem) are not coupled and can be treated separately. One of the goals of this dissertation is to investigate to what extent this unsteady decoupling is physically valid.

A further simplification to these equations can be made by assuming that the unsteady perturbation can be represented harmonically, and that each harmonic component can be calculated individually. This step essentially removes any explicit time dependence from the equations, and allows them to be solved by a wide range of solution methods. Finally, solutions for arbitrary flow disturbances can be obtained using Fourier superposition of the individual solutions.

The primary motivation behind these linearized approaches is the substantial reduction of calculation time relative to the solution of the full equations. Furthermore, these types of linearized codes have been shown to perform satisfactorily in many turbomachinery aeroelastic applications (e.g. Panovsky, Nowinski, and Bölcs, [65]).

By definition, however, the above linearized methods are limited to small unsteady perturbations, and hence can be applied only to incipient flutter and selected forced vibration cases. Therefore the role of direct solution methods remains important. Examples of aeroelastic methods based on a solution of the complete, non-linear Euler equations include Giles [34], He [41], and Ott [64]. Recent attempts to solve the full Navier-Stokes equations include He and Denton [42], Dorney and Verdon [22], Grüber and Carstens [36], and Ji and Liu [38].

Laumert and al. [54], [55] have conducted 3D viscous non-linear time-dependent simulations on a VKI Brite-Euram cascade geometry in order to investigate the aerodynamic blade excitation mechanisms in a phenomenological manner. They described separately the effects of wake, potential and shock distortions on the blade surface unsteady pressure distribution for three vibratory blade modes.

1.1.4 Experimental Methods for Forced Response

The primary objectives of the experimental work in this field are to enhance the physical understanding of forced response phenomena and to provide a basis for the development of numerical predictive techniques. While clearly the most appropriate setting for these experiments is in a real machine, this environment is not particularly accessible, nor conducive to instrumentation. In addition, it can be difficult to isolate specific phenomena. Hence, the majority of this experimental research is conducted in cascades or specially designed rotating rigs.

These studies generally fall into one of three categories of measurements: (1) aerodynamic gust response, (2) vibrating blade(s), or (3) combined gust response/vibrating blade(s). An overview of the research conducted to date in each of these three categories is provided in the following sections.

1.1.5 Aerodynamic Gust Response Measurements

These types of experiments are concerned with the time-varying, aerodynamic loading of a non-vibrating blade in response to a periodic upstream/downstream flow disturbance. The primary objectives of such experiments are to: (1) define the physical characteristics of aerodynamic gusts generated in turbomachinery, and (2) to quantify the blade loading resulting from these gusts in the absence of blade vibration effects. The majority of these experiments are conducted in annular cascades or rotating rigs, due mostly to the difficulties in producing proper gust loading in linear cascades.

One important exception to this rule is the early work of Ostdiek [63]. These experiments investigated the aerodynamic response of a five blade linear cascade to an oscillating inlet flow for low reduced frequencies. Fleeter [29], O'Brien, Cousins, and Sexton [61], and Dring et al. [23] used low-speed rotating rigs to conduct similar measurements.These experiments were focused primarily on the unsteady blade loading resulting from rotor-stator interaction.

Sturm and Fottner [73] conducted gust response measurements in a high speed linear cascade with cylindrical wake generators in a “hamster wheel” arrangement.

In general, much of the experimental work that followed was conducted in support of ongoing analytical/numerical efforts. Many of these experiments were particularly concerned with investigating the applicability of linearized methods to forced response phenomena. Capece and Fleeter [14], for instance, obtained measurements on a stationary vane in a three-stage axial compressor rig. The experimental results served to highlight the limitations of classical linearized methods by detailing the importance of the steady blade loading on the unsteady response of the vane.

In the 1990's, more attention was focused on the physical characteristics of the incoming aerodynamic gusts. Henderson and Fleeter [43] investigated wake-related gusts in a low-speed rotating rig. The flow disturbances created downstream of a rotating row of perforated plates and a row of airfoils were compared with the vortical gust models used in linearized methods. It was determined that the gusts created by the perforated plates satisfied the vortical gust model constraints. Furthermore, in this case, the agreement between the measured unsteady blade surface pressures and the linearized predictions was good. In contrast, the gusts generated by the rotating airfoils violated the model constraints, and the resulting blade surface comparisons were significantly worse. It was hypothesized that these discrepancies were due to potential flow content in the airfoil generated wakes.

Following this work, Manwaring and Wisler [57] developed a method based on Giles [35] to split the measured gusts into both vortical and potential components. This split was determined based solely on the measured unsteady velocity data. The results demonstrated the important presence of potential components in gusts created downstream of a rotating turbine blade row.

Feiereisen, Montgomery, and Fleeter [26] adapted the above method to incorporate the measured static pressure fluctuations as well. This allowed for a more strict decomposition of the vortical and potential components. They were able to verify the hypotheses of Henderson and Fleeter [43] by definitively identifying the presence of a significant potential component as the reason behind the cited discrepancies. This work also identified the important impact of upstream traveling potential disturbances on the unsteady response of the blade row.

Using the improved splitting method, Weaver and Fleeter [78] examined the effects of steady blade loading on the aerodynamic gust forcing functions created by turbine blade rows. Downstream of the blade row, the results showed an increase in potential effects with steady blade loading. In addition, some limitations of these splitting methods were identified, specifically as applied to the potential disturbances created upstream of the blade row.

Feiereisen and Fleeter [27] extended the two-dimensional gust splitting technique to three-dimensional flow for application to turbine blade wakes.

1.1.6 Oscillating Airfoil Experiments

This type of experiment is concerned with the unsteady aerodynamic loading generated on a blade vibrating in uniform flow. The primary objective of such investigations is to quantify the damping of the blade motion due to the flow, traditionally referred to as the aerodynamic damping. Experimental results of this type are particularly valuable for flutter investigations. More specifically, the sign of the aerodynamic damping term is an indication of stability and determines whether or not self-excited vibrations can occur.

Aerodynamic damping data is important for forced response vibrations as well. By definition, however, resonant forced vibrations are always aerodynamically damped. Therefore in contrast to flutter, the primary focus is not on aerodynamic stability, but rather the level of positive damping contributed by the unsteady aerodynamics. For forced response vibrations, this is an important consideration in the determination of the resulting blade vibration amplitude.

The first oscillating airfoil measurements were conducted approximately twenty-five years ago. Fleeter et al. [28] performed a series of measurements in a linear cascade where the blades were forced to oscillate in torsion at a given frequency and inter-blade phase angle. For various supersonic inlet conditions, the resulting unsteady blade loading was measured using embedded dynamic pressure transducers. These measurements were used to investigate the effects of inlet Mach number, reduced frequency, and inter-blade phase angle on the unsteady blade loading.

Adopting the same basic approach, Bölcs and Schläfli [7] conducted experiments in a non-rotating, annular turbine cascade. The advantage of the annular cascade for these types of measurements is its inherent circumferential periodicity, and hence the absence of spurious sidewall acoustic wave reflections. These investigations placed particular emphasis on quantifying the aerodynamic stability of the blade. The important influence of the inlet flow angle, the inter-blade phase angle, and the exit Mach number on the unsteady aerodynamic damping was documented. For certain flow conditions, self-started flutter was even observed.

Beginning with the work of Széchényi and Girault [74] and Davies and Whitehead [20], a number of studies have investigated the applicability of the “influence coefficient” technique or linear superposition principle to oscillating airfoil experiments. This principle states that the unsteady pressures which occur along a given blade surface can be represented by the linear sum of the contributions made by the individual vibrating blades in the cascade.

In a linear cascade, Buffum and Fleeter [10] investigated the validity of this technique in subsonic flow. They compared the unsteady measurements obtained while all blades were vibrating with the vector sum of measurements obtained with individual vibrating blades. In general, a good agreement was demonstrated. Some discrepancies were observed, however, that were later attributed to wave reflections from the lateral sidewalls of the test facility (Buffum and Fleeter, [11]).

Similar measurements were conducted by Bölcs, Fransson, and Schläfli [9] in three different annular cascades. Taking advantage of the inherent circumferential periodicity of the annular setup, these measurements were able to provide definitive evidence that the linear superposition technique is valid over a wide range of flow conditions.

Korbächer and Bölcs [51] investigated the limits of the superposition principle in the same test facility. Measurements were obtained for a compressor cascade operating at both subsonic and transonic flow conditions. It was determined that the unsteady pressures in close proximity to the shock cannot be linearly superimposed. This was attributed to the large, nonlinear perturbations introduced by the shock motion.

Finally, the reader is referred to a definitive collection of oscillating airfoil test cases referred to as the Standard Configurations. This data set was assembled by Bölcs and Fransson [8], Fransson and Verdon [31], and Fransson et al. [32] with the purpose of providing an experimental database for use in evaluating aeroelastic analyses. This well-documented collection of 11 data sets represents both an excellent introduction to these types of experiments, as well as an indispensable reference for continuing efforts in this field.

1.1.7 Combined Aerodynamic Gust/Oscillating Airfoil Experiments

This section describes experimental investigations involving combinations of gust and oscillating blade measurements. The superposition of these two flow fields addresses the complete forced vibration problem from an aerodynamic point of view.

Poensgen and Gallus [69] used an annular compressor cascade to investigate the unsteady pressures generated on a vibrating blade in the presence of steady and unsteady flow. A single blade in the non-rotating cascade was instrumented for unsteady pressure measurements. This same blade was mounted to an electrodynamic shaker system to allow for controlled oscillation in both the torsion and bending modes. Gust disturbances were generated upstream of the cascade using a rotating row of airfoils. Three series of measurements were performed: (1) oscillating blade only, (2) upstream gust only, and (3) combined oscillating blade and gust. A primary focus of this study was to determine whether the combined case represents a linear superposition of the gust and oscillating blade effects. A single set of results corresponding to an inlet Mach number of 0.24 was presented. In general, good agreement between the measured unsteady pressure data for the combined case and the superimposed gust/oscillating blade results was observed. However, some significant discrepancies, particularly with respect to the unsteady pressure phase angle, were present near the blade trailing edge. These discrepancies, though not explained, were more than likely due to experimental error in a region of relatively small unsteady pressure magnitudes.

Kim-Frey [49] and Kim-Frey and Fleeter [50] used a three-stage axial flow compressor to investigate the unsteady aerodynamics on a rotor blade row subjected to simultaneous forced excitation and imposed gust disturbances. The aerodynamic gust is created upstream of the rotor blade row using two stationary perforated plates. The rotor disc itself is equipped with special hardware to allow for the controlled torsional oscillation of four blades simultaneously. The results for arbitrary inter-blade phase angles are then obtained using the influence coefficient technique. A total of four blades were instrumented to measure the unsteady blade surface pressure distribution. As for the previously described experiment, measurements were obtained for: (1) only the gust, (2) only the oscillating blade, and (3) a combined oscillating blade and gust. One of the primary focuses of this study was to determine whether the gust and oscillating blade effects are linearly superimposed in the combined case. It was concluded that this linear assumption was valid for small oscillation amplitudes and low steady blade loading. Possible limitations of the influence coefficient technique or error on phase measurement were considered as possible source of observed discrepancies.

Manwaring, et al. [58] performed measurements on an extensively instrumented two-stage fan. The objective of these experiments was to investigate the complete forced response problem, including both gust and blade motion effects, in a realistic turbomachinery environment. Two blades in the first rotor were instrumented to measure unsteady blade surface pressures. A total of four blades, including the two instrumented blades, were also equipped with root strain gauges to measure vibratory stresses. An inlet total pressure flow distortion could be generated using screens mounted upstream of the rotor blade row. It was observed that the gust perturbations created by the screens were primarily vortical in nature, with also a significant entropic content. Good agreement with two-dimensional, linearized numerical codes was demonstrated for measurements made away from blade structural resonance. Near resonance, the agreement between the predicted and measured unsteady loading became progressively worse. These discrepancies were attributed to the possible existence of three-dimensional effects in the unsteady flow field.

Nowinski [60] has recently conducted extensive measurements on a single pitching compressor blade in the presence of downstream generated potential disturbance in a linear wind tunnel. He concluded that the superposition principle holds for a wide range of reduced frequencies, incidence angles, gust-vibration angles and even in the presence of flow separation. However, he found that, in the local presence of shocks, the linear superposition principle wasn’t valid.

1.1.8 Structural Issues for Forced Response

While this work is essentially limited to the aerodynamics side of the forced response problem, it should be made clear that structural characteristics of the blade row play an equally important role in determining its aeroelastic behavior. Our ability to determine the natural modes of vibration of a given blade row has greatly improved over the years. In large part, this is the result of significant advances made in finite element methods.

The earliest studies of flow induced blade vibrations drew heavily on basic beam theory. Using this approach, the blade motion was classified in terms of pure bending, torsion, or edgewise modes (Armstrong and Stevenson, [4]). These types of analyses, however, ignore the effects of radial geometric variations of the blade profile, as well as mechanical coupling via the disk or tip shroud. In particular, mechanical coupling introduces system vibration modes that can involve combined bending/torsional motion. Hence, today, structural engineers commonly rely on finite element analyses to characterize the natural vibration modes of a given blade row (Ewins and Henry, [24]: Ewins, [25]). Recent research in this field include the modeling of mistuning and coupling effects that cannot be avoided in the production process and significantly affects the vibratory response of a bladed disk assembly. An excellent thesis on this subject, with a good summary of the current research in structural simulations of bladed disk assembly, has just been issued by Kahl [46].

An interesting paper predicting the vibratory response of a turbine blade due to upstream vane distress (LEO) has been presented by Panovsky and Carson [66]. In this article, the authors summarize the overall approach from steady CFD simulations to crack propagation analysis in a quantitative approach to determine blade life. The results show that vane distress is a significant excitation source for the blades and are in good agreement with experiments.

There still exist several challenges to overcome before these analyses can be considered optimized for turbomachinery applications. In general, however, it can be said that there currently exists a higher level confidence concerning these structural determinations, as compared to the aerodynamic issues. In general, the gap between aerodynamic and structural research in turbomachines is diminishing. In the near future, specialists in aeroelasticity will have to master both topics as coupled aerodynamic and structural codes will appear.

1.2 Summary of State-of-the-Art

A summary of the current state-of-the-art in unsteady aerodynamics research applied to the forced response problem is given below, with a special emphasis on those elements that warrant additional investigation:

1. while a fair amount of oscillating airfoil and aerodynamic gust response data exists in the literature, there are have been comparatively few experimental investigations focused on the complete forced response problem, i.e. the simultaneous consideration of both gusts and vibrating blade effects.
2. moreover, there exists little experimental evidence available to confirm the traditional linearity assumption, specifically that the above two effects can be treated separately and subsequently superimposed.
3. furthermore, the simultaneous investigations have never been conducted on a full vibrating cascade but on a limited number of vibrating blades in combination with the influence coefficient technique possibly at the origin of observed discrepancies in the linear superposition principle.
4. relatively limited attention has been directed towards the local validity of the superposition principle as compared to its validity on the overall loading of the blades.

1.3 Objectives and Technical Approach

The overall objective of this research is to achieve a broader physical understanding of the complete aerodynamic forced response problem. The word “complete” here refers to a simultaneous consideration of the unsteady aerodynamic contributions derived from both upstream generated aerodynamic gusts, as well as the cascade’s vibration modes. As mentioned previously, these two effects have traditionally been treated separately. However, any estimation of the blade vibration amplitudes associated with forced response phenomena must consider both of these effects. Hence, it is of particular interest in this work to investigate the exact nature of the interaction between these two sources of unsteady flow fields.

The following specific tasks are outlined in order to address the above objectives:

- measure the unsteady aerodynamic blade response to (1) imposed cascade vibration modes (travelling wave mode), (2) upstream generated aerodynamic gusts, and (3) combinations of these two effects.
- using the above experimental results, address the local validity of the assumptions inherent in linearized treatments of the forced response problem. Specifically, can the local unsteady blade loading be considered as a linear superposition of the unsteady forces derived individually from the cascade’s vibration mode and from the aerodynamic gusts?

The experimental tasks detailed above have been performed in a non-rotating annular test facility using a test rig composed of rotating wake generators and a fixed turbine cascade. There are two rotating wake generators: one possesses 13 elliptical struts and the other has 22. Each one is designed to generate wake profiles similar to a blade row. The turbine cascade consists of 20 blades attached to a separate torsion suspension system, with a magnetic excitation feature, allowing the control of the cascade’s vibration mode. Several blades are instrumented to measure the resulting surface steady pressures, unsteady pressures and blade vibration mode.

1.4 The Brite-Euram ADTurB project

"Aeromechanical Design of Turbine Blades" (ADTurB BRPR-CT95-0124), is a European project to generate experimental data for validation of design and analysis tools that are used to predict amplitude of vibration in bladed disk assemblies.

The consortium consists of 12 partners (Rolls-Royce plc, Snecma Moteurs, Rolls-Royce Deutschland, Turbomeca, ITP, FiatAvio, DLR, KTH, ONERA, EPFL, University of Limerick, University of Oxford), from six countries within the European Community and one associated country. This includes six industrial partners all with a common interest in the ultimate objective, i.e. eliminating HCF failures in gas turbine rotors, all coming together to support experiments at world leading research centers and universities. The industrial partners perform a range of tasks from design and manufacture of rig hardware to supporting testing and analysis. Two of the research organizations, DLR and EPFL control unique facilities which were adapted to meet the needs of the experiments. Other academic partners are engaged in predictions using innovative techniques to prove their effectiveness. The partnership includes amongst them recognized world experts in the field of aeroelasticity and vibration.

Aero-engine manufacturers need to eliminate high cycle fatigue failures to improve aircraft safety, engine reliability and cost of ownership. Additionally there is a strong need to be able to predict vibration levels to reduce lead times and to expand the freedom of the turbine blade designer to explore more optimal designs. The objectives of this project were to provide good quality data with which to validate current and future prediction software, and to compare a variety of approaches to give an "exchange rate" between cost and accuracy.

To achieve these objectives, two experimental campaigns were devised. The first rig at EPFL was used to verify the superposition principle for forced response, since many prediction methods already assume that the aerodynamic forcing-function and the aerodynamic damping can be calculated independently. The second rig at DLR provided aerodynamic and vibration response validation data for a realistic turbine stage. The measurement programme was designed to allow validation at all stages through-out the prediction process so that errors can be accurately pinpointed.

To investigate blade forced response effects in a high pressure turbine stage two experiments have been performed in the DLR rig. A major coordinated effort amongst the partners was required to design, manufacture, instrument and assemble the rig in the wind tunnel of rotating cascades RGG at the German Aerospace Centre DLR in Göttingen. The first experiment uses an existing "rigid" rotor and deals with the identification of the aerodynamic forcing functions. The second experiment used a new designed rotor with "flexible" blades, using the same airfoil, which has targeted resonant frequencies within the rig running range. Both experiments provide a database for the validation of forced response prediction codes for high pressure turbines. In order to be able to change the blade passing/disturbance frequency on the rotor over a wide range two stators with different number of blades are used for the investigations. A first stator with 43 blades and a second with 70 blades was designed and manufactured.

The first project has fulfilled its objectives. A database of the results was established and populated during the project, enabling an accessible record of all the results and also easy comparison of data from any source. The results show that many aspects of the prediction process are well modelled, but the prediction of unsteady aerodynamics remains the largest contributor to error. Additionally the DLR rig showed a significant low engine order response and this will provide a useful “head start” for the follow on project: ADTurB II, involving additional industrial and academic partners (MTU, ALSTOM, University of Naples, Imperial College, ECL).

The follow-on project, ADTurB II, builds on the past experience extending the technology to other excitation sources and more complex phenomena as outlined below. The subjects under investigation are:

- Low Engine Order (LEO) Excitation.

This accounts for half of the vibration problems experienced in turbomachinery blading and is caused by non-uniformities in flow around the annulus due to differences in nominally identical vanes, burners etc.

Previous research in the field of forced response prediction has focused almost exclusively on wake passing frequency excitation where boundary conditions can be well defined and the problem size is smaller. Single blade and vane sectors can then be used for numerical simulations. The more variable and potentially dangerous LEO sources have been largely ignored because the problem is more difficult.

- Influence of Mistuning / Damping on Vibration Amplitude.

Blade to blade variations in frequency, mode shape, damping and aerodynamics cause a large amplitude scatter (up to 10:1). It is crucial to be able to predict not just typical but maximum amplitudes as it would normally be the maximum amplitude blade that fails.

Both of these subjects have a common underlying theme, i.e. examining the effects of non-uniformity. It is intended to explore these subjects by undertaking a series of experiments on the same continuous flow rig as for ADTurB but with a new more flexible rotor, investigating vane flow variation. In addition, mechanical and aerodynamic mistuning experiments will be performed in the non-rotating annular test facility at EPFL.

CHAPTER 2

Experimental Apparatus

All measurements presented in this dissertation have been conducted in the non-rotating annular test facility of the “Laboratoire de Thermique Appliquée et de Turbomachines” (LTT), “Ecole Polytechnique Fédérale de Lausanne” (EPFL). This chapter describes all the experimental apparatus and measurement devices used for the Brite-Euram ADTurB I project (see 1.4) and the subsequent results presented in chapter 4 and chapter 5. Specific details are provided concerning the numerous modifications on the test facility and the new equipment used as part of this experimental research project.

This chapter continues in section 2.8 p. 45 by giving an overview of the integration of all the control systems previously described. It concludes with a summary of all the key modifications made on the non-rotating annular test facility.

The reader is referred to chapter 3 for the description of the measuring techniques used in combination with the devices presented in this chapter.

2.1 Air Supply Network

The non-Rotating Annular Test Facility is part of a network of experimental facilities at the LTT that share a common air supply. A schematic of this system is given in Figure 4. Air is supplied to the network on a continuous basis by a four-stage centrifugal compressor. This compressor has a maximum pressure ratio of 3.5 and a maximum flow rate of 12 [kg/s]. The compressor is driven at a constant speed of 9500 RPM by an electric motor. At peak level operation, the motor consumes approximately 2.2 [MW].

As shown in Figure 4, air is initially drawn from the atmosphere and passes through an inlet valve into the compressor. At the exit of the compressor, air temperatures can reach as high as 180 [°C]. A pair of heat exchangers is available to regulate the temperature of the air entering the various test stands. Typical test section temperatures range between 20 [°C] and 60 [°C]. Within the test facility network, the system-wide flow conditions are regulated using the compressor inlet valve in combination with an air bypass valve. The bypass valve also acts as an emergency release in the case of an impending surge. Independent control of the flow conditions for a given test facility is achieved using separate inlet and outlet valves.

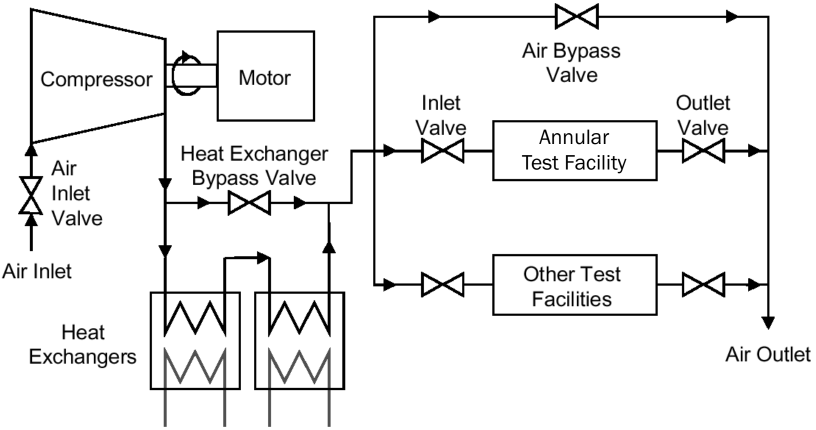

FIGURE 4. air supply network

2.2 The Non-Rotating Annular Test Facility

Flow measurements in turbomachinery blading can be performed in the following ways:

- studies in the turbomachine itself.
- experiments in annular cascades.
- experiments in linear cascades.

Unfortunately, the testing of turbomachines often presents numerous drawbacks such as cost disadvantages and realization difficulties. It is particularly difficult to use heavy measuring instrumentation on a rotating turbine or compressor row. With this in consideration an original concept was developed at the LTT: a non-rotating annular cascade, see Bölcs [6].

FIGURE 5. the non-rotating annular test facility

This device includes a nozzle allowing the realization of an axisymmetric steady flow with a swirl corresponding to the relative flow in an axial turbomachine. A radial-axial nozzle generates the flow condition in the test section of the annular wind tunnel. The pre-swirl vanes are situated in the radial entry of the test facility where the flow is subsonic (see Figure 6). Through this method, the shock interference effects between the pre-swirl vanes and the test cascade are eliminated. In addition, the clearance between the tip of the blades and the casing remains constant for all pre-swirl vane positions. Downstream of the guide vanes, the flow is accelerated and turned in the axial direction. The tangential velocity component in the nozzle increases with decreasing radius (according to the momentum theorem), and the normal velocity component increases according to the law of continuity. The velocity and flow angle in the test section depend on the nozzle geometry as well as on the inlet flow conditions. With an appropriate choice of flow conditions, subsonic or supersonic flow may be achieved in the test section. In the case of supersonic flow, the flow area normal to the velocity vector evolves along the trajectories as in a Laval nozzle. Thus, the flow area decreases in the subsonic part of the nozzle until sonic velocity is obtained; thereafter it increases. The sonic throat in the annular nozzle is self-generated, and appears at different locations depending on the inlet conditions. The flow in the test section is axisymmetric but variable over the channel height. According to the rotation of the flow, the static pressure is higher on the outer wall than on the inner wall. With constant spanwise total pressure, the Mach number will therefore decrease while the flow angle increases from the inner to the outer surface. However, this spanwise Mach number distribution is also influenced by the generation of a total pressure gradient over the nozzle height.

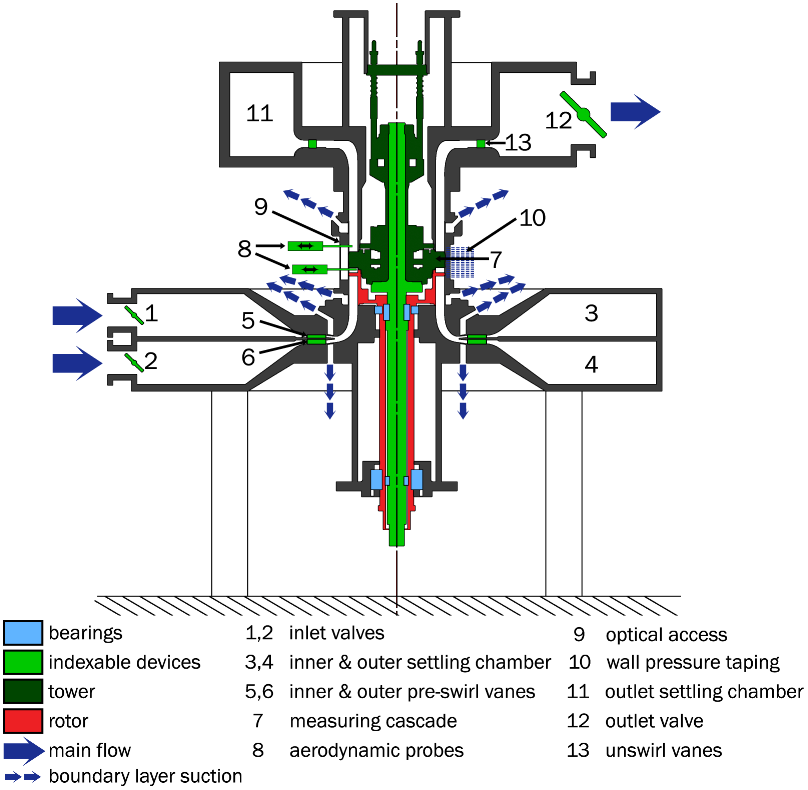

FIGURE 6. schematic view of the non-rotating annular test facility

As a result, two separate inlet flows with different velocities and angles are generated in the annular cascade facility (“1” and “2” in Figure 6). The velocity profile in the test section results as these two flows merge. The generation of the two separate flows is done in independent settling chambers (“3” and “4” in Figure 6). In each of these inlet flows, the pre-swirl vanes (“5”, “6” in Figure 6) can be regulated independently of each other. The velocity profile in the inlet sections can be influenced by two separate boundary layer suction locations immediately downstream of the pre-swirl vanes. Four additional independent suctions upstream and downstream of the test cascade may also be used to further influence the velocity profile as well as the boundary layer. Whereas in a linear cascade the suction is used to adjust periodic flow conditions, in an annular cascade the suction is used only to influence the velocity profile over the channel height and to reduce the secondary flow effects. Flow measurements are conducted upstream and downstream of the cascade with five-holes L-probes (“8” in Figure 6). Since they can only move radially the tower can be rotated step-by-step in order to get a complete mapping of the flow conditions upstream and downstream of the cascade. The Non-Rotating Annular test facility allows the study of transonic flow phenomena in compressors and turbines. The experiments are applied to explain physical phenomena appearing in a transonic stage as well as to simulate test cases for design and off-design calculation methods.

2.3 The Rotating Wake Generator

Considering the principle of the non-rotating annular test facility described in the previous section, the study of rotor-stator interactions in this test stand implies the use of a rotating wake generator in order to simulate impinging wakes on the measuring cascade. In other words, in this particular facility the rotor of a real axial turbomachine is represented as a stator (measuring cascade) whereas the corresponding stator is represented as a rotor (rotating wake generator). This last device was specially designed for the Brite-Euram ADTurB projects (see section 1.4). The rotor integration in the non-rotating annular test facility was indeed one of the greatest technical challenges of the project, especially considering the indexing feature of the measuring cascade. This resulted in the fabrication of a co-axial drive system as schematically represented in Figure 6. A 45 [kW] synchronous motor equipped with a “MOSFET” control system drives the wake generator and controls precisely its speed. A synchronization between the movement of a reference blade and the rotor’s rotation speed is possible and described in section 2.8.

The design of the wake generator aimed for the same relative flow conditions as the one obtained at midspan, and at design conditions, on the DLR Göttingen ADTurB test rig (see section 1.4). In order to match the wake profile impinging on the blade rows of the two test facilities, 3D unsteady multistage simulations using J. Denton’s UNSTREST 13 were carried out on both test setups (see [56]). Besides the relative flow conditions at midspan the wake profiles were matched for maximum total pressure drop and wake width upstream and downstream of the blade row. Several cylindrical struts and flat plates were tested at different axial positions. The design process led finally to the use of elliptical struts avoiding the disadvantages of both cylindrical bars and flat plates; i.e. Von Karman Vortex generation and high sensitivity of the wake profile to inflow angle, respectively. Figure 7 shows a schematic view of the wake generator and the blade row. Table 5 gives the corresponding main geometric values for the two wake generators (engine orders 13 and 22). Variation of the axial gap and the strut stagger angle for the two setups are due to the alignment of the major axis of the elliptical struts to the relative inflow, this latter being different for the two wake generators in order to keep a constant wake generation frequency[1].

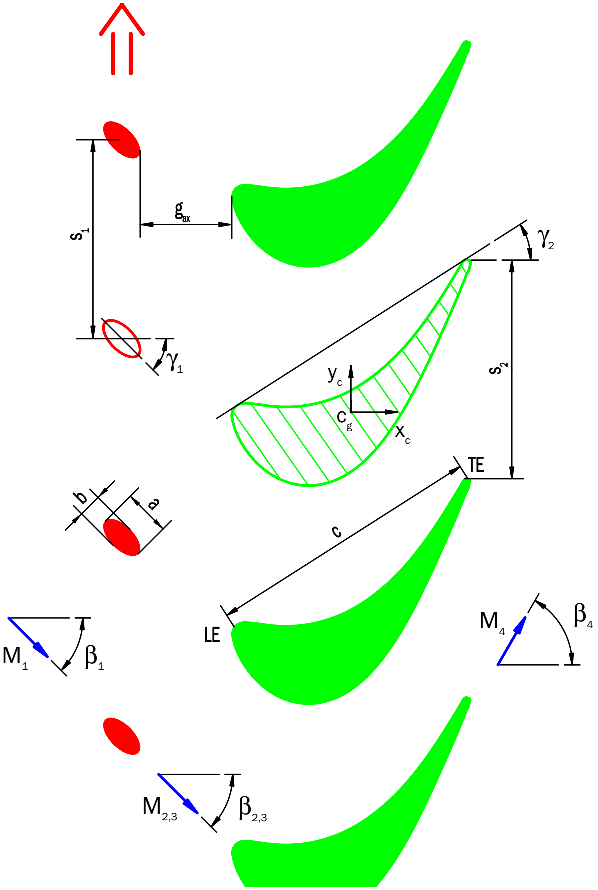

FIGURE 7. schematic view of wake generator and blade row

---

[1] *The superposition of gust response and controlled vibration has to be at the same frequency given by the design of the blade suspension system (eigen-frequency) for periodicity reasons.*

	EO 13	EO 22	units
γ_1	39	41.3	[°]
γ_2	-32.7	-32.7	[°]
a	12	12	[mm]
b	6	6	[mm]
c	75.2	75.2	[mm]
g_{ax}	24.06	23.94	[mm]
s_1	87	51.41	[mm]
s_2	56.55	56.55	[mm]

TABLE 5. wake generator and blade row main geometric values

2.4 The Measuring Cascade

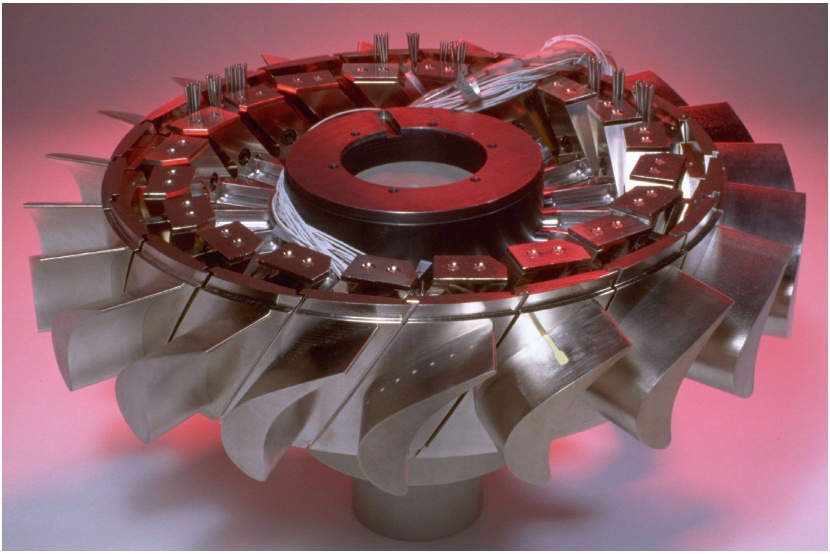

FIGURE 8. B-E ADTurB measuring cascade

The measuring cascade, illustrated in Figure 8, comprises twenty prismatic turbine blades. The blade profile corresponds to the one (at midspan) in the more realistic forced response test facility (DLR Göttingen) as part of the Brite-Euram ADTurB project (see section 1.4). Each blade has its independent suspension system for controlled vibration, as shown in Figure 9. The design of this system aimed a first torsion mode around 275 [Hz][1]. At this frequency the magnetic excitation system is still able to vibrate the blade vibration system at high enough amplitudes for precise unsteady pressure measurements on the blade surfaces.

F-E modeling was used to evaluate the different spring designs before the fabrication of spring prototypes. Most of the design was done using a 3D design program (IDEAS MS 3.0) allowing the computation of different structural parameters like the weight of each part, center of gravity and inertial properties. These features were very useful for the selection of the materials and were used to place the center of gravity of the torsion setup on the torsional axis of this system. The design of the metallic spring for a pure torsion movement is shown in Figure 9 and consists of a cross-shaped cross-section about 30 millimeters long.

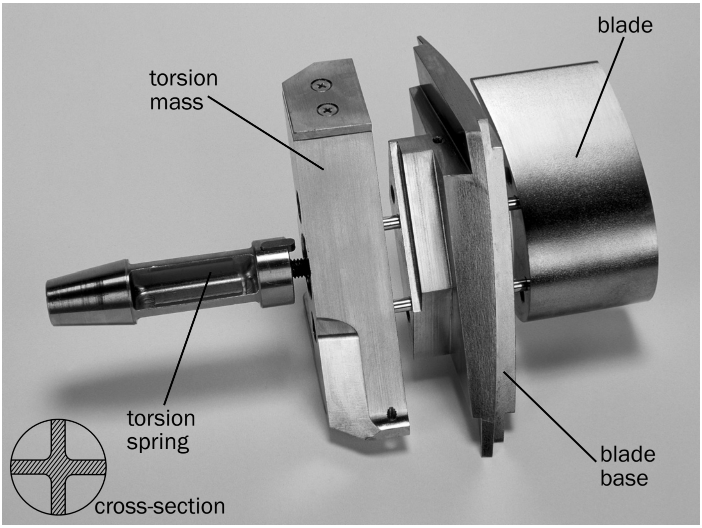

FIGURE 9. Blade suspension system for torsion (blown-up model)

One blade is equipped with three embedded accelerometers (ENTRAN EGA-125-100D) in order to monitor the blade's two-dimensional movement and validate the pure torsion mode assumption. The other instrumentation of the blades consists of blade surface pressure measuring devices for both steady and unsteady pressures. Six blades are equipped with pres-

---

[1] *A second set of metallic springs and masses were designed for a pure bending mode at the same eigenfrequency. Unfortunately the cascade's vibration mode wasn't stable in presence of passing gusts due to the limitations of the cascade vibration control system (see section 2.5).*

sure tappings at three different blade height (25%, 50% and 90%) as pairs of PS and SS measuring blades, in order to minimize the effect of mistuning of these instrumented blades. Similarly, two blades (PS and SS) are equipped with unsteady pressure transducers at midspan. There are twelve measuring locations on the SS measuring blades and nine measuring locations on the neighboring PS measuring blades (channel measurement) with the LE measurement being conducted on both blades. This feature is quite useful to verify the symmetry of the incoming flow (angle of attack) and to verify the superposition of the unsteady pressures over one profile for integral values calculation (unsteady lift/moment coefficients). The distribution of the pressure measurement locations on the blade profile is given in Figure 10 for both steady and unsteady measuring blades. The three different blade height steady pressure measurements allow the validation of the quasi-two-dimensional flow assumption as well as the computation of the steady loading. The unsteady pressure measuring blades enable the measurement of the pressure fluctuations due to the different unsteady sources presented in this work.

The pressure taps are constructed from 1.5 [mm] diameter cavities that run the length of the blade. Within each cavity, a piece of medical-type steel tubing is placed. The cavity is then sealed with a durable epoxy. The actual measurement location along the blade surface is connected to the imbedded metal tubing by a small 0.4 [mm] tap drilled normal to the blade's surface. The metal tubing exits at the blade base and is connected to the steady pressure measurement system with flexible Viton tubing ®.

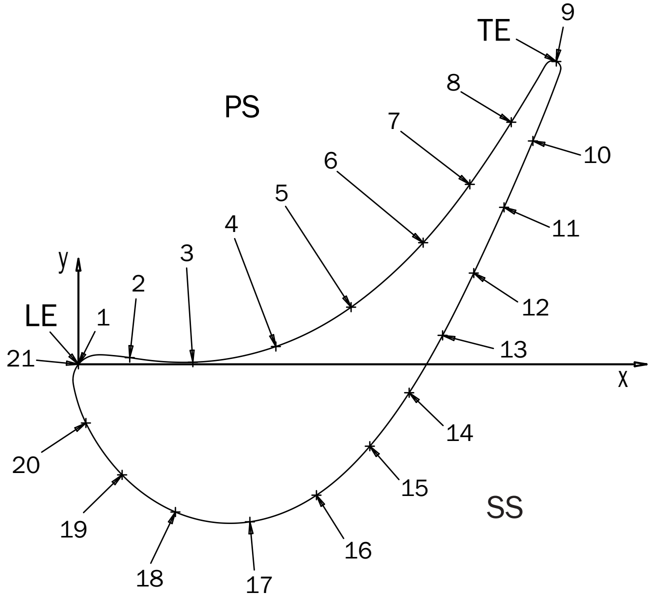

FIGURE 10. blade surface pressure measurement locations

The high-response piezo-resistive pressure transducers used are cylindrical ENDEVCO™ Model 8534A with a 50 [psia] range. They are mounted in a similar manner as the steady-state pressure tap: the pressure taps are constructed from 1.7 [mm] diameter cavities that run the length of the blade. The actual measurement location along the blade surface is connected to this hole by a small 0.4 [mm] tap drilled normal to the blade's surface. The pressure transducer is placed inside the access hole and then glued with epoxy through a second hole (see Figure 11). Compared to surface mounted unsteady pressure transducers, the main advantage of this mounting technique is a high physical protection of the membrane to dust particles or rough handling. Furthermore, the membrane's low sensitivity to acceleration effects in this configuration (no movement perpendicular to the membrane) make tedious acceleration corrections obsolete.

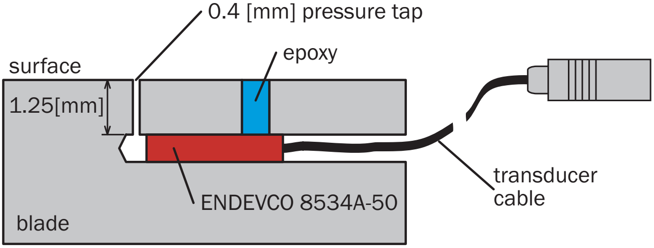

FIGURE 11. schematic view of unsteady pressure transducers mounting

2.5 The Cascade Vibration Control System

The cascade vibration control system (BBC EME 100) consists of an oscillator, a phase controller, twenty individual blade control systems and is schematically represented in Figure 12. The oscillator generates a reference signal with the desired frequency and feeds it into the phase controller. This second device splits the main reference signal into twenty blade reference signals with controllable phases. Each blade vibration system then uses its assigned reference signal as set point. The blade suspension system described in the previous section (see Figure 9) is put into motion by the means of an electromagnetic excitation system, schematically represented in Figure 13. Each blade vibration control system uses an inductive displacement transducer (VIBRAX made by Vibro-Meter) to monitor the blade's motion and use it as feedback in the control loop. The vibration amplitude of each blade can be selected directly on the individual blade vibration control system. Typical vibration frequencies produced by this system are between 150 and 300 [Hz]. The amplitudes range between 0.3 and 0.5 [°] for a torsional movement, allowing accurate unsteady pressure measurements on the blade surfaces. With this blade vibration system design, higher vibration frequencies would diminish rapidly blade movement amplitudes, reducing in the same manner the signal-to-noise ratio of the unsteady pressure signals.

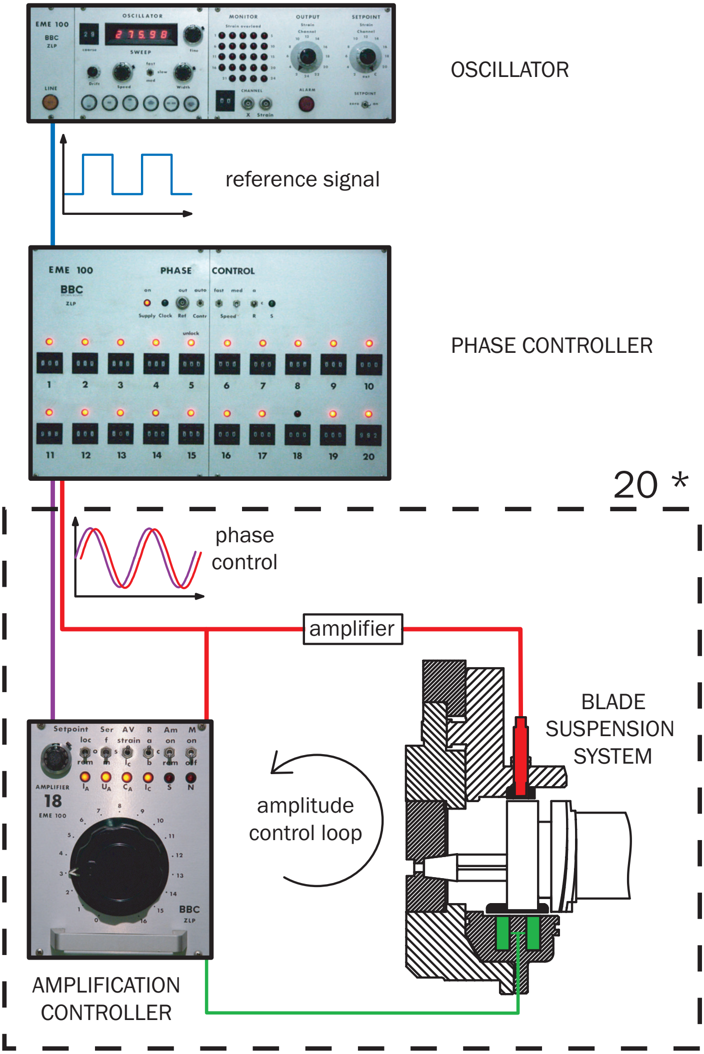

FIGURE 12. cascade vibration control system

The blade vibration control system can only excite the blade suspension system and not damp its movement. Measurements are therefore only possible as long as the disturbing forces of the flow are not bigger than the force induced by the magnetic system.

LEGEND:

1	cascade's core
2	metalic spring
3	mass element
4	blade base
5	blade
6	displacement captor
7	transformer plate
8	electromagnet
9	hydraulic break
10	teflon ring
11	DS inner wall
12	US inner wall
13	outer wall

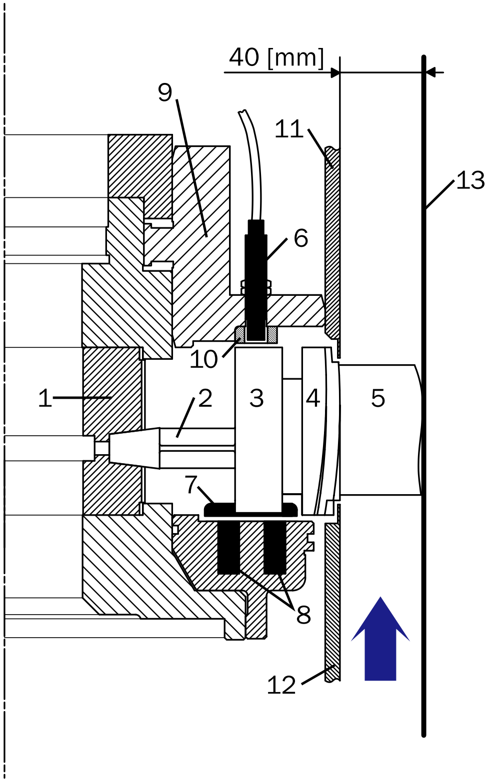

FIGURE 13. controlled vibration setup

2.6 The Tower Assembly

FIGURE 14. B-E ADTurB tower

The tower assembly mainly consist of the measuring cascade, its excitation system, a hydraulic brake, and a connector plate. Its design allows rapid changes of rotor configuration or tower swap and a full rotation of the measuring cascade in the test facility (see section 2.2). The hydraulic brake (“9” in Figure 13) has three main functions:

- to block the blades by applying the brake on the masses for steady-state or gust response measurements.
- to hold the displacement transducers (“6” in Figure 13) and allow the optimization of their signals by regulating the distance to the ferromagnetic plates on top of the masses.
- to avoid damage of the vibrating systems by limiting physically the vibration amplitudes[1].

---

[1] *Since the blade vibration system has no damping feature, some situations can lead to amplifying blade amplitudes with possible damages on the blade suspension system.*

2.7 Aerodynamic Probes

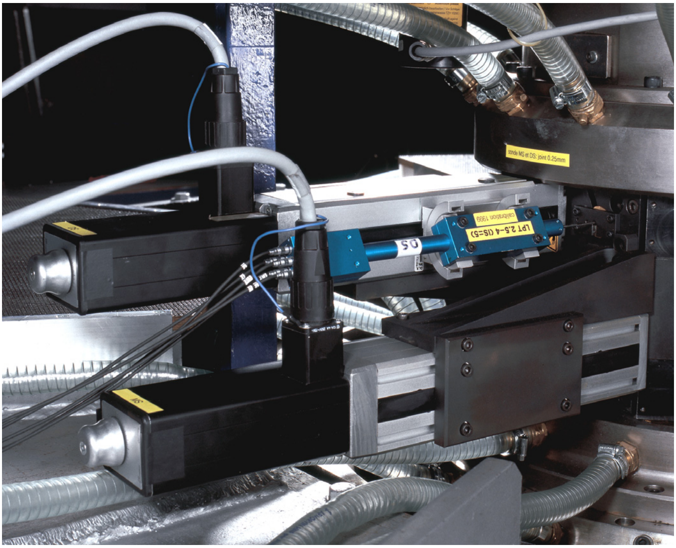

FIGURE 15. US and MS probe holders

New probe holders have been designed to measure the steady flow conditions at the following locations: upstream of the rotating struts, between the rotating struts and the measuring cascade, and downstream of the blade row. Three precise industrial linear displacement systems were selected to control the radial positioning of each probe, two of them are shown in Figure 15. A variable pitch angle mechanism has been designed to set the stagger angle of each probe along the mean flow direction at the corresponding flow measuring location. The combination of the radial positioning of the probes and the rotation indexing of the measuring cascade allows precise flow mapping at the three axial positions. The probes used are five-holed L-shaped probes (2.5 [mm] diameter) upstream and downstream of the simulated turbine stage and, due to reduced spacing between the strutted disk and the blade row, a four-holed wedge probe (3 [mm] diameter) at that location. All the probes have been fabricated in stainless steel tubings.

An unsteady wedge probe developed at Oxford University [3] has been employed to measure the wake produced by the rotating struts. It is composed of three surface mounted unsteady pressure transducers covered with elastomer allowing two-dimensional unsteady flow measurements. The reader is referred to [1] and [2] for a detailed description of unsteady wedge probe measurements using piezo-resistive pressure sensors.

The different types of aerodynamic probes employed in this study are presented in Figure 16.

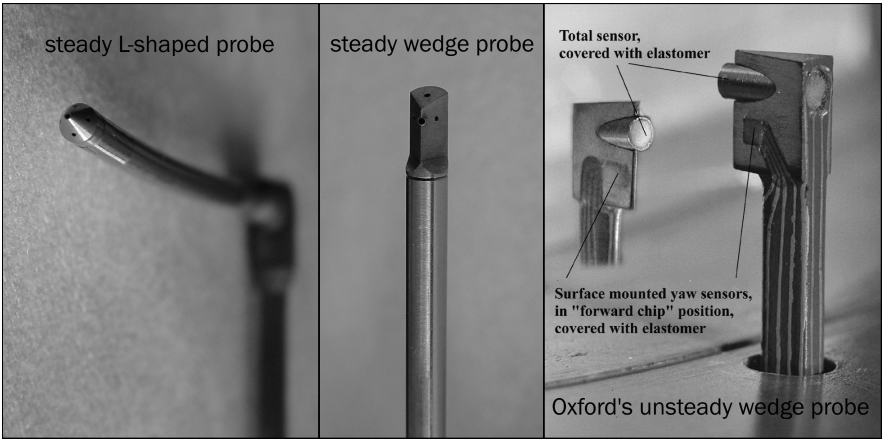

FIGURE 16. steady and unsteady aerodynamic probes

2.8 Control Systems and Data Acquisition Hardware

Besides the air supply, the flow controls and the cascade vibration control system, all the new equipment has been conceived with the idea of controlling and automating the measurements from two different PCs running National Instrument’s Labview™ 6.0i programming language. Most devices have independent control systems and only the minimum commands are given from the control programs. This feature saves CPU usage for data acquisition and data reduction and maximizes the control speed through dedicated low-level electronic control systems. As schematically represented in Figure 17, one PC controls the test facility (tower indexing, probe positioning, rotor speed control) and the steady data acquisition, enabling the control and measurement of the steady-state flow. The other PC handles all the unsteady data acquisition and data reduction so that results can be checked just after the unsteady measurements have been carried out.

Figure 17 shows the data acquisition setup used when the rotor is running and the steady PC controls its speed, which corresponds to gust response, forced response or unsteady wake measurements. For the other types of measurements carried out in this study, the reader is referred to section 3.4 and 3.6 for a detailed description of the measuring methods used.

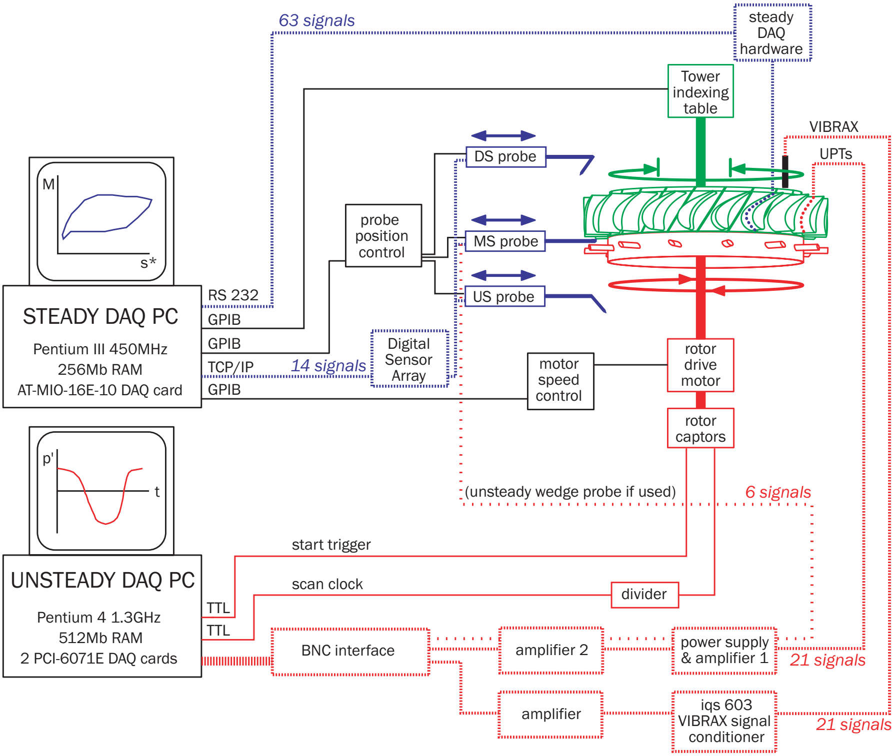

FIGURE 17. Schematic view of control systems & data acquisition (gust response setup)

The blade surface steady pressures are acquired using a multiplexer system, model JGMS6-48, made by Scanivalve Corp. This system has a total of 192 independent pressure inputs and can sample four pressures at a time. The pressure values are measured using four Digiquartz 2100 AT pressure transducers, manufactured by Paroscientific Inc. These transducers can measure absolute pressures up to 6.9 [bar] with a precision of ±0.5 [mbar]. The control of the multiplexer is accomplished using a multifunction I/O card, model AT-MIO-16E-10, made by National Instruments™. This card is installed in a Pentium III personal computer that is also used to store the acquired data.

The steady probe pressures are acquired using a digital sensor array, model DSA-3017, made by Scanivalve Corp. It incorporates sixteen temperature compensated piezo-resistive pressure sensors with a pneumatic calibration valve, RAM, 16 bit A/D converter, and a microprocessor in a compact self-contained module. The microprocessor compensates for temperature changes and performs engineering unit conversion. The microprocessor also controls the actuation of an internal calibration valve to perform on-line zeroing and multipoint calibrations. This on-line calibration capability virtually eliminates sensor thermal errors with a long term system accuracy of ±.05% [FS]. Pressure data are output in engineering units via Ethernet using TCP/IP protocol.

Time-varying voltage signals can be acquired from four different sources: (1) the blade surface unsteady pressure transducers, (2) the imbedded blade accelerometer, (3) the inductive displacement captors (VIBRAX) and (4) the unsteady wedge probe's unsteady pressure transducers. The measurement chain for each of these devices is illustrated in Figure 17. The pressure transducer signal passes through a pair of amplifiers connected in series. The first amplifier filters the DC signal component and applies a magnification of 10. This amplifier also supplies the 10 [V] necessary to power the attached transducer. The second amplifier applies a magnification of 1, 10, 100 or 1000. This selectable amplification setting facilitates the handling of larger input signals. Such signals can occur, for example, with the appearance of a shock near the pressure transducer location. It allows therefore the adaptation of each signal to the DAQ range optimizing the resolution of the acquired signal. The amplified signal is then input into a low pass filter with a cutoff frequency of 4 [kHz]. This pre-filtering of the higher frequency signal content reduces aliasing errors that can be produced during the post-acquisition FFT decomposition. The filtered signal is then input into the acquisition board, described later in this discussion.

The blade accelerometer signal passes through the same series of amplifiers as the unsteady pressure signals do but the first amplifier supplies the 15 [V] necessary to power the accelerometer, the second amplifier as no low-pass filtering and the amplification settings are adapted to each acceleration signal amplitude in order to maximize the resolution of the digitalization.

Each VIBRAX proximity captor is hooked up to a signal conditioner, model iqs 603 made by Vibro-Meter. Every output voltage signal then passes through an amplifier with variable magnification. This set of amplifiers is used in the VIBRAX calibration process to fix a constant blade movement sensitivity for all blades.

The time-varying analog signals described above are sampled and digitized using two PC-based acquisition cards, model PCI-6071E, manufactured by National Instruments™. Each card is capable of performing a multiplexed sampling of 32 independent channels with a maximum sampling rate of $1.25 \cdot 10^6$ [samples/s] divided by the number of channels acquired. The two cards are internally linked using a RTSI (Real-Time System Integration) bus cable. This hardware connection allows timing and synchronization signals to be shared between the acquisition boards. Specifically signals from an external start trigger and from an external scan clock source are shared directly on the boards, synchronizing the acquisition. The data acquisition is controlled by a Pentium 4 1.3 [GHz] personal computer using Labview™ 6.0i software interfaces. The acquired digital data is stored directly to hard disk and is later backed-up to CD-R. For a detailed description of the timing signal sources as a function of the type of measurement, the reader is referred to section 3.3.

2.9 Key Developments

A new blade suspension system has been designed, in combination with two separate metallic springs: one to have a pure bending motion and one to have a pure torsion movement of the blade, both with a common eigen-frequency. A new turbine measuring cascade has been assembled with twenty suspension systems from which nine support instrumented blades (six steady measuring blades, two unsteady measuring blades, one blade equipped with three accelerometers).

A rotor driven wake generator has been successfully designed and integrated in the non-rotating annular test facility of the LTT. The previous measuring cascade indexing system has been replaced by a more precise and rapid control system and is driven through a co-axial shaft in order to have the rotor driven separately. The rotor drive system permits to reach speeds of up to 3’000 RPM in both directions with the possible use of loaded blading. A specially built control system allows to synchronize the rotor speed with an outboard reference signal, in the present case, with a reference blade vibration signal.

Three new probe-holders, with precise displacement control systems, have been designed to investigate the steady flow conditions upstream of the wake generator, between the wake generator and the measuring cascade, and downstream of the measuring cascade. The control of the probes position, in combination with the indexing of the measuring cascade (on a common PC), allows an automation of the steady flow mapping measurements. A new digital sensor array, controlled by the same PC, allow a more precise and rapid acquisition of the probes steady pressures. Several four-holes wedge probes and five-holes L-probes have been fabricated and calibrated up to Mach 1.4 in a linear wind tunnel for the purpose of this investigation.

The non-rotating annular test facility has been totally overhauled and the pre-swirl vanes fixation systems have been replaced as well as their aging indexing system. The more precise hydraulic angular positioning of the pre-swirl vanes, in combination with the new lack of play on each of them, enables rapid and very precise flow conditions selection. Furthermore, the periodicity of the incoming flow is augmented and only several minutes are necessary to obtain previously used flow conditions as to hours in the past.

The blade vibration control system has been repaired and all twenty blades can be put into vibration separately with a common excitation frequency.

All the new systems have been designed, or selected, with the general idea of having two different PCs automate most tasks while still able to present rapidly intermediate results, in order to address the quality of the measurements quasi on-line. To free up enough computer power for post-processing while controlling the test facility, all the control systems are autonomous and only minimum information is transferred between them and the main PC. Figure 17 gives a good overview of this philosophy.

CHAPTER 3

Measuring Techniques

This chapter describes the measuring techniques used for all the different types of measurements carried out in this study. A special emphasis is made on describing the calibration processes, data reduction techniques and statistical analysis applied for each measurement type. These processes are the basis for the data acquisition and data reduction programs using Labview™ programming language.

This chapter closes with a summary of the key developments made in the measuring technique.

The user is referred to the previous chapter for a description of the hardware used in combination with the measuring techniques described hereafter.

3.1 Steady Aerodynamic Probes

The steady aerodynamic probes presented in section 2.7 were calibrated in one of the LTT's Laval nozzles (100 [mm] channel width). The calibration ranges for the pitch and yaw angles of all the probes are 25 and 20 [°], respectively. The probes have been calibrated up to Mach 0.9 except for the downstream probe that has been calibrated through the transonic regime and up to Mach 1.4. Five calibration coefficients are determined for each probe and then used during measurements to compute the flow properties (Mach number, pitch and yaw angles, static and total pressures) from the acquired probe pressures. For each measurement location (radial position and cascade index), the digital sensor array records fifty values per pressure tap and sends the averaged value to the data acquisition program. This latter reads in the averaged values until the standard deviation is less than one millibar ensuring stable flow conditions and precise results. The three probes are placed on three different probe-holders in order to avoid tainting downstream probe measurements with upstream probe flow interactions. Typical measurements comprise nine radial measuring positions (every 4 [mm]) and 28 circumferential locations (every 1 [°]; over a passage and a half). The corresponding measuring grid can be viewed in Figure 27 on page 70.

For more details on the actual calibration technique used, the reader is referred to [15] and [16]. A more general description on steady aerodynamic probe calibration can be found in [21].

3.2 Steady Blade Surface Pressures

For the steady measurements, the calibration procedure simply involves “zeroing” the pressure transducers prior to each measurement series. Specifically, this consists of reading the atmospheric pressure using an external device, and resetting each of the four pressure transducers to output this value. This calibration can typically be accomplished with a precision of ±0.1 [mbar]. The primary source of error associated with the steady-state pressure values is due to the settling time of the pressures. This error is estimated to be approximately ±0.5 [mbar]. The Labview™ based software interface controls the steady data acquisition system, reads in the differential values and display the blade surface pressure distribution as well as the computed blade surface isentropic Mach distribution. Measurements are made until these distributions remain constant.

3.3 Unsteady Data Acquisition Techniques

For this investigation, the overall approach applied to the acquisition of the unsteady data differs somewhat from methods used previously at the LTT. Former methods have generally employed the internal clock of the data acquisition card to trigger data sampling. This approach has the disadvantage of limiting the choice of sampling frequencies to factors of the maximum internal clock frequency. These frequency values rarely, if ever, correspond to the frequencies of interest for a given experiment. The end result is the presence of FFT leakage effects due to non-periodic samples, adding difficulties in detecting the main harmonics and introducing errors on the detected amplitudes and phases as well.

In the context of this investigation, the flow disturbances arise from imposed excitations, and hence the important signal frequencies are known a priori. To take advantage of this fact, the excitations (blade movement or rotor position) are utilized as external triggering sources for the unsteady data acquisition. Using this phase-lock data acquisition technique, one alleviates the problems associated with FFT leakage and ensures a high signal-to-noise ratio.

One drawback of this technique is that the sampling and triggering frequencies cannot be measured during the unsteady data acquisition but needs to be determined in another manner. For this purpose a first sub-program uses the data acquisition card's counters to measure the sampling and triggering frequencies just prior to the unsteady measurements. These two signals are measured until their variations are minimal, then the actual unsteady data acquisition can begin.

For controlled vibration experiments (see section 2.5), the oscillator's reference TTL signal (excitation signal in Figure 18) is input into a frequency multiplier device that applies a multiplication of sixteen. This in-house multiplier was designed and constructed for the purpose of this investigation and is based on a phase-locked loop circuit design. The multiplied signal is then connected to the acquisition card and serves as an external trigger control for the data sampling. During controlled vibration experiments, each rising edge of the scan clock source initializes the acquisition of a single sample for all attached data channels. This procedure is schematically represented in Figure 18. A total of 1536 periods are acquired on six consecutive scans for each acquired signal (21 unsteady pressure transducers, 20 displacement captors, 3 accelerometers) and directly stored on a hard media. After a Fast-Fourier Transform, each signal yields a frequency resolution of 0.03 [Hz] and a frequency range from DC to 2.1 [kHz] according to the Nyquist theorem. In most cases controlled vibration measurements in pure bending or torsion mode yield a pure sinusoidal pressure response on the blade surface avoiding the use of windowing on the FFT process. This technique combined with the high frequency resolution and range returns excellent signal-to-noise ratios and high precision on the detection of the fundamental harmonic present in each unsteady pressure signal.

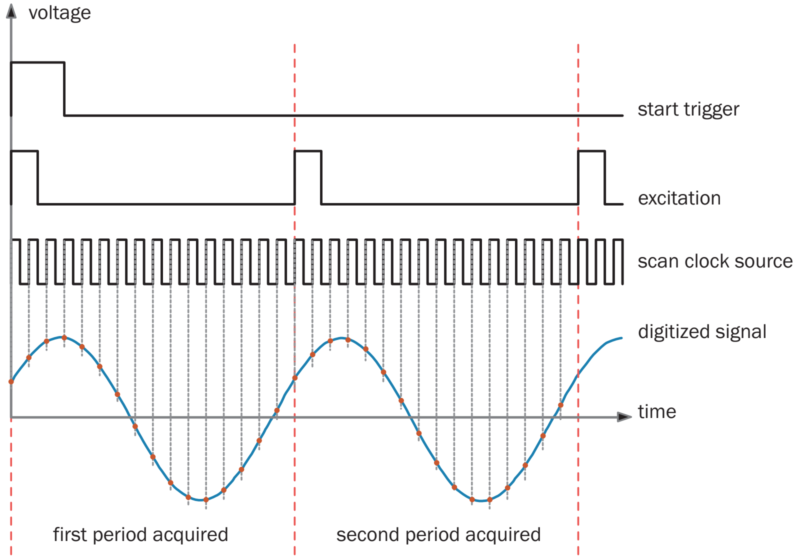

FIGURE 18. Unsteady data acquisition technique

For measurements using the rotating wake generator (gust response, superposition of gust response and controlled vibration) the data acquisition technique differs by the use of two encoders directly mounted on the motor and used as timing signal sources. The first optical encoder with one increment per revolution is used as start trigger source. It can be indexed at any position in order to set the start of the acquisition at a defined radial position of the rotating wake generator. The second custom-made encoder has 18'304 increments (13*22*64). Used in combination with a custom-built selectable frequency divider, the number of samples per period (between two consecutive struts) can be chosen between 2 to 64 for the engine order of 13 (13 strutted rotor), and between 2 to 128 for the engine order 22 (22 strutted rotor). With this technique the measured signals are acquired directly as a function of the position of the rotating wake generator filtering by design any speed variation of the rotor. This additional feature compared to the controlled vibration test setup augments considerably the quality of the acquired signals and simplifies the harmonic signal analysis further.

Typical measurements in the gust response setup consists of acquiring 65'536 samples per channel (21 unsteady pressure transducers) with 64 samples per period. The 1024 consecutive periods acquired for each channel are directly stored to a hard drive (burst mode). For measurements combining gust response and controlled vibration, the number of samples acquired per channel are reduced to the half of the forced response setup because of DAQ buffer limitations (21 unsteady pressure transducers, 20 displacement captors, 3 accelerometers). A FFT on each digitized signal yields a frequency resolution of 0.5 [Hz] (0.25 [Hz] for gust response) and a measuring bandwidth from DC to more than 8 [kHz], enabling the detection of more than ten harmonics. Due to the quality of the measuring technique, no windowing is necessary on the digitized signal prior to the FFT. As a matter of fact testing typical windowing techniques (Hanning, Hamming, Blackman, Blackman-Harris, Exact Blackman, Flat top, 4 term B-H, 7 term B-H, low Sidelobe) degraded the quality of the peak detection on either the amplitude or phase, or even both, during the harmonic signal analysis. This inverse effect compared to common signal processing knowledge is believed to be due to the particularly high periodicity between the excitation source and the digitalization.

The main sampling parameters used for the different measurement configurations are summarized in Table 6. The total number of samples acquired during controlled vibration measurements is lower than for the two other types of measurements for two reasons: first of all, the data acquisition technique for this type of measurements uses a custom-built frequency multiplier with a maximum multiplication factor of 32. Moreover, the acquired signals are pure sine tones that can be precisely detected using a limited number of samples. The difference in the total number of samples acquired between gust-response only and simultaneous gust response and controlled vibration measurements is a reflection of the limitation of the non-buffered data acquisition technique used in combination with the augmentation of the number of signals acquired in the simultaneous measurements.

Type of measurement	number of samples	number of samples per period	total number of periods	minimum frequency resolution [Hz]	maximum frequency detected [kHz]
Controlled Vibration	1536	16	96	0.03	2.12
Gust Response	65’536	64	1024	0.25	8.48
Combined GR & CV	32’768	64	512	0.5	8.48

TABLE 6. unsteady signal sampling summary

A sample of the Labview user interface for the unsteady data acquisition is shown in Figure 19. In addition to the acquisition process explained above, this interface also provides the possibility to visualize short time clips of the incoming raw voltage data. This is helpful for troubleshooting purposes, as well as to obtain a quick estimate of the signal amplitudes. In addition, a simplified data reduction can be applied to acquired raw data, and these results can be presented in the acquisition control panel. This is beneficial for obtaining a preliminary indication of the measured unsteady pressure amplitudes and phase angles.

An example of the data reduction software interface is presented in Figure 20 for controlled vibration and gust response measurements. Each step of the harmonic signal analysis is presented in three consecutive plots for each channel and then stored in a HTML file for control purposes. The first plot shows the raw amplitude spectrum and the harmonics detected. The second plot compares the raw time signal with its reconstruction based on the significant harmonics found. The last plot shows the dimensional raw time signal and the final calibrated unsteady pressure signal. Four additional plots present the cascade's vibration modes (amplitude and phases) for measurements using PS or SS unsteady instrumented blades as reference blade.

The corrections and calibrations processes carried on the digitized unsteady pressure signals are presented in the next section.

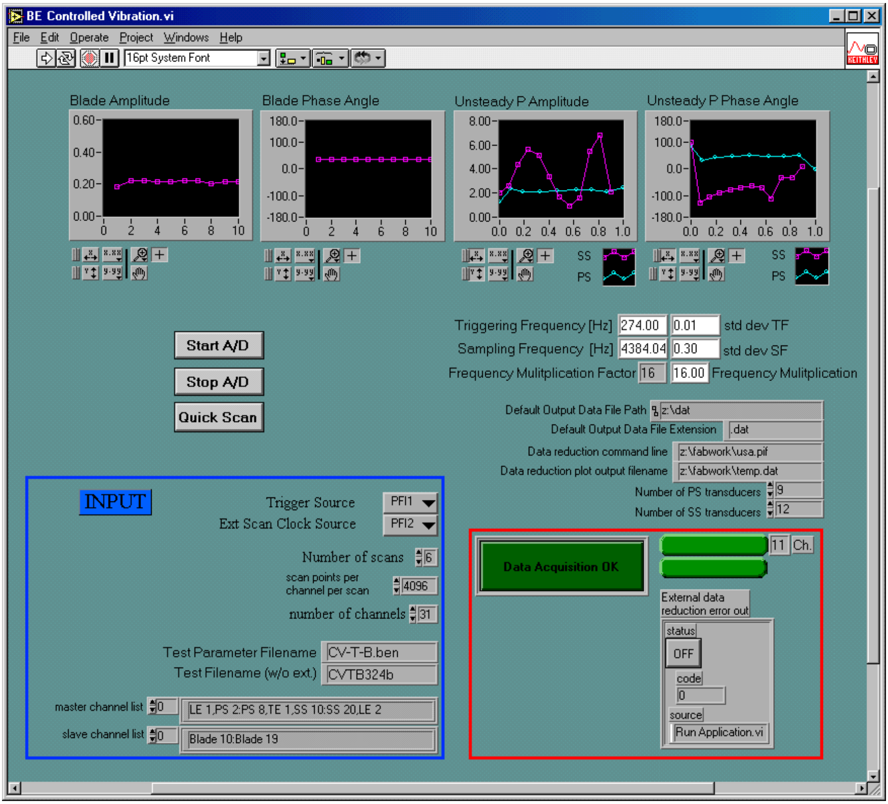

Triggering Frequency [Hz] 274.00 0.01 std dev TF

Sampling Frequency [Hz] 4384.04 0.30 std dev SF

Frequency Mulitplication Factor 16 16.00 Frequency Mulitplication

Default Output Data File Path z:\dat

Default Output Data File Extension .dat

Data reduction command line z:\fabwork\usa.pif

Data reduction plot output filename z:\fabwork\temp.dat

Number of PS transducers 9

Number of SS transducers 12

Trigger Source PFI1

Ext Scan Clock Source PFI2

Number of scans 6

scan points per channel per scan 4096

number of channels 31

Test Parameter Filename CV-T-B.ben

Test Filename (w/o ext.) CVTB324b

master channel list 0 LE 1,PS 2:PS 8,TE 1,SS 10:SS 20,LE 2

slave channel list 0 Blade 10:Blade 19

Data Acquisition OK

11 Ch.

External data reduction error out

status OFF

code 0

source Run Application.vi

FIGURE 19. controlled vibration DAQ software interface

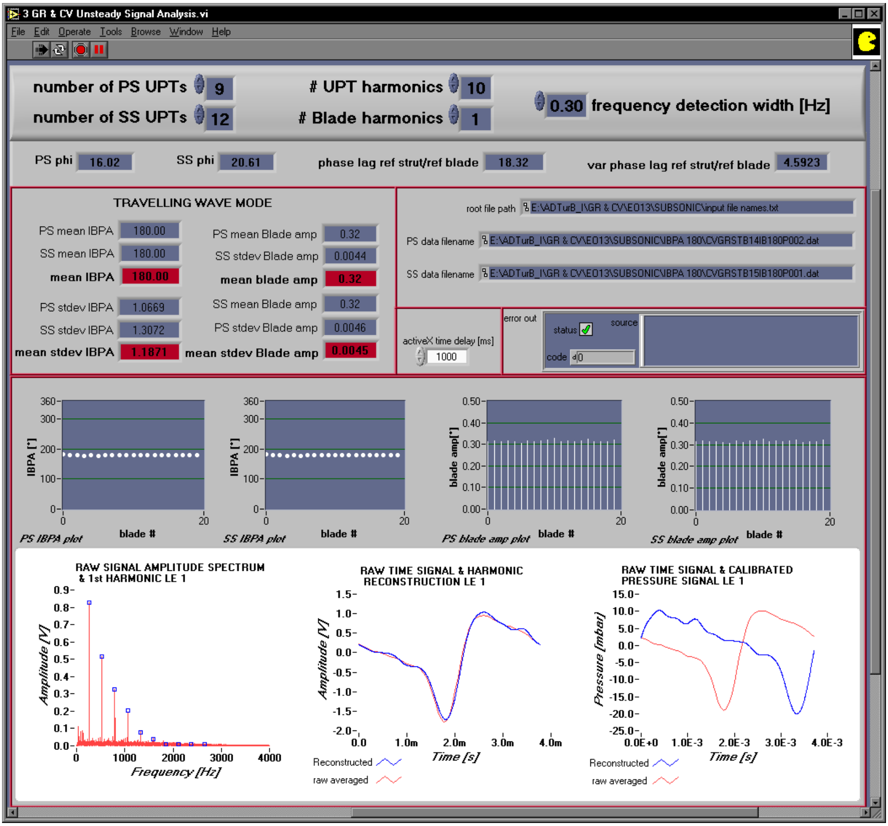

3 GR & CV Unsteady Signal Analysis.vi

number of PS UPTs 9

number of SS UPTs 12

UPT harmonics 10

Blade harmonics 1

0.30 frequency detection width [Hz]

PS phi 16.02

SS phi 20.61

phase lag ref strut/ref blade 18.32

var phase lag ref strut/ref blade 4.5923

TRAVELLING WAVE MODE

PS mean IBPA 180.00

SS mean IBPA 180.00

mean IBPA 180.00

PS stdev IBPA 1.0669

SS stdev IBPA 1.3072

mean stdev IBPA 1.1871

PS mean Blade amp 0.32

SS stdev Blade amp 0.0044

mean blade amp 0.32

SS mean Blade amp 0.32

PS stdev Blade amp 0.0046

mean stdev Blade amp 0.0045

root file path E:\ADTurB_I\GR & CV\E013\SUBSONIC\input file names.txt

PS data filename E:\ADTurB_I\GR & CV\E013\SUBSONIC\IBPA 180\CVGRSTB14IB180P002.dat

SS data filename E:\ADTurB_I\GR & CV\E013\SUBSONIC\IBPA 180\CVGRSTB15IB180P001.dat

activeX time delay [ms] 1000

error out

status ✓

code 0

source

FIGURE 20. combined gust response and controlled vibration data reduction software interface

3.4 Unsteady Blade Surface Pressures

From the digitized unsteady pressure signals stored on a hard drive during measurements, a series of corrections have to be applied in order to obtain the “true” unsteady pressure signals. The main UPT signal processing features are presented in Figure 21 in the order they are implemented in the data reduction programs. This illustration is followed by a description of the calibration and the corrections processes applied on the UPT signals.

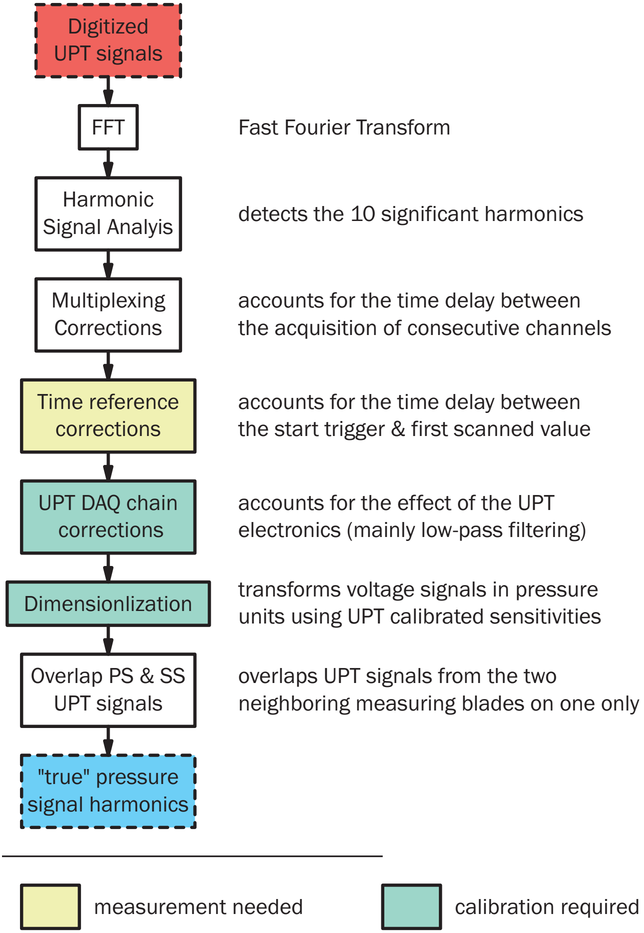

FIGURE 21. UPT data reduction process overview

The sensitivities of the unsteady pressure transducers are determined using a device which applies a periodic fluctuating pressure. This apparatus, illustrated in Figure 22, consists of a small hand-held device that is placed directly on the surface of the instrumented blade over the unsteady pressure tap. This device contains a small chamber that is open at one end and connected to an external source of fluctuating pressure at the other. The interface between the tap surface and the chamber opening is sealed with an o-ring. The fluctuating pressure within the chamber is measured simultaneously by a reference pressure transducer (ENDEVCO™ model 8534-50) and the transducer being calibrated. The two transducer voltage signals are input into a frequency analyzer, model HP35660A, made by Hewlett-Packard Co., and a comparison of both the amplitude and phase angle is made. The sensitivity of the given transducer is calculated based on this comparison and the known specifications of the reference transducer.

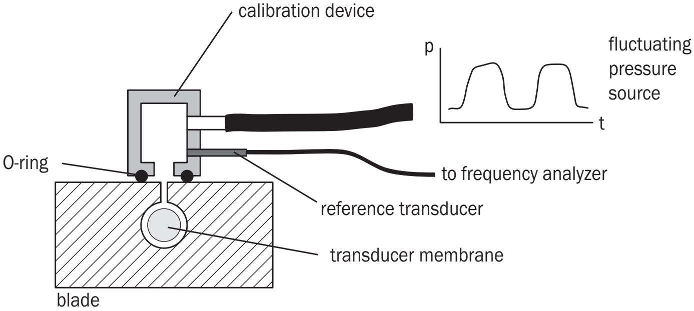

FIGURE 22. unsteady pressure transducer calibration technique

In general, this dynamic calibration procedure results in sensitivities less than 1% off those given by the manufacturer of the unsteady pressure transducers. The repeatability of such measurements are in the same order of magnitude. The low-pass filtering effect of the tap connecting the surface to the unsteady pressure transducer (see Figure 11 on page 40) has no influence on the measured bandwidth (250 [Hz] - 3 [kHz]). This dynamic calibration also showed that the small cavity drilled in front of the sensor has no effect on the unsteady pressure signals for these frequencies. Furthermore, the frequency response of the pressure transducers used is substantially superior to the minimum required for this investigation. Hence, in general these devices were found to exhibit little or no dependence on frequency over the range of experimental frequencies. The frequency dependency of the unsteady measuring chain is in fact almost entirely derived from the amplifiers and in particular from the imbedded low-pass filters. The evaluation of the amplifiers characteristics, therefore, represents a critical part of the unsteady calibration procedure specially if the unsteady pressure signals include several harmonics.

The UPT measuring chain is calibrated using a “periodic chirp” voltage signal input. This type of signal consists of a sinusoidal waveform with a periodically varying frequency. The measuring chain characteristic over the desired frequency range is determined by calculating the time-averaged frequency response function between the original and filtered “chirp” signals. This was performed using a frequency analyzer (model HP35660A). A typical set of UPT measuring chain characteristic is shown in Figure 23 with dots. In this example the nominal amplification is set to 1000 and the effect of the 4 [kHz] low-pass filter is that the amplification at 2.5 [kHz] drops to 500. Moreover, at this frequency the phase shift is close to 180 [°], inverting the original signal. This shows how critical the unsteady calibration procedure is for precise unsteady pressure measurements in turbomachinery.

Traditionally, the corrections are applied to the unsteady data at discrete frequency values (the harmonics detected) by fitting each time polynomial functions to the measured characteristics. The error introduced by this fitting method is approximately ±1 [%] on the local amplitude value for the damping corrections and ±1 [%] on the phase angle corrections.

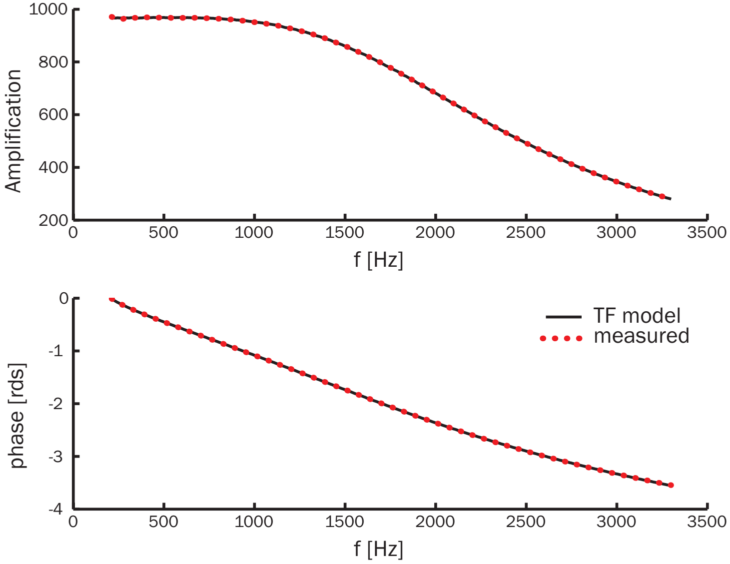

FIGURE 23. UPT DAQ chain characterization[1]

In this study a new procedure based on a transfer function modeling technique has been developed. The main advantages of such a technique, if a reasonable model can be found, are that only one equation is necessary to model both the amplification factor and phase angle information as a function of frequency. Moreover, if the harmonics found are represented as complex numbers, a simple multiplication by the inverse of the transfer function model will output the corrected values directly, accelerating considerably the data reduction procedure.

---

[1] *for visibility reasons only some of the 400 measured values are plotted.*

Good references on discrete time signal processing and modern spectral estimation have been written by Oppenheim [62] and Kay [47], respectively.

Several models have been tested with different numerator and denominator orders. The best transfer function model found is represented in equation (3.1) where a, b, c, d, e and f are the six complex constants to be determined from the measured characteristic vector Y(s) using a least square estimator. The final frequency response model is represented with a line on Figure 23 and exhibits very precise modeling of the measured data over the whole bandwidth.

$$G(s) = \frac{Y(s)}{U(s)} = \frac{a + \frac{b}{s} + \frac{c}{s^2}}{1 + ds + \frac{e}{s} + \frac{f}{s^2}} \qquad (3.1)$$

The absolute error between the model and the measured data, based on a nominal amplification of 1000, is represented on Figure 24. This error is less than 0.3% over the bandwidth where the ten harmonics of the measured unsteady pressure signals are to be found. Besides a considerable gain in precision this method is easier to implement and much faster in the correction process than the previous methods used. This modeling technique has been published by the author and is given in APPENDIX A. It describes in detail the modeling technique applied in this study.

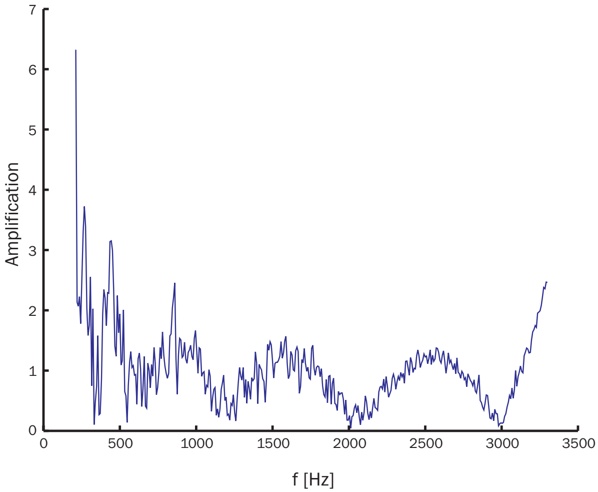

FIGURE 24. absolute error of the transfer function model in per thousand

The unsteady pressure transducers mounted in the blades are susceptible to blade motion effects. These errors appear as false pressure signals. Though particularly small in the present configuration where the displacement of the blade is parallel to the UPT's membrane (see Figure 11 on page 40), such errors are consistent for controlled vibration measurements and can be effectively suppressed. In general, this error is a linear function of the blade acceleration. These corrections can be determined by measuring the unsteady transducer output signals, as well as the blade accelerometer output, while the measuring blades are oscillating in a no flow environment (the surface taps are generally sealed with special tape during this procedure). These measurements are typically made for several different excitation frequencies. These acceleration corrections are applied to the unsteady data for a random frequency value by fitting polynomial functions to the measured values. The error signal is then subtracted from the measured data. The associated error is less than ±1% on total amplitude in terms of the amplitude correction, and less than ±2[°] for the phase angle correction (for the single harmonic of the pure torsion or bending mode).

One additional correction addresses the temporal effects introduced by the multiplexed unsteady data acquisition. As described in the previous section, the unsteady data acquisition is triggered externally. With each rising edge of the trigger signal, a single data point for all channels is acquired. These values are obtained in consecutive fashion, starting with the first channel and ending with the last. This method of acquisition, known as burst mode, is characterized by a fixed delay of approximately 3×10^{-6} seconds between the acquisition of consecutive signals within a single burst. For the measurement results, this difference is most significant for the higher frequencies and for the channels at the end of the channel list (noting that the first channels are commonly used as reference signals from which all phase angles are calculated). At 3 [kHz], the maximum phase angle error associated with this effect is approximately 8 [°] for the twenty-first channel. However, this error is well defined and can be effectively eliminated for each harmonic and each channel during the data reduction process.

One last correction addresses the temporal effect introduced by the time lag between the start trigger and the first scanned value determined by the first scan clock peak. Besides a time delay of less than a microsecond necessary for the DAQ hardware device to respond, an additional time delay is introduced by the relative positioning between the start trigger encoder and the scan clock encoder. In other words, a scan clock peak can never occur at the exact time the start trigger peak does. This time delay, varying with rotor speed, is measured using a digital oscilloscope and is generally between two and ten microseconds. An example is given in Figure 25 (start signal on channel 1 and scan clock source on channel 2). The associated corrections enable a common and precise time reference between the different measurements.

The last corrections deals with the fact that the unsteady blade surface measurements are conducted on two neighboring blade (PS and SS). In order to study the excitation effect over the blade profile it is necessary to overlap the unsteady pressure signals from one unsteady measuring blade over the other unsteady measuring blade. For controlled vibration measurements (travelling wave mode) and gust response measurements these corrections correspond to a time reference change for periodicity reasons. In the combined case, two sets of measurements are necessary with each time one of the unsteady measuring blade is used as reference and measured with. This is due to the fact that the phasing between the reference blade movement and strut passing frequency cannot be identical between two neighboring blades (combined effect of the engine order and inter-blade phase angle selection).

This calibration process compensates, to a great extend, all systematic errors on the unsteady pressure measurements using the described technique and hardware. Additional random errors cannot be accounted for but can be estimated through an averaging technique. In most measurement cases, 96 to 1024 successive periods are acquired per time-dependent signals. Collecting several measurements with the same test conditions and dividing each of the acquired signals into smaller time-periods before the data reduction is applied allows the use of a statistical approach to determine these random errors. For all the different test cases studied in this work, this error is inferior to ±1% on amplitude and ±1% on phase for a full scale data acquisition. This represents a maximum random error of ±0.4 [mbar] on the amplitude of the unsteady pressure signal. This random error is primarily due to variations of the mainstream flow conditions, the cascade’s vibration mode, the gust profile and secondary flow effects.

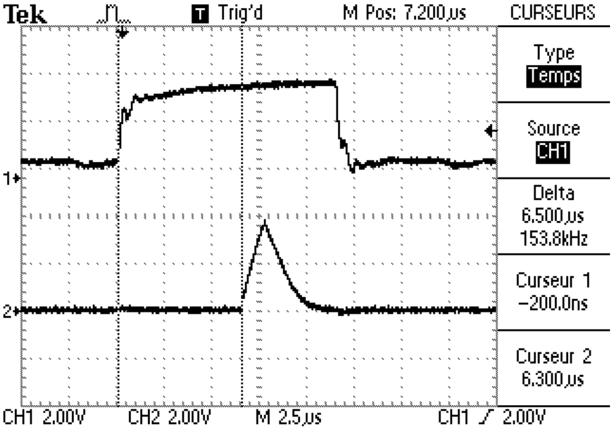

FIGURE 25. example of time delay between start trigger and first scanned value

3.5 Unsteady Aerodynamic Probe

An unsteady wedge probe developed by Oxford University [3] has been employed to measure the wake produced by the rotating struts (see Figure 16). The same data acquisition technique as for gust response measurements has been applied to unsteady wake measurements (see section 3.3). In this configuration, only the three unsteady pressure transducers of the probe have been acquired. Several measurements have been conducted to study the potential effect of the blade row, the effect of rotor speed variation as well as the effect of doubling the sampling frequency (128 samples per period, 32 [kHz] sampling frequency). A new optical encoder has been designed in order to increase the time resolution by a factor of two to sixteen. This will allow to enlarge the measurement bandwidth up to 300 [kHz].

3.6 Cascade’s Controlled Vibration Mode

Controlled vibration experiments consists of imposing a cascade vibration mode followed by the measurement of the induced pressure fluctuations on the instrumented blades. Commonly, all the blades are put into vibration with the same frequency, amplitude and a constant and periodic inter-blade phase angle (IBPA), whose definition is given in Figure 46 on page 88. It has been shown by Lane [53] that, for a cascade constituted of equally spaced identical blades, the IBPA can only take discrete values σ corresponding to a periodic IBPA:

$$\sigma = \frac{2 \cdot \pi \cdot n}{N} \tag{3.2}$$

where N is total number of blades of the blade row and n an integer such that: $0 \le n \le N$. Since the measuring cascade has twenty blades, periodic IBPA correspond to twenty multiples of 18 [°]. This particular mode associated with a constant vibration frequency and amplitude for all blades is called travelling wave mode and has the main advantage of being periodic over the vibrating annular cascade. It is important to notice that, compared to forced response measurements, the structural behavior of the cascade (damping and coupling) isn’t accounted for in this type of measurements. Furthermore, even if the cascade is mistuned in damping and frequency, the cascade’s vibration control system imposes the travelling wave vibration mode.

The design of the blade suspension system (see section 2.4) defines the blade vibration mode and determines the testing frequency for controlled vibration measurements. This frequency has to be close enough to the eigenfrequencies of the blade suspension systems in order to have high enough responses to the electromagnetic excitations. Limitations on the blade vibration amplitudes are given by the instrumented blades, in particular steady pressure taps equipped blades, whose mechanical damping can be up to ten times greater than non-instrumented ones. Furthermore, the testing frequency must avoid exact matching with the eigenfrequencies of the blade vibration systems in order to hinder resonant vibrations since the blade vibration control system cannot damp the blade movement.

The calibration process of the cascade vibration control system mainly consists of setting each of the VIBRAX amplifier to a certain sensitivity: a reference accelerometer (Brüel & Kjaer type 4375) is set on a blade which is put into vibration without control at a constant amplitude. Both signals are then compared using a dynamic signal analyzer and the VIBRAX amplifier is adjusted to give a predefined factor between the amplitude of these displacement signals. This procedure is repeated for all blades each time the blade suspension system configuration is changed.

During measurement, the twenty blades are set to vibrate in the travelling wave mode with one selected periodic IBPA. The vibrations amplitudes are all monitored on an oscilloscope and the phase controller indicates with the use of LEDS if the blade movements are in phase with their assigned reference signals. As soon as a stable travelling wave mode is obtained, unsteady measurements are conducted (see section 3.3). This procedure is repeated for the twenty different periodic IBPA if these modes are stable.

If the influence coefficient technique is applicable, the travelling wave measurements can be mathematically reconstructed from single blade vibration measurements (see APPENDIX B). These simplified measurements consist of vibrating one blade at a time and measuring its vibration effect on the unsteady pressure measuring blade. The validity of this other linear superposition principle can be validated by comparing the influence coefficients obtained from single blade measurements with the one computed from travelling wave measurements (see Figure 97 and Figure 98 on page 156). These latter measurements constitute a set of linear equations that can be solved using matrix algebra in order to get the complex influence coefficients associated with each blade, as defined in equation (B.4) on page 153.

3.7 Key Developments

The main development in the measuring techniques is the design of a multi-channel high frequency data acquisition system synchronized with the rotor via a custom built high resolution encoder. The synchronization feature allows to physically filter all rotor speed variations in the unsteady measurements by adapting the sampling to the actual position in time of the rotor. Used in combination with a custom built frequency divider, this encoder allows the sampling of the unsteady signals with various time resolutions. A second encoder permits the triggering of the data acquisition with a reference strut's position and, therefore, each consecutive wake measured can be attributed to a specific strut. A great effort has been carried out in the calibration process and in the unsteady signal post-processing in order to have a very precise determination of the harmonic content up to more than ten sub-harmonics. More specifically, all time-delays present in the data acquisition chain have been accounted for and a very precise modeling of the electronics effect on the signal has been developed using a transfer function modeling technique.

Other developments on the measuring techniques mainly consisted of upgrading the steady acquisition programs to Labview™ and implementing a modernized algorithm for the determination of the flow quantities from the probes calibration curves and from probe measurement data.

All data acquisition and post-processing programs have been written using Labview™ programming language with modular sub-structures for ease of future developments.

CHAPTER 4

Steady-State Flow

This chapter presents the steady-state results for two different flow conditions: a subsonic test case and a transonic test case, both close to blade profile design conditions. These measurements, consisting of steady aerodynamic probe measurements as well as blade surface pressure measurements, were aimed at having identical quasi-two-dimensional steady-state flow conditions between controlled vibration measurements, gust response measurements and for the superposition of these two sources of unsteady pressures. These conditions are necessary in order to focus on the superposition of the unsteady aerodynamic sources studied in this work. Furthermore, these conditions permit the use of quasi-two-dimensional numerical codes with great accuracy and limited simulation times by modeling streamtube height variations. The quasi-two-dimensional flow assumption is verified for all test cases and the effects of secondary flow is addressed and discussed in detail. A comparison of the steady-state results between the different test configurations is presented as well. For a description of the experimental apparatus and the measuring techniques associated with these steady-state results, the reader is referred to chapter 2 and chapter 3, respectively.

After a presentation of the flow parameters and their definitions, this chapter starts with a comparison of the averaged flow conditions for the three different test configurations consisting of:

- the measuring cascade only.
- the measuring cascade with the engine order 13 rotor.
- the measuring cascade with the engine order 22 rotor.

The next section presents the mainstream flow conditions in three dimensions and the analysis of the secondary flow effects. It is followed by a presentation of the blade surface isentropic Mach distributions for both flow cases and all three test configurations, including their analysis. Finally this chapter closes with a short summary of the key findings.

4.1 Definitions

This section describes the flow parameters used to present the steady-state results. The steady pressures are commonly expressed in terms of the isentropic Mach number M, defined as:

$$M = \sqrt{\frac{2}{\gamma - 1}\left[\left(\frac{p_{t1}}{p}\right)^{\frac{\gamma - 1}{\gamma}} - 1\right]} \tag{5.1}$$

where p is the static pressure measured at a given location, p_{t1} is the upstream total pressure, and γ is the ratio of specific heats for air (γ =1.4).

Considering an cylindrical coordinate system with x, y (or rθ) and z being the axial, circumferential and radial directions, respectively, the isentropic Mach vector can be expressed as (u,v,w) or as (M, β, φ) where β is the relative flow angle and φ the radial deflection angle as illustrated in the following figure. The steady-state results presented in this chapter are represented as (M, β, φ). Indices are used to differentiate the three axial probe measurement planes. Figure 7 on page 36 shows the three probe measurement locations and their respective indices.

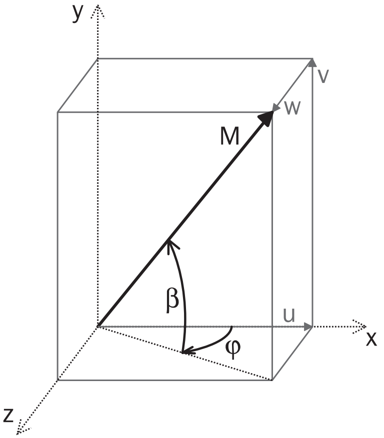

FIGURE 26. reference coordinate system and flow variable definitions

4.2 Average Flow Conditions

As described in section 1.4 and 2.3, the design of the measuring cascade and the rotating wake generator aimed the same relative flow conditions as the one obtained at midspan, and at design conditions, on the DLR Göttingen ADTurB test rig. These design conditions consist mainly of a relative outlet Mach number of 0.9 with a relative inflow angle of 45 [°]. In this configuration a transonic pocket (in the relative frame of reference) is present on the suction side of the turbine blade. In addition to this transonic test case, a second case corresponding to an operating point with reduced rotor speed on the DLR rig is studied and called subsonic test case.

For each flow condition, three different test configurations are necessary in order to study the superposition of gust response and controlled vibration:

- measuring cascade alone (no rotor) for controlled vibration measurements only.
- measuring cascade with the 13 strutted rotor (EO 13) for gust response and superposition measurements.
- measuring cascade with the 22 strutted rotor (EO 22) for gust response and superposition measurements.

The average flow conditions for these three configurations are given in Table 7 for the subsonic test case and in Table 8 for the transonic test case. The averaged values and the associated standard deviations are based on three measurement locations around mid-blade height in the radial direction and over one passage (18 [°], every 1 [°]) in the circumferential direction. This data is taken from the flow mapping measurements presented in section 4.3.

For each test case, matching flow conditions between test configurations focused on meeting the blade surface pressure distribution (see section 4.4) as well as the average inlet and outlet flow conditions.

As shown in the next table, the average flow conditions match well between the three test configurations of the subsonic test case. Most flow conditions are identical between runs. Main trends consist of a slight augmentation of all total and static pressures with the increase of the number struts. This is due to the rising total inlet pressure necessary to counter the augmenting aspect ratio of the wake generator and getting similar blade surface pressure distribution between these three configurations. Differences are mainly observable on the relative flow angles upstream and downstream of the measuring cascade ($\beta_{2,3}$ and β_4). As a matter of fact the insertion of the rotating wake generator diminishes the potential effect[1] of the measuring cascade observable upstream of it (position 2,3). This is clearly visible on the “midstream” flow mapping results in Figure 30 and is further discussed in the next section.

The standard deviations based on 54 samples (except for T_{t1}) show that statistically inflow conditions are constant over the averaging grid (3*18) to a good precision. Of course, “midstream” and outflow averaged conditions vary to a larger scale mainly due to potential and wake effects as indicated by higher standard deviations at these two axial locations.

---

[1] *This effect is combined with leakage flow effects as described in the following section.*

VARIABLE		NO ROTOR		EO 13		EO 22		TREND
name	units	value	std. dev.	value	std. dev.	value	std. dev.	
T_{t1}	[K]	296	±2	299	±2	299	±2	=
p_{t1}	[mbar]	1238	±4	1251	±3	1283	±3	+
$p_{t(2,3)}$	[mbar]	1235	±3	1245	±2	1276	±2	+
p_1	[mbar]	1139	±3	1151	±2	1179	±2	+
$p_{2,3}$	[mbar]	1154	±8	1167	±8	1196	±9	+
p_4	[mbar]	890	±10	903	±11	908	±13	+
M_1	[]	0.35	±0	0.35	±0	0.35	±0	=
$M_{2,3}$	[]	0.31	±0.02	0.31	±0.02	0.31	±0.02	=
M_4	[]	0.67	±0.06	0.66	±0.05	0.69	±0.04	~=
β_1	[°]	46.7	±0	46.7	±0.1	46.8	±0.1	=
$\beta_{2,3}$	[°]	49.4	±3	45.8	±3	45.2	±3	-
β_4	[°]	-56.9	±3	-58.3	±2	-59.1	±2	++
φ_1	[°]	-0.7	±0	-0.6	±0.2	-0.6	±0.2	=
φ_4	[°]	5.1	±3	4.7	±3	4.5	±3	-

TABLE 7. comparison of averaged flow conditions for the subsonic test case

The averaged flow conditions for the transonic test case, presented in Table 8, exhibit similar trends between the three different configurations as for the subsonic test case. Again most flow variables are almost identical and mainly all pressure values have a tendency to augment as the number of inserted struts passes from 0 to 13 and then to 22. This time the potential effect upstream of the measuring cascade is less influenced by the presence of the rotating wake generator as shown by the “midstream” relative flow angle ($\beta_{2,3}$) that doesn’t drop as much as for the subsonic test case.

The relatively low dispersion of inflow values, as standard deviations indicate, reflects again constant inflow conditions over the averaging grid. The overall rise of the standard deviations (factor of two) between the inflow conditions of the two test cases is an indication of the augmentation of the turbulence level, as one would expect. Of course, the wakes generated in the transonic test case have greater potential and vortical effects (same struts used) than in the subsonic test case yielding even higher dispersion in the measured values, in particular for the downstream static pressure p_4.

Looking at the deflection angle φ for both flow conditions show that in both cases the flow has a tendency to deviate in the radial direction as it passes through the measuring turbine cascade. This is due to the fact that the annular cascade is composed of prismatic blades and therefore the aspect ratio of the turbine profile diminishes with increasing radial values. This is further addressed in the following section.

VARIABLE		NO ROTOR		EO 13		EO 22		TREND
name	units	value	std. dev.	value	std. dev.	value	std. dev.	
T_{t1}	[K]	303	±3	303	±3	304	±3	=
p_{t1}	[mbar]	1589	±6	1597	±5	1639	±6	+
$p_{t(2,3)}$	[mbar]	1592	±6	1597	±3	1637	±5	+
p_1	[mbar]	1427	±5	1434	±6	1473	±4	+
$p_{2,3}$	[mbar]	1451	±18	1461	±18	1504	±14	+
p_4	[mbar]	871	±27	895	±23	873	±40	
M_1	[]	0.4	±0	0.39	±0.01	0.39	±0	=
$M_{2,3}$	[]	0.37	±0.02	0.36	±0.02	0.35	±0.02	-
M_4	[]	0.95	±0.08	0.93	±0.06	0.98	±0.07	~=
β_1	[°]	47.5	±0.3	47.6	±0.4	47.4	±0.3	=
$\beta_{2,3}$	[°]	48	±4	46.9	±3	46.6	±3	-
β_4	[°]	-57.6	±3	-58	±3	-58.9	±3	+
φ_1	[°]	0	±0.1	0.1	±1	-0.2	±0.1	=
φ_4	[°]	6	±2	6	±3	6	±3	=

TABLE 8. comparison of averaged flow conditions for the transonic test case

One can concluded from the presented average data that the three different test configurations exhibit very close mainstream flow conditions in the middle of the test section for both test cases.

Averaging the main flow properties over the three different test setups yields the following table of global averaged data.

test case	T_{t1} [K]	p_{t1} [mbar]	p_1 [mbar]	p_4 [mbar]	M_1 []	M_4 []	β_1 [°]	β_4 [°]
subsonic	298	1257	1156	900	0.35	0.67	46.7	-58
transonic	303	1608	1445	880	0.39	0.95	47.5	-58

TABLE 9. global averaged flow conditions for subsonic and transonic test cases

4.3 Mainstream Flow Conditions

As described in section 1.4 and 2.3, mainstream flow conditions measurements are conducted using steady aerodynamic probes at three different axial positions: upstream of the wake generator, between the rotating struts and the measuring cascade ("midstream" measurements), and downstream of the blade row. Nine equidistant measurements are conducted in the radial direction over two passages (36 [°] every 1 [°]) for the configuration without the wake generator and over a passage and a half when using either wake generators (EO 13 and EO 22).

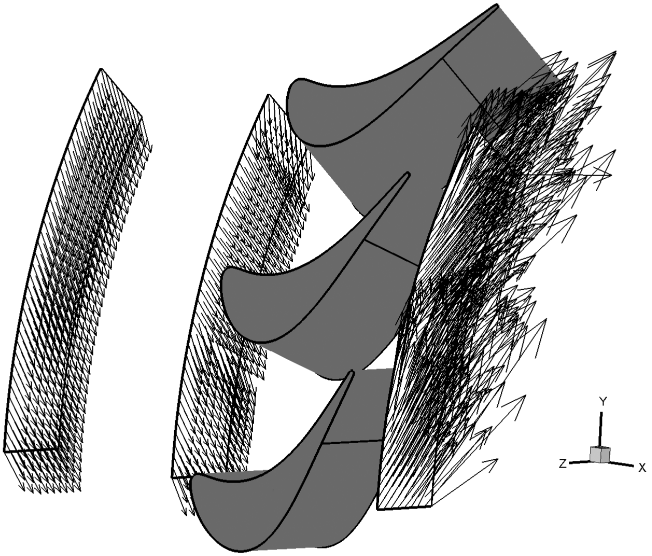

FIGURE 27. mainstream flow vectors, transonic test case, no rotor

In Figure 27 an example of steady aerodynamic probe measurements is given for the transonic test case with no rotor and presented as flow vectors. In this three-dimensional view one can observe that the inflow conditions are constant over the whole measuring grid. At the midstream location the potential effect of the blade row is indicated by the deviation of the flow vectors in the passage flow near the suction side of each blade. Otherwise the flow is constant at this axial location[1] and is comparable to the inflow conditions. Besides the expected deviation and acceleration, the downstream flow measurements exhibit important three-dimensional flow effects to be further analyzed in this section.

In Figure 30 on page 75 the freestream isentropic Mach distribution for the subsonic test case is presented as contour plots for the three axial measurement positions and the three test configurations. The upstream measurements show uniform inflow conditions for all test configurations with just one radial strip exhibiting slightly higher velocities. In fact this difference is due to the scaling and the choice of legend. Since the average inflow Mach number is of 0.35 and the contour level change is at the same limit, small variations of speed around this value will come out as different color levels, magnifying variations around this threshold. The uniformity of the inflow conditions is confirmed by the average results of Table 7 and the 3D visualization of the mainstream flow vectors[2]. Nevertheless this pattern suggests a slight effect of the two separate inlet flows produced upstream of the radial-axial nozzle of the test facility (see Figure 6 on page 34) and is confirmed by static pressure visualization.

The midstream results show uniform flow conditions at this location except for a C-shaped zone of higher velocities situated just in front of each blade in the mainflow direction ($\beta = 45$ [°]). This effect is magnified and presented for the subsonic test case without rotor in Figure 28 as an example. One would expect a rise in static pressure in front of each blade's leading edge along the whole blade height with decreasing intensity along the axial direction since the passage width increases as well (prismatic blades in an annulus).

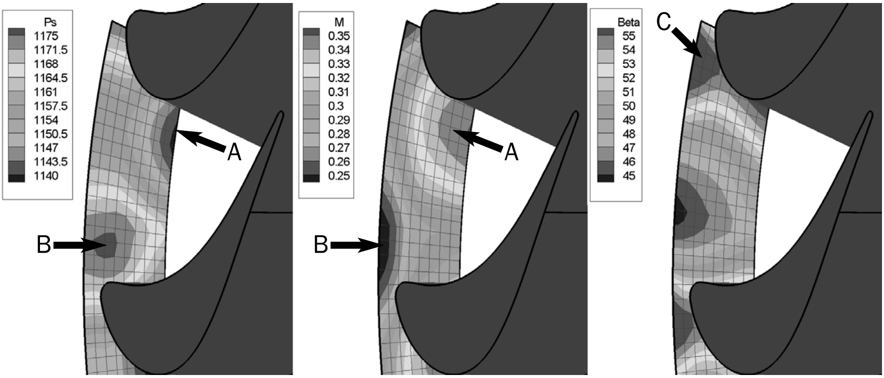

FIGURE 28. potential and leakage flow effects of blade row, subsonic test case, no rotor

---

[1] *N.B. The four-hole steady wedge probe used at the midstream location only measures two-dimensional flows.*

[2] *The chosen legend optimizes the visualization of the potential effects and downstream flow structures.*

In fact this potential effect is only visible near the casing as indicated by zone B in Figure 28. The lack of potential effect near the hub seems to be due to another effect as suggested by the unexpected A zone. In this region a static pressure drop is visible with the associated increase in Mach number. This zone and the lack of potential effects near the hub suggests the presence of leakage flow in this region. In order to let the blade suspension system vibrate freely, the blade base design is such that a 1.5 [mm] gap surrounds it. Even if this gap is followed by a kind of labyrinth seal (see Figure 8 on page 37), the air seems to enter upstream of the measuring cascade in the gap between the upstream inner wall and the blade bases as illustrated in Figure 36 on page 80. Unfortunately the steady wedge-probe measurement at this location doesn’t include the velocity component in the radial direction which would confirm or not the leakage flow effect near the hub. As a matter of fact the relative flow angle β exhibits quasi constant deviations along the blade height (C zone in Figure 28) like one could expect from pure potential effects. But the deviations near the hub could be produced by the leakage flow (particularly in the gap between neighboring blade bases), accelerating and deviating the flow in this region in the same way as potential effects.

The downstream results for the subsonic test case (Figure 30) show good periodicity over the measured passages for all three test configurations and exhibit very similar patterns between them. Besides a main accelerated flow (yellow and orange contours) several effects near the hub and near the casing appear and seem to interact with the blade’s wakes. Near the hub two different zones are present: a low velocity region (in blue) along three quarter of each passage and a high velocity one (in red) that emanates from the hub and fades in the main flow. These two effects are believed to be originated by the leakage flow through the gaps surrounding the blade bases as suggested in Figure 37. As illustrated earlier in this section air seems to leak inside the measuring cascade upstream of the blades through two different types of orifices: the gap between the inner walls and the measuring cascade (upstream and downstream of the measuring cascade as illustrated in Figure 13 on page 42), as well as the gap between neighboring blade bases (Figure 29).

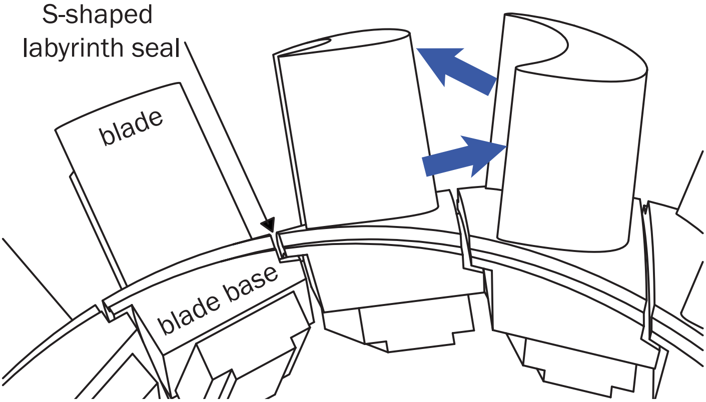

FIGURE 29. S-shaped labyrinth seals between neighboring blade bases

The passages associated with these openings are different in nature and should account for their different effects observed downstream of the cascade. The gaps between the inner walls (#11 and 12 in Figure 13 on page 42) and the blade bases (#4) is rather narrow and the direction changes are important (~ twice 180 [°]) as opposed to the labyrinth seal between neighboring blade bases where the main flow is deviated almost parallel to the slot and where the turning much smaller (~ twice 90 [°]) on a larger spacing. Even if both leakage flows must interact in the inner spacing of the measuring cascade these differences suggest two leakage flow effects:

- a low mass flow rate leakage flow entering through the gap between the upstream inner wall and the measuring cascade and being injected through the gap between the downstream inner wall and the measuring cascade with low velocity and almost radially (yellow arrows in Figure 37 on page 80).
- a high mass flow rate leakage flow that penetrates the spacing between neighboring blade bases in the LE region and then being reinjected in the main flow through the same gap but near the TE, accelerated by the static pressure change (light blue arrows in Figure 37 on page 80).

This difference in leakage flows is confirmed by the total pressure distribution downstream of the blade row (Figure 34 on page 79) where important losses are observed only for the low mass flow rate leakage flow.

The other secondary flow effect observed near the casing and that interacts with the blades wakes (light green region) is due to tip gap vortices as attested by the sidewall isentropic Mach distribution of Figure 36 on page 80. In this figure one sees that the difference in static pressure between the pressure and the suction sides of each blade drives a flow that accelerates beyond the transonic regime as it passes through the 0.5 [mm] tip gap (1.25 [%] of the channel height) and decelerates as it leaves this spacing as illustrated by the black arrows. The divergence of outflow angles between this secondary flow as it exits the tip gap and the mainflow (illustrated with the blue arrows) is of around 20 [°] and is the source of the tip gap vortex generation. The effect of this vortex is also visible on the total pressure distribution of Figure 34 and is schematically represented in Figure 37 on page 80. Numerous references on tip gap vortices in turbomachinery can be found in the literature.

Figure 32 on page 77 presents the velocity vectors of the subsonic test case without rotor at three different radial positions in order to view the secondary flow effects. The tip gap vortices distort the flow vectors in a rather smooth manner suggesting that they are stable over time. On the contrary, leakage flow effects near the hub exhibit unstable flow conditions since large variations on velocity direction and intensity as well as values out of the calibration range of the steady aerodynamic probe (represented with no vectors) can be seen. Furthermore if one considers the gap geometry between the measuring cascade and the downstream inner wall one can understand that radial low-momentum flow injection must produce great instabilities and high levels of turbulence. Nevertheless two zones with higher velocities than the mainflow and with a slight component in the radial direction can be observed, especially for the transonic test case in Figure 33 on page 78.

Besides an expectable evolution of the flow conditions the transonic test case results exhibit similar flow patterns to the subsonic test case but with noticeable higher leakage effects. This time the so-called high mass flow rate leakage flow extends along the whole length of the blade. This is probably due to a combined augmentation of both leakage flows where the low-momentum leakage flow as an accelerating effect on the nearby flow as one can observe in Figure 31.

One additional effect not present in the subsonic test case is the appearance of a small high velocity zone (in red) in the middle of the through flow region and at about three quarter blade height, specially present in the EO 22 results. This local acceleration of the flow must be produced by the tip gap vortex creating a nearby local deviation of the flow towards the casing and an associated expansion of the passage flow as suggested in Figure 33 on page 78.

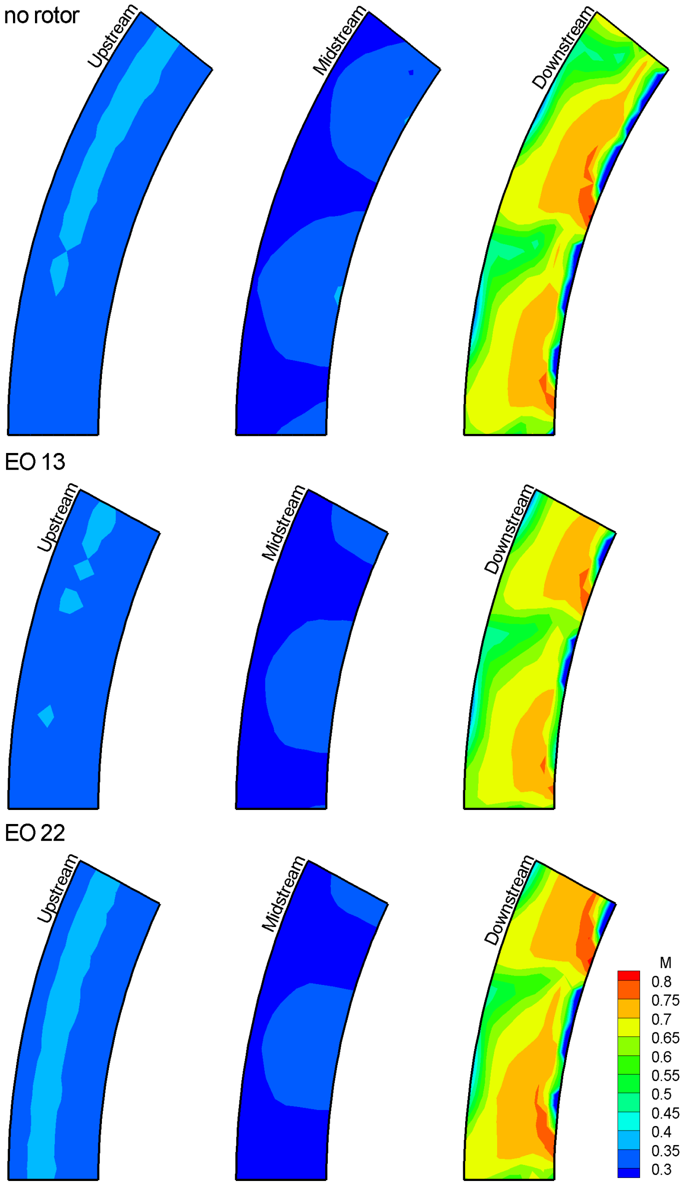

FIGURE 30. mainstream Mach number distribution, subsonic test case

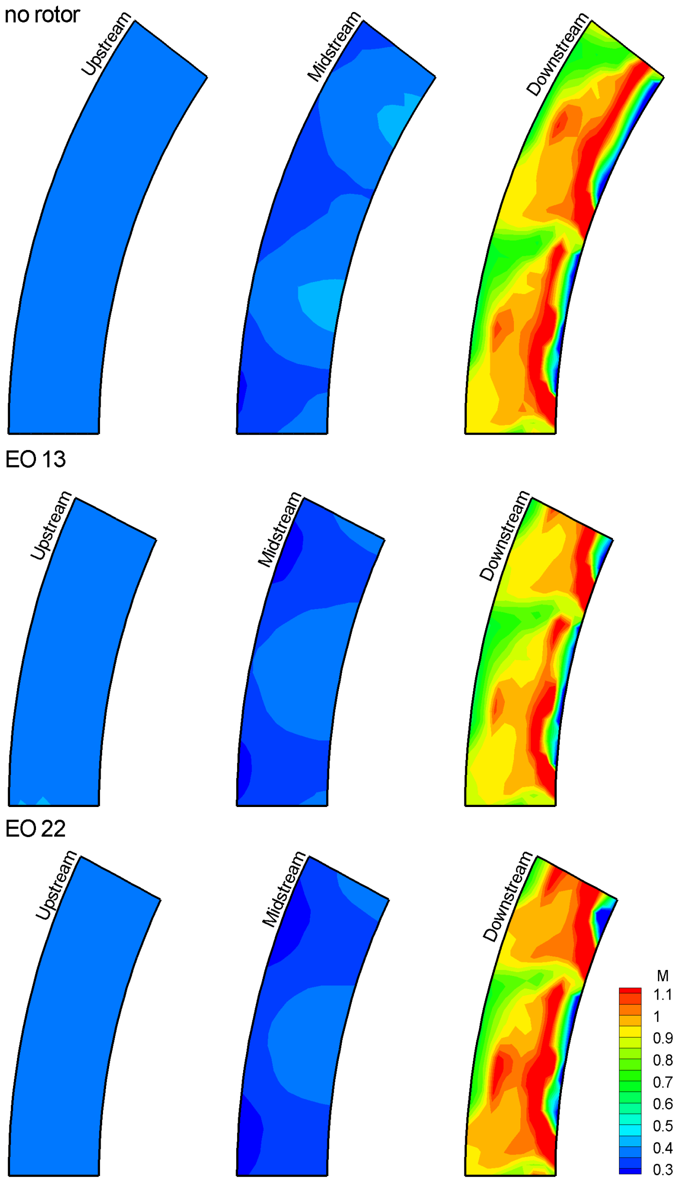

FIGURE 31. mainstream Mach number distribution, transonic test case

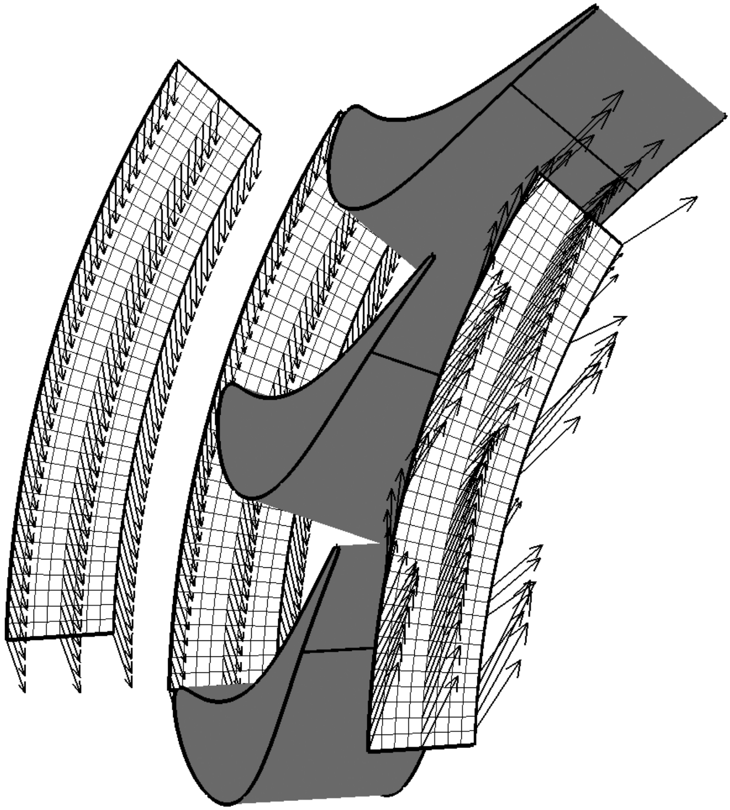

FIGURE 32. secondary flow example (subsonic test case, no rotor)

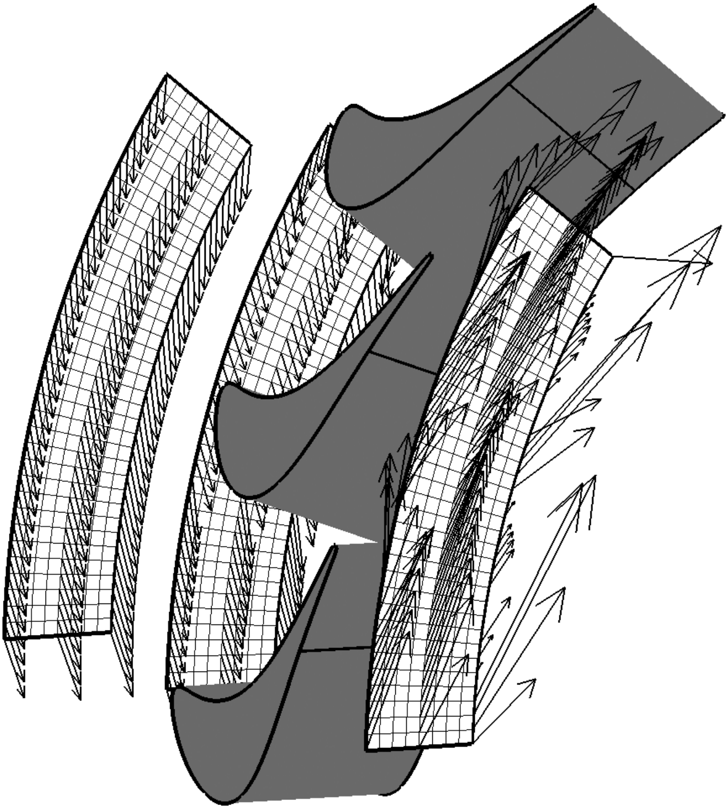

FIGURE 33. secondary flow example (transonic test case, no rotor)

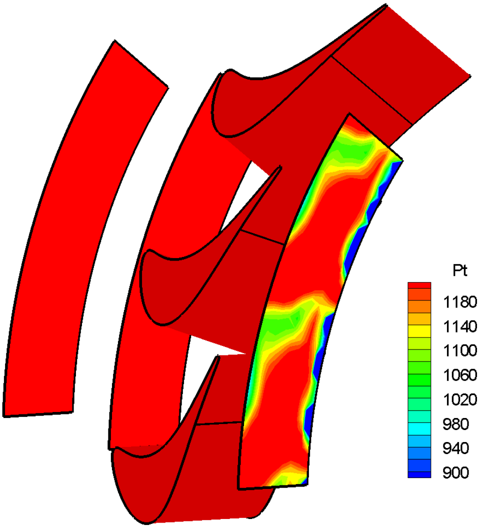

FIGURE 34. total pressure distribution (subsonic test case, no rotor)

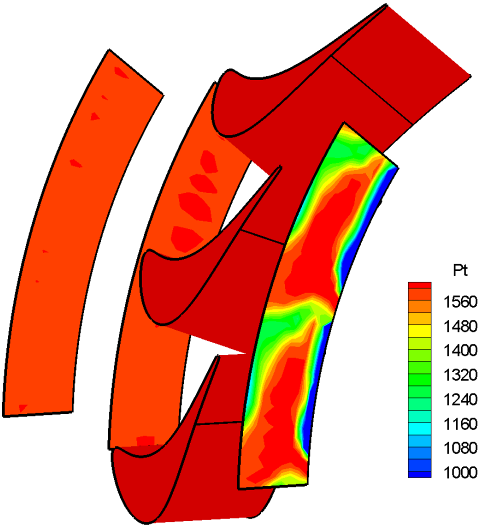

FIGURE 35. total pressure distribution (transonic test case, no rotor)

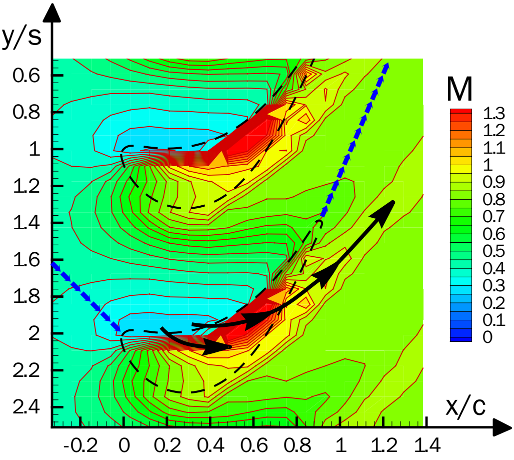

FIGURE 36. sidewall isentropic Mach number distribution (transonic test case, no rotor)

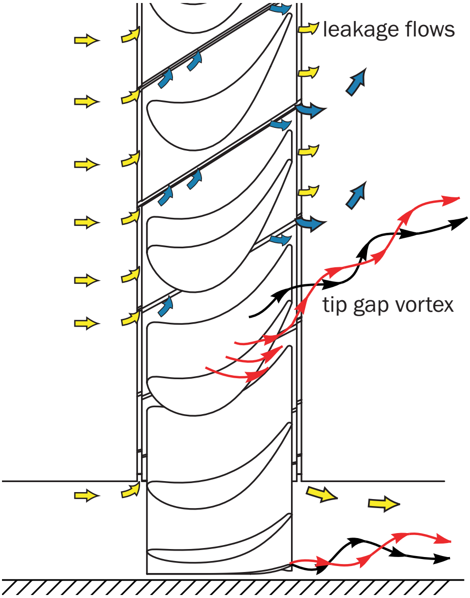

FIGURE 37. schematic view of secondary flows

4.4 Blade Surface Isentropic Mach Distribution

The blade surface isentropic Mach distributions (without rotor) as a function of the non-dimensional curvilinear location s*, at the three radial measuring positions for the subsonic test case and the transonic test case are presented in Figure 38 and Figure 39, respectively. At first glance, the combination of an exponential acceleration of the flow on the pressure side and a logarithmic acceleration of the flow on the suction side is a reflection of the steady lift of the blade represented by the surface delimited by these two curves as one would expect from the design of a turbine blade[1]. Comparing these evolutions for the three different radial measurements locations (20%, 50% and 90% blade height) show several discrepancies in the quasi-two-dimensional flow assumption. The secondary flow effects, detected and described in the previous section, are the source of the main observable discrepancies, as demonstrated below:

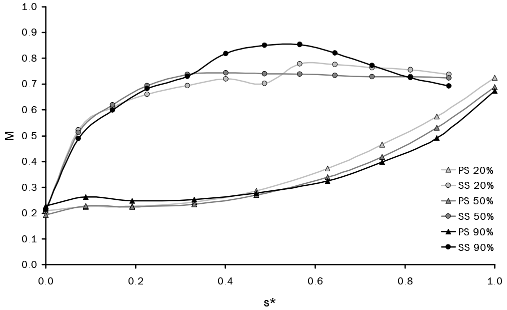

FIGURE 38. blade surface isentropic Mach distribution, subsonic test case, no rotor

The effect of tip gap vortex can be seen on the measurements conducted near the blade tip. At this radial location this secondary flow originated by the difference in static pressures between the pressure side of the blade (near the LE) and the suction side (s*=0.5) accelerates in these two regions more than the flow at mid-channel height. This is particularly visible on the suction side with the presence of a hump and is confirmed by comparisons with the sidewall isentropic Mach number distribution of Figure 36 on page 80 for the transonic test case. As one would expect this local acceleration and deceleration is more important and occurs further down on the surface as the upstream/downstream static pressure difference rises for the transonic test case.

The effects of the leakage flow through the core of the measuring cascade and described in the previous section can be observed on the measurements conducted near the blade base. At this radial location, both PS and SS surface flows accelerate more than the mid-channel height flow starting from s*=0.5 to the TE. On the PS this evolution is progressive but on the SS the isentropic Mach number jumps from 0.7 to 0.8 at s*=0.55. This difference is attributed to the location of the so-called high-momentum leakage flow injection between

---

[1] *The inverse evolution can be observed with static pressure distribution physically at the source of the lift.*

neighboring blade bases. As one can observe from Figure 37 on page 80 the middle of the SS surface (at s*=0.5) is much closer to the s-shaped labyrinth seal between blade bases than the PS surface (5 versus 20 [mm]) explaining the important influence of the leakage flow injection on the SS isentropic Mach distribution near the hub. As one would expect the leakage flow effects are greater for the transonic test case (Figure 39) especially for the SS where the isentropic Mach jumps from 0.8 to 1.05 at s*=0.55 and then has another hump in the supersonic region around s*=0.7. Further investigations, implicating three-dimensional unsteady flow measurements, are necessary in order to understand the complex flow involving transonic flow conditions interacting with presumably unsteady leakage flow effects in this region but they are out of the scope of the present dissertation.

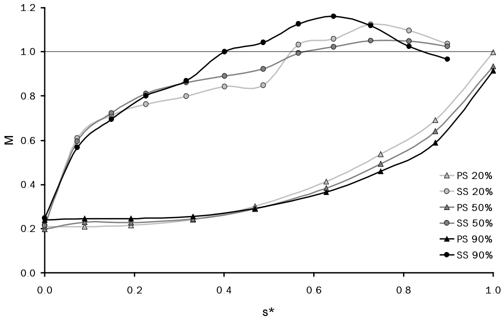

FIGURE 39. blade surface isentropic Mach distribution, transonic test case, no rotor

Other differences between the isentropic Mach distributions at the three radial positions can be accredited to geometric variations between measuring passages since the measurements are conducted on six different blades (see 2.6 p. 43). For example the combination of slight variations of stagger angles between the steady measuring blades and the high sensitivity of the LE measuring location to the proximity of the stagnation point seems to be the main source of dispersion of results at this location.

Figure 40 to Figure 45 compare the blade surface isentropic Mach distribution between the three test configurations (no rotor, EO 13, EO 22) for each radial position (25%, 50% and 90% blade height) and for both test cases. Similar trends are observable in all cases: first of all very good agreement is noticeable between the three different configurations for every radial positions and both test cases. The main differences are repetitive between plots and consist of:

- a diminishing isentropic Mach number at the LE location and on the SS near the LE as the number of inserted wake generators passes from 0 to 13 and then to 22.
- an augmenting isentropic Mach number on the SS near the TE as the number of inserted wake generators passes from 0 to 13 and then to 22.

The first observation reflects the rising losses due to the insertion of the strutted rotor in combination with augmenting engine order.

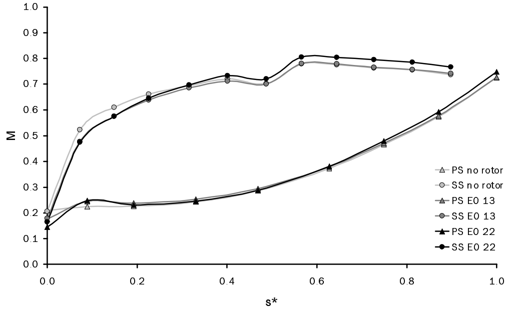

FIGURE 40. blade surface isentropic Mach, 20% blade height, subsonic test case

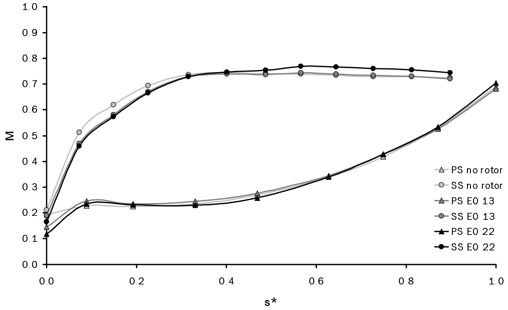

FIGURE 41. blade surface isentropic Mach, 50% blade height, subsonic test case

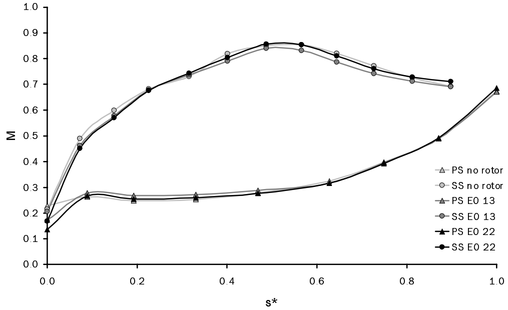

FIGURE 42. blade surface isentropic Mach, 90% blade height, subsonic test case

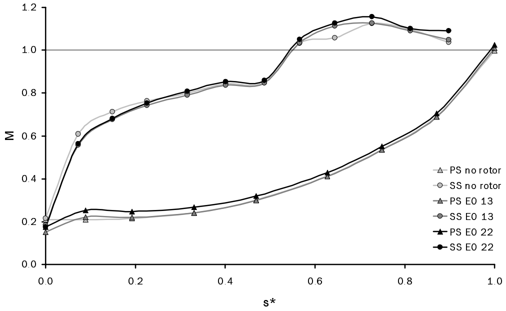

FIGURE 43. blade surface isentropic Mach, 20% blade height, transonic test case

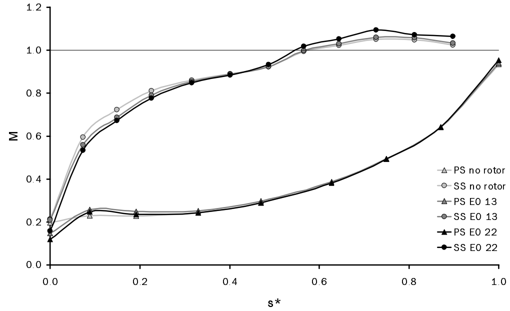

FIGURE 44. blade surface isentropic Mach, 50% blade height, transonic test case

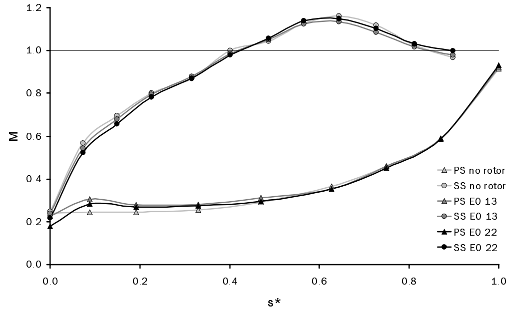

FIGURE 45. blade surface isentropic Mach, 90% blade height, transonic test case

As presented in the next section, and typical of stator-rotor interactions in turbomachinery, the effect of the wake is strong near the LE and diminishes in intensity as it progresses along the blade surface (especially on the SS). In order to counter the general velocity defect due to the presence of wakes in the steady measurements, the inlet total pressure is augmented as the number of struts passes from 0 to 13 and then 22 (see Table 7 p. 68 and Table 8 p. 69). Therefore, the differences observed reflect the compromise found between compensating the effect of a strong wake near the LE and compensating a weaker wake near the TE on the time-averaging process. In other words, the influence of the wake is under-compensated near the LE and over-compensated near the TE on the SS in order to optimize the overall blade surface isentropic Mach distribution between the three different test configurations. Considering the fact that each blade surface pressure measurement is conducted on a different instrumented blade, and that relatively small differences are observed between the blade surface isentropic Mach distributions, the overall steady loading can be considered identical between the three different test configurations and the two flow conditions to a great extend.

4.5 Executive Summary

The steady probe and blade surface measurements have shown a high level of steady flow periodicity over the blade passages and quasi-constant inflow conditions. They have also revealed the presence of secondary flow effects constituted mainly of a tip gap vortex and leakage flows through the labyrinth seals of the blade bases. The effect of each is clearly visible near the casing and near the hub, respectively, but they do not contaminate the measurements conducted in the mid-channel region, where unsteady measurements are conducted as well. In this region, the quasi-two-dimensional flow assumption is considered valid for both studied flow conditions and the effect of leakage flow can be ignored.

The steady-state results for the different test configurations exhibit very good agreement among them for both flow cases, ensuring almost identical steady flow conditions between cases where the superposition of unsteady pressures are to be studied. Small differences cannot be avoided considering the three different test configurations (no rotor EO 13, EO 22) and the presence of different gust profiles in the time-averaging process of the two engine orders. It is believed that the presented results are an optimal compromise between differences observed at the LE and at the TE, so that the overall steady loadings of the blades are quasi-identical for the three test configurations.

The transonic test case is characterized by a supersonic flow region on the second-half of the suction side of the blades and greater secondary flow effects than for the subsonic test case. It has been shown that the quasi-two-dimensional flow assumption is still valid around the mid-channel height measuring location, where the linear superposition principle of unsteady pressures has been studied.

CHAPTER 5

Time-Dependent Flow

In this chapter, the results of the time-dependent portion of this investigation are presented. These results are divided into three parts: (1) the unsteady loading induced by the torsion controlled vibration of the turbine cascade in the travelling wave mode in a uniform flow (controlled vibration measurements), (2) the forcing-function produced by upstream generated aerodynamic gusts on a clamped annular turbine cascade (gust response measurements), and, (3) the unsteady pressures produced on a vibrating cascade in the presence of upstream generated aerodynamic gusts (combined vibration-gust excitation). Parts (1) and (2) correspond to the traditional “divided” approach to the aerodynamic forced response problem. i.e.: identification of the aeroelastic properties of the cascade (aerodynamic damping and aerodynamic coupling) and identification of the aerodynamic forcing-functions. Part (3) represents an approximation of the complete phenomenon, including both the aerodynamic effects associated with the incoming flow disturbances (potential and vortical), as well as those related to the resulting elastic properties of the cascade.

The experimental results associated with the above tests are comprised primarily of time-varying pressures measured at discrete locations along the blade surface’s mid-span location. The overall objective of these measurements is to identify important aspects of the unsteady aerodynamic behavior of the blade. In particular, attention is focused on providing some needed insight into the local relationship between the time-dependent flows of parts (1) and (2) and that of part (3).

The chapter opens with a description of the various parameters used to present the time-dependent results. The remainder of the chapter is comprised of a presentation of the experimental results. This section is divided according to experiment type: controlled-vibration only, gust-response only and combined vibration-gust excitations. Finally, this chapter addresses the validity of the linear superposition principle of the unsteady pressures of (1) and (2) by comparison with the results of (3) on a quantitative and qualitative basis.

5.1 Definitions

This section describes first the time-dependent signal sign conventions used in this study. It is followed by a description of the way data are presented in this chapter and how simultaneous and combined measurements are compared to one another.

In the context of this investigation three primary types of time-dependent signals are being studied:

- blade vibration signals (20).
- strut passing signal (1).
- blade surface unsteady pressure signals (21).

Blade vibration signals are used to monitor the cascade's vibration mode for measurements involving controlled vibration of the measuring cascade. As described in section 3.6 on page 62 the imposed cascade vibration mode, called travelling wave mode, consist of an identical movement of all blades but with a constant and periodic inter-blade phase angle (IBPA) defined in Figure 46. The sign convention of the pure torsional movement studied is given in Figure 47.

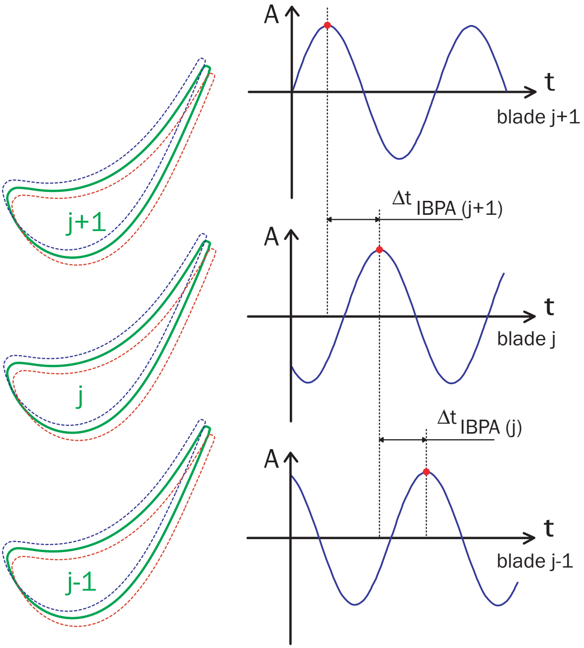

FIGURE 46. inter-blade phase angle definition for turbine cascades

For controlled vibrations only the movement of the unsteady measuring blades are used as reference signals. Therefore, in this configuration all measured blade surface unsteady pressures are expressed as a function of the time reference given by the sinusoidal movement of the blade they are on.

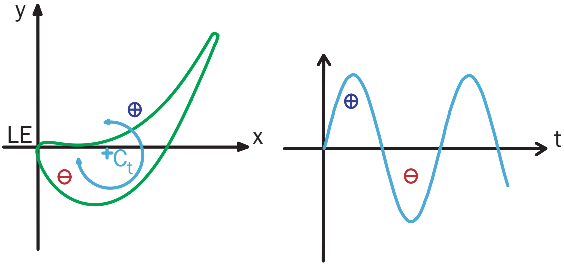

FIGURE 47. torsion sign convention

For all measurements involving rotating struts (gust response measurements, unsteady wake measurements and superposition of gust response and controlled vibration) the strut passing signal is used as reference signal and the corresponding time reference is defined in Figure 48 using a reference strut and a reference blade.

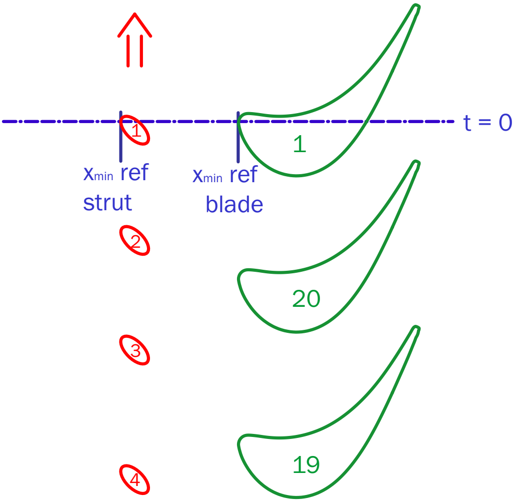

FIGURE 48. time reference with rotating wake generator

In the case of combined gust response and controlled vibration experiments the gust-vibration phase angle, Φ, is defined as the phase angle between the strut passing signal and the movement signal of the unsteady measuring blade used as reference. For a given time, this phasing between synchronized excitation sources corresponds to the relative angular positioning of the reference blade as a function of the circumferential positioning of the reference strut.

All time-dependent signals have the exact same fundamental harmonic frequency and are represented in this study as amplitudes and phases of sinusoïds. The phase angles are defined as positive when a given signal leads the reference signal, as shown in Figure 49.

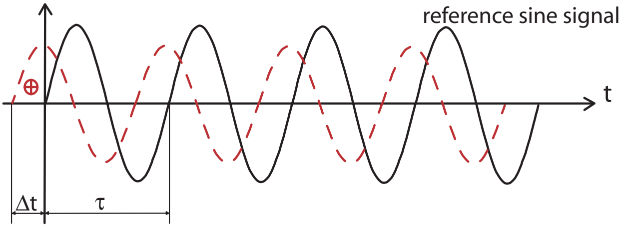

FIGURE 49. phase angle sign convention

For all three test configurations, the time-dependent signals are first analyzed individually in their dimensional form, both in the time and frequency domain, and relevant examples are given. In this context, the location of the measured unsteady pressure signals is given by the unsteady pressure transducer number as defined in Figure 10 on page 39. These numbers are preceded by LE, TE, PS or SS in order to give an indication on whether the measuring location is at the leading edge (LE), trailing edge (TE) or on the suction (SS) or pressure side (PS) of the blade. Cases are summarized and presented as time-resolved pressure contour plots as a function of time and blade surface location. The time-scale is non-dimensionalized by the first harmonic time period of the reference signal and results are presented over two periods (repeated data). The blade surface locations are presented as the non-dimensional curvilinear location s* on either the pressure side or the suction side, with values ranging from zero at the leading edge location and one at the trailing edge location. These time-resolved pressure contour plots allow a convenient qualitative comparison between the simultaneous gust-vibration measurements and the linear combination of gust response and controlled vibration measurements.

Quantitative comparisons between combined and simultaneous results are made using both local relative error spectrum contour plots and cross-correlation contour plots.

Consider two time-dependent signals S_{sim} and S_{comb}. S_{sim} is defined as a local measurement of the unsteady pressure for the simultaneous gust response and controlled vibration measurements, and S_{comb} is defined as the corresponding signal reconstructed from the separate gust response and controlled vibration results. The relative error spectrum $\varepsilon(f)$, expressed in percent, can be written as:

$$\varepsilon(f) = \frac{FFT[S_{sim} - S_{comb}]}{|S_{ref}|} \times 100 \tag{6.2}$$

where $|S_{ref}|$ is the maximum amplitude variation of either signal used as reference.

The corresponding relative error spectrum plots show the location and the concerned frequencies where discrepancies occur between simultaneous and combined measurements. But effects of time lag between simultaneous and combined signals cannot be clearly identified with this technique. On the contrary, the cross-correlation between these two signals in the time-domain gives an indication of the quality of the signal's time correspondence as a function of the time-lag k introduced as a new variable. The cross-correlation can be non-dimensionalized using a reference signal auto-correlation as presented in the following equation:

$$r(k) = \frac{R[S_{sim};S_{comb}]}{R[S_{ref};S_{ref}]} \tag{6.3}$$

where the cross-correlation R between an x and a y time signal is defined analytically as:

$$R_{xy}(t) = x(t) \otimes y(t) = \int_{-\infty}^{\infty} (x(\tau) \cdot y(t+\tau))d\tau \tag{6.4}$$

For discretized signals X and Y with m and n elements, respectively, using k, the discrete time-lag, equation (6.4) becomes:

$$R_{XY}(k) = \sum_{i=0}^{m-1} X_j Y_{j+k} \quad \text{for k= -(m-1),-(m-2)... n-1} \tag{6.5}$$

Finding the cross-correlation peak gives the optimal values of k and r(k) yielding both an indication of the quality of the signals time-correspondence and the associated time-lag. Non-dimensionalizing the cross-correlation using the maximum auto-correlation value between the simultaneously measured and combined signals yields a range of non-dimensional cross-correlation r(k) between zero and one. This latter value is associated with identical phases between each signal's fundamental harmonic components to be compared.

5.2 Time-Dependent Measurements Summary

This section gives an overview of all the time-dependent measurements performed in this study and the corresponding unsteady flow parameters. The reader is referred to section 4.2 on page 67 for a description of the average flow conditions associated with the following unsteady flow conditions.

The unsteady flow parameters for controlled-vibration only experiments are summarized in Table 10. The twenty different inter-blade phase angles selected correspond to the traveling wave vibration mode of the measuring cascade as further described in section 3.6 on page 62.

Table 11 and Table 12 summarizes, the unsteady specifications for the gust-response only measurements, and the simultaneous controlled vibration and gust response measurements, respectively. The reader is referred to section 3.3 on page 51 for a detailed description of the measuring technique associated with these types of measurements.

test case	vibration frequency f [Hz]	vibration amplitude A [°]	reduced frequency k []	inter-blade phase angles IBPA [°]
subsonic	265	0.313	0.281	18, 36, 54, 72, 90, 108, 126, 144, 162, 180, 198, 216, 234, 252, 270, 288, 306, 324, 342
transonic	265	0.313	0.205	18, 36, 54, 72, 90, 108, 126, 144, 162, 180, 198, 216, 234, 252, 270, 288, 306, 324, 342

TABLE 10. controlled vibration measurement specifications

test case	excitation frequency f [Hz]	reduced frequency k []	engine order EO []
subsonic	265	0.281	13
subsonic	265	0.281	22
transonic	265	0.205	13
transonic	265	0.205	22

TABLE 11. gust response measurement specifications

For the simultaneous controlled vibration and gust response measurements around twenty gust-vibration phase angle Φ values were selected between 0 and 360 [°]. Considering all the different parameters associated with this test configuration, the cases described in Table 12 correspond to 252 different measurements of the blade surface unsteady pressure distribution.

test case	excitation frequency f [Hz]	vibration amplitude A [°]	reduced frequency k []	engine order EO []	IBPA [°]	gust-vibration phase angle Φ [°]
subsonic	265	0.313	0.281	13	0, 90, 180, 270	~20 values
subsonic	265	0.313	0.281	22	0, 90, 180, 270	~20 values
transonic	265	0.313	0.205	13	0, 90, 180, 270	~20 values
transonic	265	0.313	0.205	22	0, 90, 180, 270	~20 values

TABLE 12. simultaneous gust response and controlled vibration measurements specifications

5.3 Controlled Vibration Measurements

This section gives relevant examples of the blade surface unsteady pressure signals acquired during controlled-vibration only measurements. This data is usually the basis for studying the aerodynamic stability of the cascade with the examination of the local and global aerodynamic damping as a function of the IBPA, i.e: the aerodynamic damping and aerodynamic coupling effects of the cascade. Since the primary focus of the present dissertation is the validity of the linear superposition principle of the controlled vibration and gust response induced time-dependent pressures, the aerodynamic stability analysis is summarized in APPENDIX B. In this current section the nature of the blade surface time-dependent pressures is described, analyzed and illustrated in the frequency domain as well as in the time domain.

Examples of typical amplitude spectra of the unsteady pressure perturbations produced by controlled vibration measurements with 0 [°] IBPA for the subsonic test case and the transonic test case are given in Figure 50 and Figure 51, respectively. Each scale is adapted to the maximum amplitude of the presented signal for greater visibility. Only six relevant signals out of the twenty-one acquired signals are presented (LE, 2 PS, 2 SS, TE). Figure 10 on page 39 shows the actual measurement locations on the blade surface corresponding to the unsteady pressure transducer number given in the following figures. The scaling is adapted to each signal's maximum amplitude for visibility reasons. These typical signals have an excellent signal-to-noise ratio with a single harmonic component at the vibration frequency of 265 [Hz]. A second peak at 1.1 [kHz] has been observed on practically all unsteady pressure signals and for all measurements conducted in the non-rotating annular test facility. This pressure perturbation fades out from LE to TE and is attributed to an excitation source upstream of the measuring cascade. It is believed that the inflow splitter disk (between inner and outer settling chambers shown in Figure 6 on page 34) vibrates and produces this pressure disturbance.

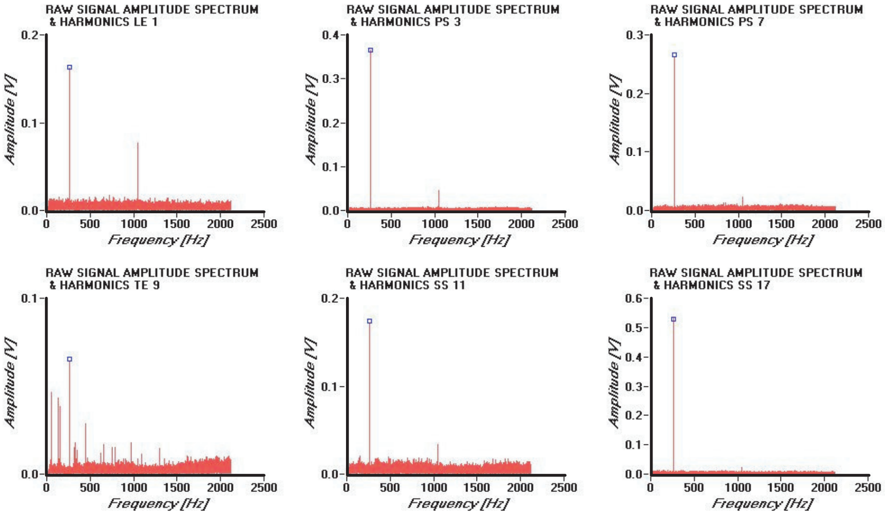

FIGURE 50. raw amplitude spectrum example for controlled vibration measurements, subsonic test case, torsion, IBPA 0 [°], 0.313 [°] vibration amplitude

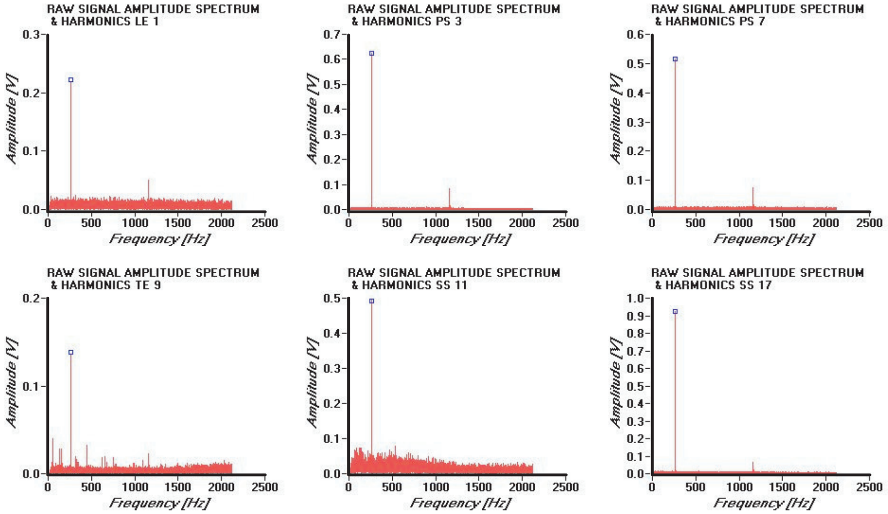

FIGURE 51. raw amplitude spectrum example for controlled vibration measurements, transonic test case, torsion, IBPA 0 [°], 0.313 [°] vibration amplitude

Besides the two main peaks due to the effect of the cascade’s vibration mode and the undesired upstream pressure disturbance, the raw signal amplitude spectra exhibit quasi-constant low level noise over the measured bandwidth. This white-noise is mainly attributed to freestream turbulence and roughly doubles in amplitude for the transonic measurements. One exception to this rule is the presence of secondary low-level peaks in the noise of the trailing edge signals. At this location the effects of the complex unsteady flow, mainly due to viscosity, separation and induced vortex generation, can be observed.

The harmonic signal analysis described in section 3.3 on page 51 is represented in Figure 50 and Figure 51 by square symbols on the fundamental harmonic corresponding to the cascade’s excitation frequency. The sharpness of the peaks show that there is no spectral leakage effects at all and, therefore, that the peak detection process can be accurately performed, both on amplitude and phase.

In summary, the unsteady pressure disturbance generated by the controlled vibration of the cascade in the travelling wave mode are single sine tones that are precisely detected in the data reduction process.

On all the unsteady pressure signals acquired for controlled vibration measurements (840), only three of them did not have a detectable fundamental harmonic. These cases presented in Figure 52 all come from transonic measurements inside the transonic pocket situate on the suction side surface of the blade near the trailing edge. The complex unsteady flow pattern due to an oscillating shock and/or shock-boundary layer interactions may be at the origin of the effects observed. The limited amount of occurrence of these phenomena is attributed to their high sensitivity to slight variations of main steady flow conditions and/or changes in the vibration mode (IBPA) on a discrete measuring location.

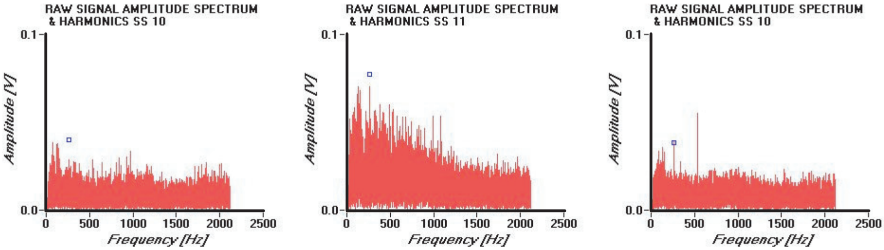

FIGURE 52. example of shock effect on raw amplitude spectrum for controlled vibration measurements, transonic test case, torsion, IBPA 90, 180, 324 [°]

Following the data reduction process, the time-dependent pressure signals produced by the cascade’s vibration mode can be represented in the time-domain as time-resolved pressure contour plots as illustrated in Figure 53 to Figure 55. These measurements are all presented over two periods (repeated data) for visibility reasons.

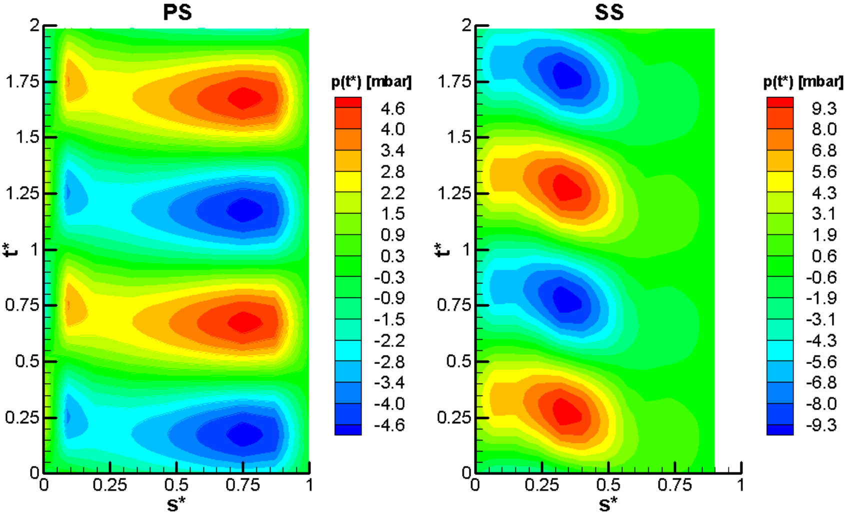

FIGURE 53. time-resolved pressures, controlled vibration measurements, subsonic test case, 265 [Hz], 0.313 [°] vibration amplitude, 180 [°] IBPA

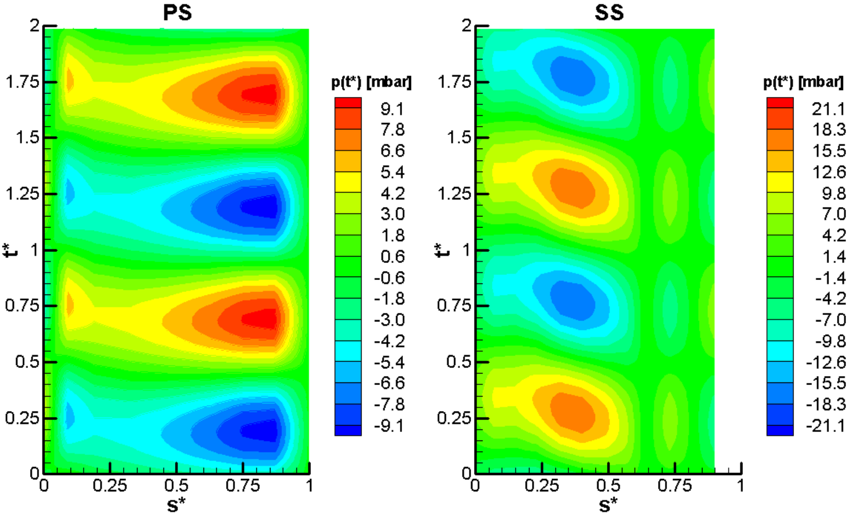

FIGURE 54. time-resolved pressures, controlled vibration measurements, transonic test case, 265 [Hz], 0.313 [°] vibration amplitude, 180 [°] IBPA

In the first two examples comparing results with the same cascade vibration mode but with two different flow conditions, one can observe the important effect of the outlet Mach number variation on the blade surface unsteady pressure amplitudes (different scaling).

The main effect of the outlet Mach number augmentation is the general rise of the unsteady pressure amplitudes by a factor of two in this example. Of course, the impact of the cascade's vibration mode is also important on the time-dependent pressure distribution as illustrated with the comparison between Figure 53 and Figure 55. For example, on the pressure side of the blade, the maximum pressure variation occurs near the trailing edge for an inter-blade phase angle of 180 [°] but near the leading edge for an inter-blade phase angle of 0 [°].

For a more detailed description of the effects of the cascade's vibration mode and flow conditions on the unsteady blade surface pressure distribution and its physical implications, the reader is referred to the aerodynamic stability analysis presented in APPENDIX B on page 151.

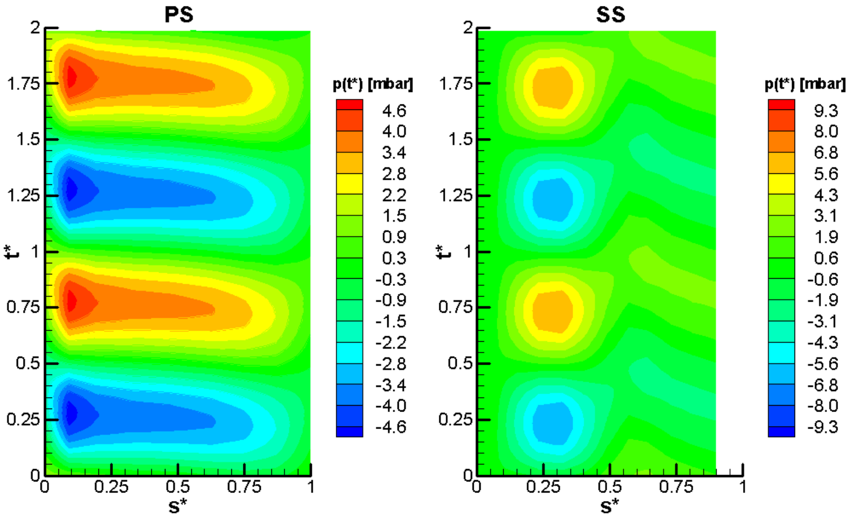

FIGURE 55. time-resolved pressures, controlled vibration measurements, subsonic test case, 265 [Hz], 0.313 [°] vibration amplitude, 0 [°] IBPA

5.4 Gust Response Measurements

This section presents all the gust response measurements summarized in Table 11 on page 92 as time-resolved contour plots. The nature of the blade surface time-dependent pressures is first described and analyzed using relevant examples, both in the frequency and time domains. Additional information on the nature of the wake, for the subsonic test case and an engine order of 22, has been obtained using Oxford's unsteady wedge probe (see section 2.7 on page 44) and is presented in APPENDIX C on page 157.

Examples of typical amplitude spectra of the unsteady pressure perturbations produced by gust response measurements are given for an engine order of 13 and 22 in Figure 56 and Figure 57, respectively. Only six relevant signals out of the twenty-one acquired signals are presented (LE, 2 PS, 2 SS, TE). Figure 10 on page 39 shows the actual measurement locations on the blade surface corresponding to the unsteady pressure transducer number given in the following figures. Each scale is adapted to the maximum amplitude of the presented signal for greater visibility.

These typical signals exhibit an excellent signal-to-noise ratio, even at the trailing edge location. In opposition to the controlled vibration time-dependent pressure signals with just a single harmonic component at 265 [Hz], the frequency content of gust response signals is much larger. With the same fundamental harmonic frequency, gust response signals have a maximum of up to four significant harmonics with an engine order of 22 (Figure 56) and six for an engine order of 13 (Figure 57). This difference observed in the frequency content is due to the variation of rotating struts speed in order to get a common wake passing frequency. This implies that the relative velocity of the struts is augmented by 69% between EO 22 and EO 13. The effect on the wake in the time-domain is a higher velocity defect and a narrower wake thickness for the EO 13 measurements. Its effect on the time-dependent pressure can be partially observed at the LE location in Figure 58 and Figure 59. Besides these major differences, vortical and potential disturbances must rise with increasing relative strut velocity but only the potential effect can be observed with the present measurements. For both engine orders, the wake-induced unsteady pressure amplitude fades out rapidly from LE to TE on both surfaces. This is an indication that the wake as important potential effects since vortical gusts decay slowly in a linear manner opposed to potential gusts that decay exponentially with increasing axial distance.

The SS is less affected by the gust than the PS as this latter surface faces the gust and shades the SS. The evolution of the wake-induced time-dependent pressure along the blade surface differs between EO 13 and 22. For the first case the shape of the wake is similar from LE to TE but for EO 22 it evolves rapidly to a more sinus-shaped pressure disturbance. This, of course, is also reflected in the frequency-domain by a more rapid vanishing of higher harmonics for EO 22. The effect of the transonic pocket on the suction surface near the TE is illustrated with the unsteady pressure signal at location SS 11. In Figure 56 and Figure 57, the harmonic content at this location is limited to two significant harmonics and closely resembles the TE signals but with higher amplitudes. The differences in the nature of the pressure signals at these two locations compared to the other locations, in the subsonic flow region, is more visible in the time domain plots of Figure 58 and Figure 59.

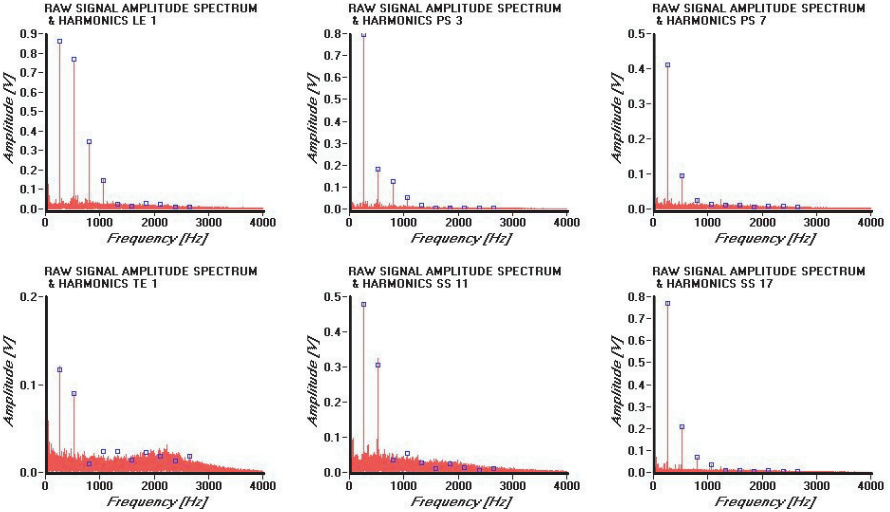

FIGURE 56. raw amplitude spectrum examples for gust response measurements, EO 22, transonic test case, 265 [Hz] excitation frequency

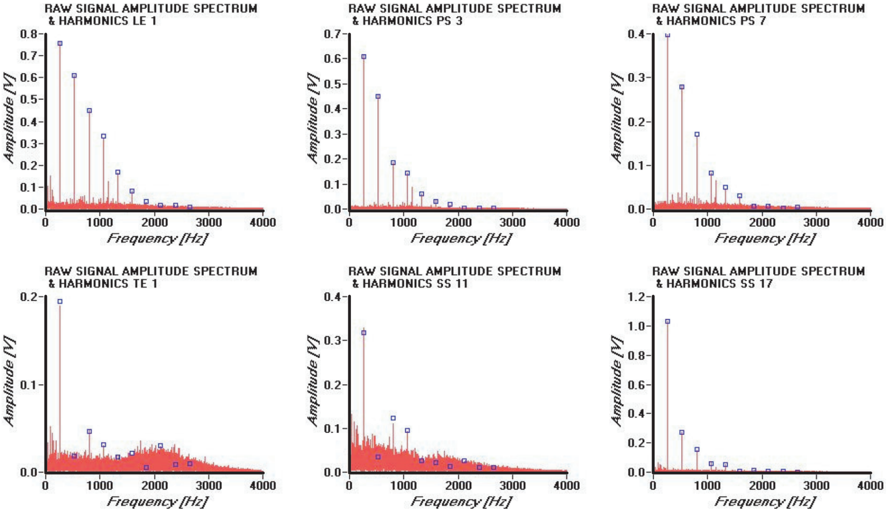

FIGURE 57. raw amplitude spectrum examples for gust response measurements, EO 13, transonic test case, 265 [Hz] excitation frequency

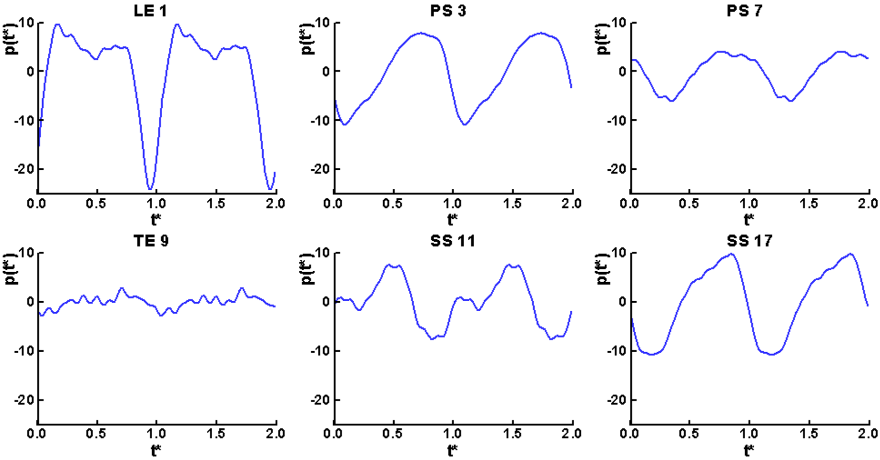

FIGURE 58. time-dependent pressure examples for gust response measurements, EO 22, transonic test case, 265 [Hz] excitation frequency

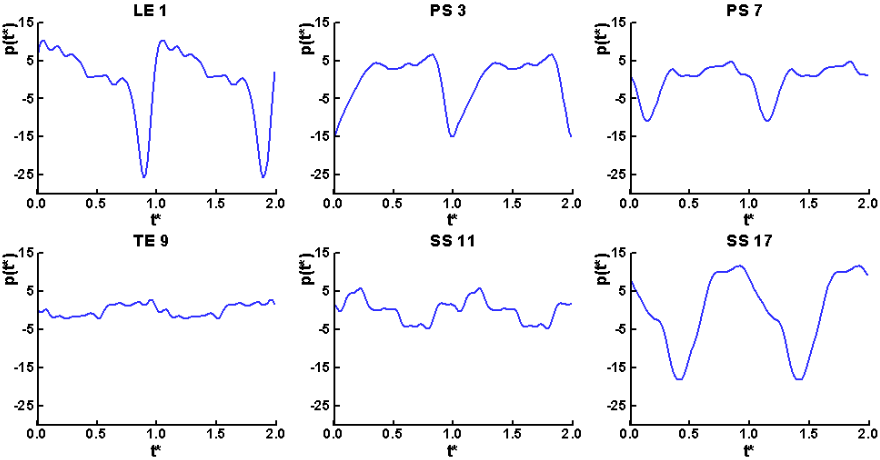

FIGURE 59. time-dependent pressure examples for gust response measurements, EO 13, transonic test case, 265 [Hz] excitation frequency

Figure 60 to Figure 63 present all the gust response measurements as time-resolved pressure contour plots on the PS and SS. Blue regions indicate the pressure defect induced by the wake. It has a maximum pressure drop at the LE for all four cases and then travels to the TE with diminishing amplitude. The slopes of the blue regions are a reflection of the speed at which the pressure disturbance propagates from LE to TE. For example, in Figure 62, this disturbance takes a quarter of a period to travel from LE to TE on the pressure side but takes about twice the time on the suction side. Of course this is due to the higher flow acceleration over the suction side at the origin of lift.

The SS results of EO 22 don’t actually exhibit a smooth shedding of the pressure disturbance along the blade surface. It actually seems that the pressure perturbations travel from TE to LE as opposed to PS results or SS results for an EO of 13. This is particularly visible for the transonic test case.

Generally, a convected wake will create two types of instantaneous pressure waves on an airfoil. Usually, negative pressure disturbances are present in front of the wake, where the flow is accelerated, and positive ones follow behind the wake, where the flow is decelerated. These instantaneous disturbances will then each travel upstream and downstream at velocities that are different from the convection velocity. Therefore, different superposition effects of these “elemental waves” can be observed at each surface position. Between measurements with an engine order of 13 and 22, the spatial separation of the wakes is changed, while the temporal separation remains the same (same frequency). Consequently, different superposition patterns can be observed. It seems possible that this could result in an overall impression of a downstream running pressure wave in one case and an upstream running one in the other. To further investigate these effects, additional data on the main flow (simulations or laser measurements) would be necessary.

The comparison between subsonic and transonic results with the same engine order shows that, besides a small augmentation of the unsteady pressure levels, the contour plots look very similar. The only significant differences can be seen on the suction side near the TE, where the transonic flow region appears. Again, this shows the important influence of a transonic flow region on the wake-induced blade surface time-dependent pressure.

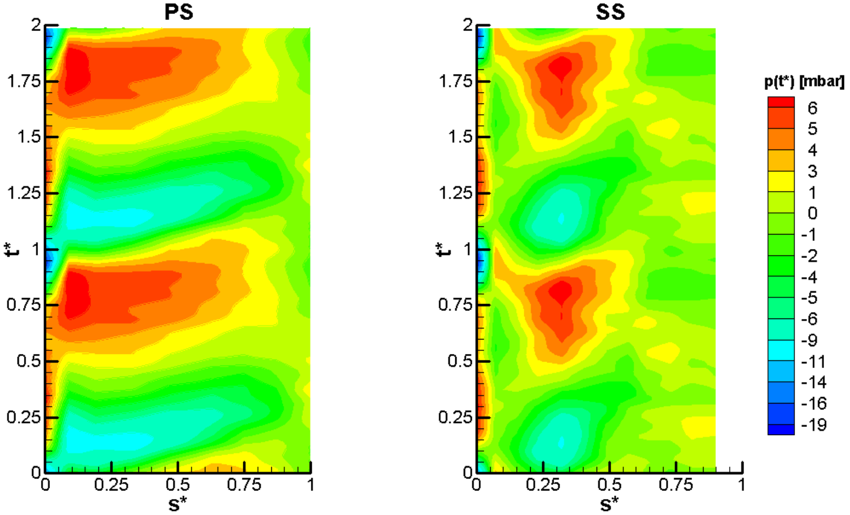

FIGURE 60. Time-resolved pressures, gust response measurements, subsonic test case, EO 22, 265 [Hz] excitation frequency

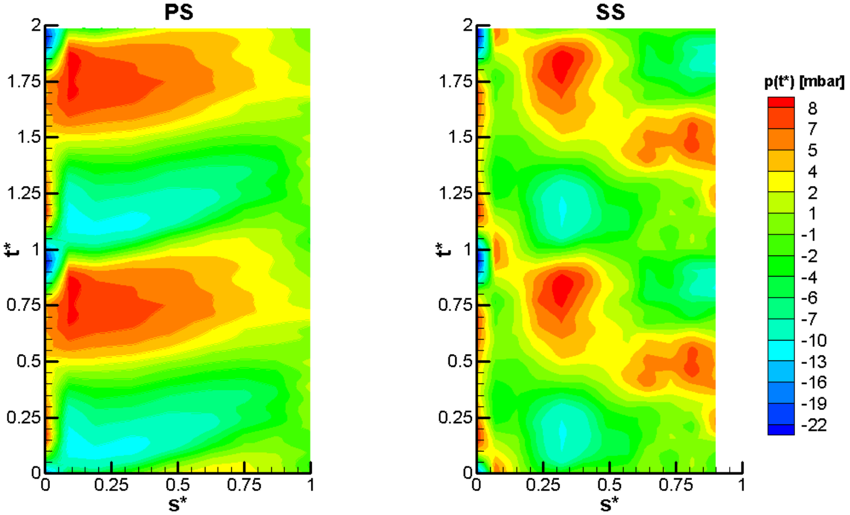

FIGURE 61. Time-resolved pressures, gust response measurements, transonic test case, EO 22, 265 [Hz] excitation frequency

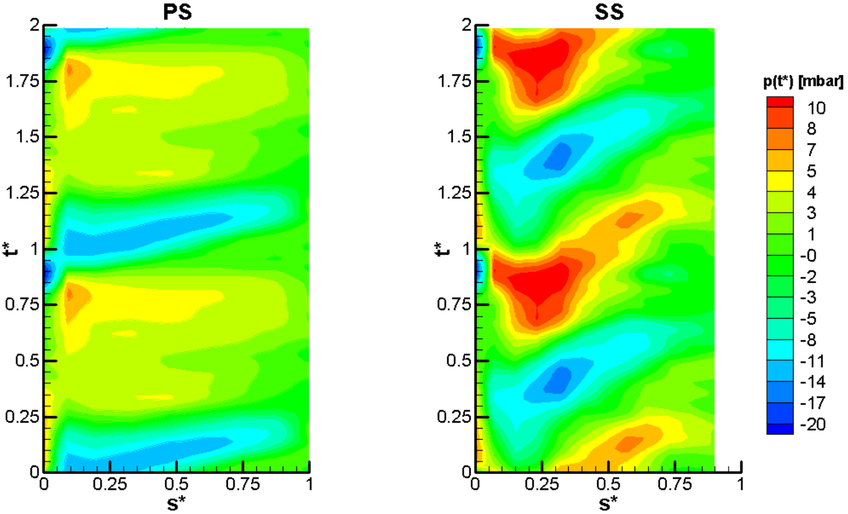

FIGURE 62. Time-resolved pressures, gust response measurements, subsonic test case, EO 13, 265 [Hz] excitation frequency

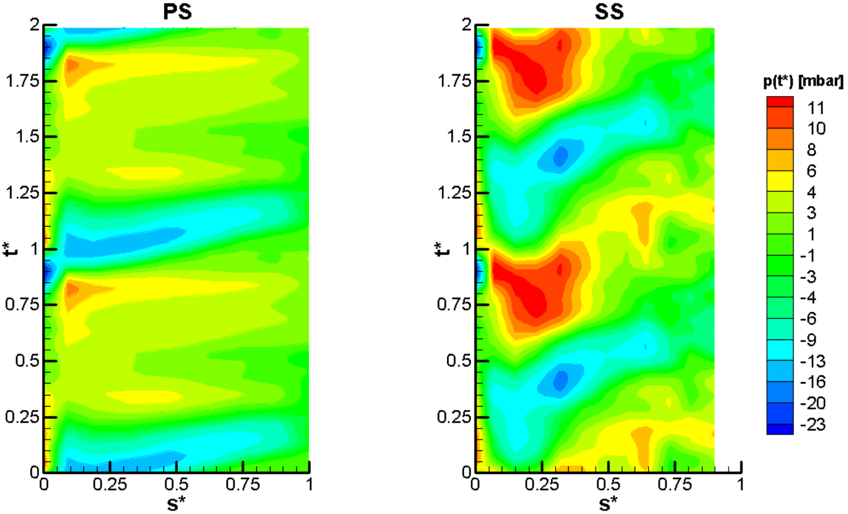

FIGURE 63. Time-resolved pressures, gust response measurements, transonic test case, EO 13, 265 [Hz] excitation frequency

5.5 Simultaneous Gust Response and Controlled Vibration Measurements

In this section, two relevant examples of simultaneous gust response and controlled vibration measurements are presented out of the 252 measurements carried out and summarized in Table 12 on page 93. These two simultaneous measurement cases correspond to the combination of controlled-vibration only measurements and gust-response only measurements presented as examples in the two previous sections. The reader is referred to the following section for a comparison between simultaneous and combined gust-vibration excitation results. The nature of the blade surface time-dependent pressures is first described and analyzed, both in the frequency and time-domains.

In Figure 64 and Figure 65, examples of typical amplitude spectra of the unsteady pressure perturbations produced by simultaneous gust response and controlled vibration measurements are given. Only six relevant signals out of the twenty-one acquired signals are presented (LE, 2 PS, 2 SS, TE). Figure 66 and Figure 67 present the harmonic signals detected in Figure 64 and Figure 65, respectively but in the time-domain. Each scale is adapted to the maximum amplitude of the presented signal for greater visibility.

The full results for these two examples are given in Figure 68 and Figure 69 on page 109, respectively as time-resolved pressure contour plots. Figure 10 on page 39 shows the actual measurement locations on the blade surface corresponding to the unsteady pressure transducer number given in the following figures.

The first simultaneous case presented (Figure 64, Figure 66 and Figure 68) corresponds to the superposition of the controlled-vibration only measurements of Figure 53 on page 97 and the gust-response only measurements of Figure 62 on page 104 with a gust-vibration phase angle Φ of 0.7[°]. The second simultaneous case presented hereafter (Figure 65, Figure 67 and Figure 69) corresponds to the superposition of the controlled-vibration only measurements of Figure 54 on page 97 and the gust-response only measurements of Figure 61 on page 103 with a gust-vibration phase angle Φ of 358.4[°]. In both cases the gust-vibration phase angle has been chosen so that the reader can easily imagine a superposition of the presented controlled vibration and gust response results. In order to view the important effect of the gust-vibration phasing, Figure 70 and Figure 71 show the same test conditions but with a Φ of 161.7 and 175.3 [°], respectively.

The raw amplitude spectra examples of Figure 64 and Figure 65 look similar to gust-response only measurements (Figure 56 and Figure 57 on page 100), as one would expect from the contribution of a single main harmonic present in the controlled vibration pressure signals (with the same order of magnitude). Besides differences in amplitude levels of the different harmonics, the same observations are valid. Simultaneous GR & CV signals have a maximum of up to four significant harmonics with an engine order of 22 (Figure 65) and six for an engine order of 13 (Figure 64). These typical signals exhibit an excellent signal-to-noise ratio, allowing a precise detection of all the significant harmonics of the pressure disturbances as illustrated by the square symbols in the following figures.

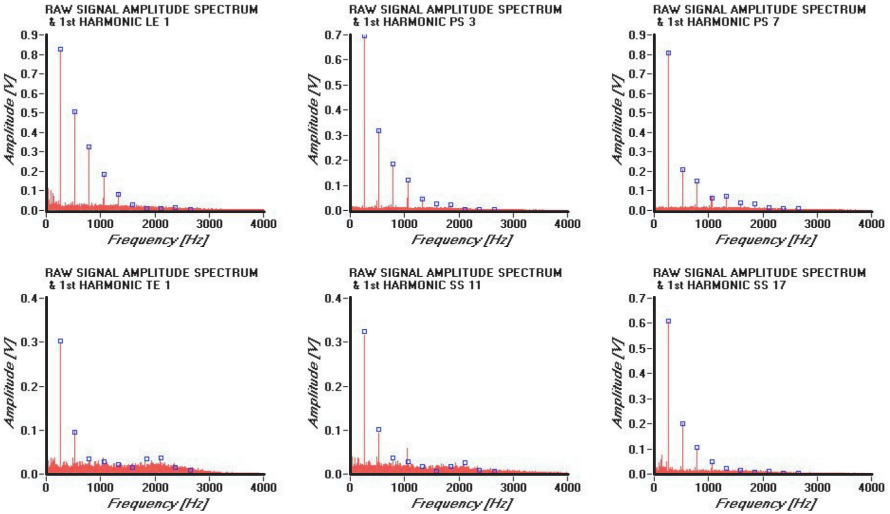

FIGURE 64. raw amplitude spectrum examples, simultaneous GR & CV measurements, subsonic test case, EO 13, f=265 [Hz], A=0.316 [°], IBPA=180 [°], Φ=0.7[°]

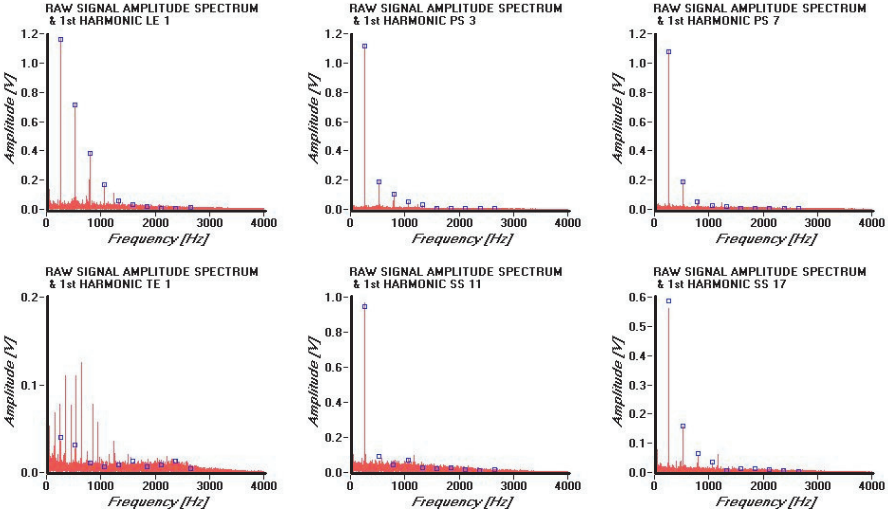

FIGURE 65. raw amplitude spectrum examples, simultaneous GR & CV measurements, transonic test case, EO 22, f=265[Hz], A=0.316[°], IBPA=180[°], Φ=358[°]

At first glance, the time-dependent pressure examples, given in Figure 66 and Figure 67, resemble the gust-response only results on page 101. But a more detailed comparison shows that, besides similarities in the overall shape of the time signals, the effect of the cascade's vibration is clearly present. For example, comparing Figure 67 with Figure 58 on page 101 shows that, in this case, the cascade's vibration mode augments the PS time-dependent pressure amplitudes with a gust-vibration phasing approaching zero. PS 3 signal gains about 30% on amplitude and PS 7 triples for the simultaneous case. These differences become evident when looking at the time-resolved pressure contour plots. For example, comparing Figure 68 with Figure 62 on page 104 shows considerable differences in the localization of the maxima and minima. In this case PS and SS maxima are displaced towards the TE of the blade. Considering the controlled vibration results for this case (Figure 53 on page 97), one can see that, with a gust-vibration phase angle around zero degrees, the PS time-dependent pressures from controlled vibration and gust response results are generally in phase. So, for instance, the maxima found in the controlled vibration PS plot near the TE dominates in the simultaneous results. But, on the contrary, SS data shows that near the LE the time-dependent pressure signals have a phase shift between controlled vibration and gust response of around 180 [°], such that the maxima disappear in the simultaneous results. On the SS surface near the TE, the pressure disturbance from the controlled vibration is negligible for this vibration mode and, therefore, the more important pressure fluctuations found in the gust response results, and at this location, dominates in the simultaneous measurements. Changing the gust-vibration phase by 180 [°] will inverse these effects, as one can observe in Figure 70. In this case the PS time-dependent pressures are globally damped by a factor of two. On the SS surface, the maxima regions are more extended and closer to the LE, since this time the pressure disturbances from controlled vibration and gust response are in phase in this region and have a constructive interaction. Similar effects can be observed with the other example presented in Figure 69 and Figure 71. With the same controlled vibration conditions as the previous example, this time the flow conditions are transonic and the engine order is 22. For a gust-vibration phasing near zero, there is a globally constructive interaction between controlled vibration and gust response pressure disturbances on the PS of the blade, but a destructive interaction on the SS of the blade. For a gust-vibration phase angle near 180 [°], the inverse effects can be observed, especially for the SS of the blade where the maxima are particularly high.

Generally, this suggests that the gust-vibration phase angle has an important effect on the time-dependent pressure distribution and, therefore, on the excitation levels and excited modes. In other words, it is likely that the judicious choice of a gust-vibration phase angle can diminish the aerodynamic excitation levels for a given cascade vibration mode, flow condition and test configuration of a single stage.

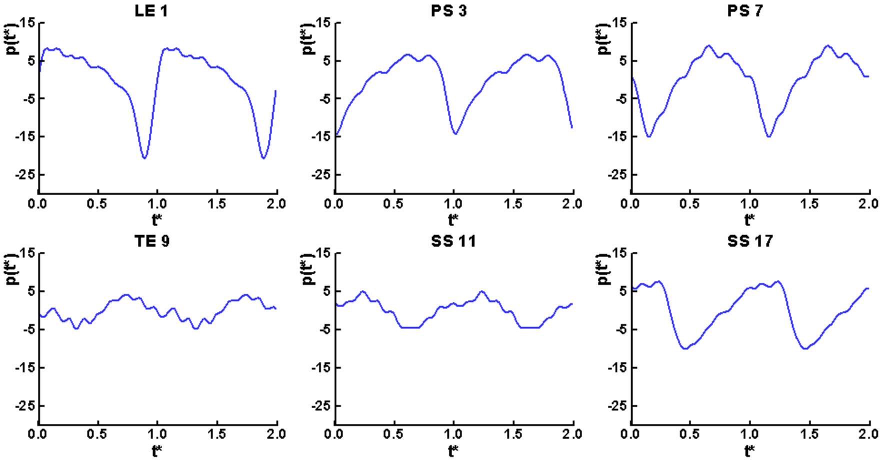

FIGURE 66. time-dependent pressure examples, simultaneous GR & CV measurements, subsonic test case, EO 13, f=265 [Hz], A=0.316 [°], IBPA=180 [°], Φ=0.7[°]

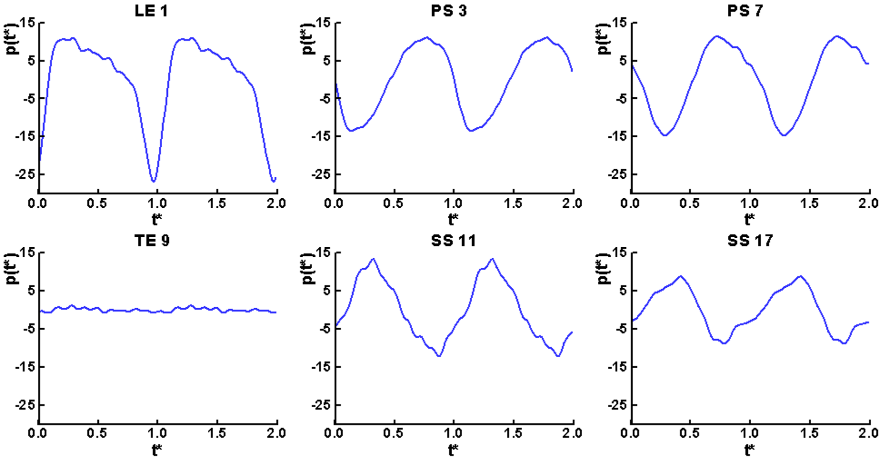

FIGURE 67. time-dependent pressure examples, simultaneous GR & CV measurements, transonic test case, EO 22, f=265[Hz], A=0.316[°], IBPA=180[°], Φ=358[°]

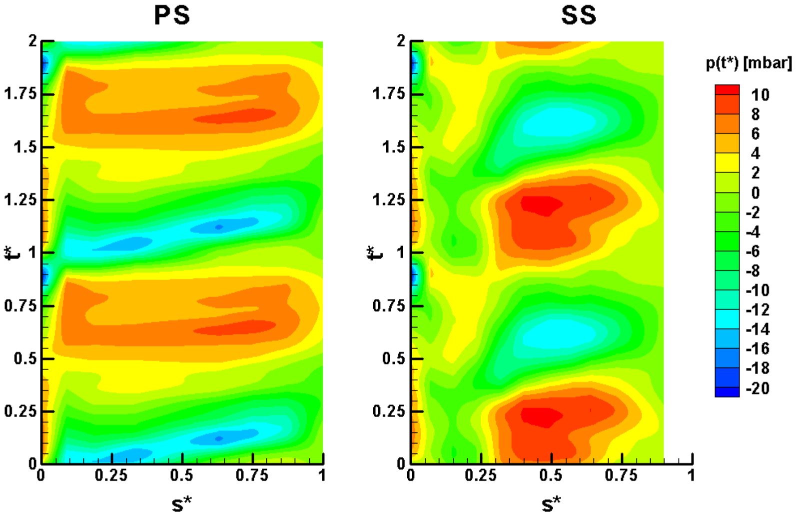

FIGURE 68. time-resolved pressures, simultaneous GR & CV measurements, subsonic test case, EO 13, f=265 [Hz], A=0.316 [°], IBPA = 180 [°], Φ = 0.7 [°]

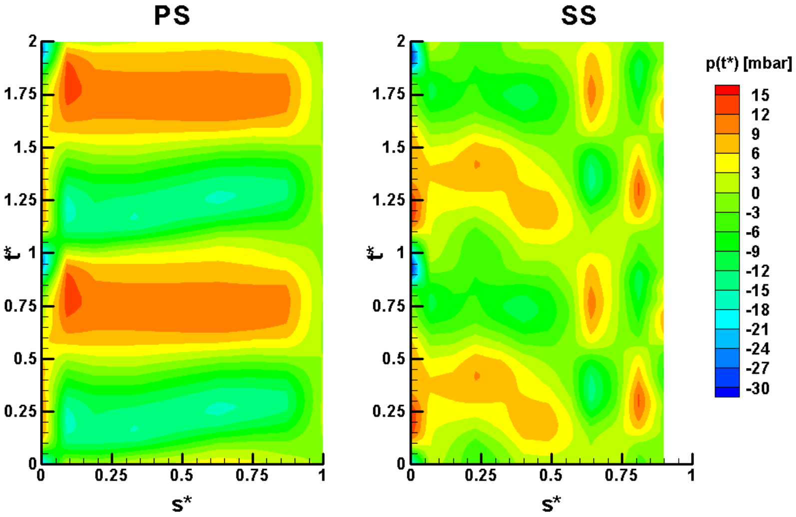

FIGURE 69. time-resolved pressures, simultaneous GR & CV measurements, transonic test case, EO 22, f=265 [Hz], A=0.316 [°], IBPA = 180 [°], Φ = 358.3 [°]

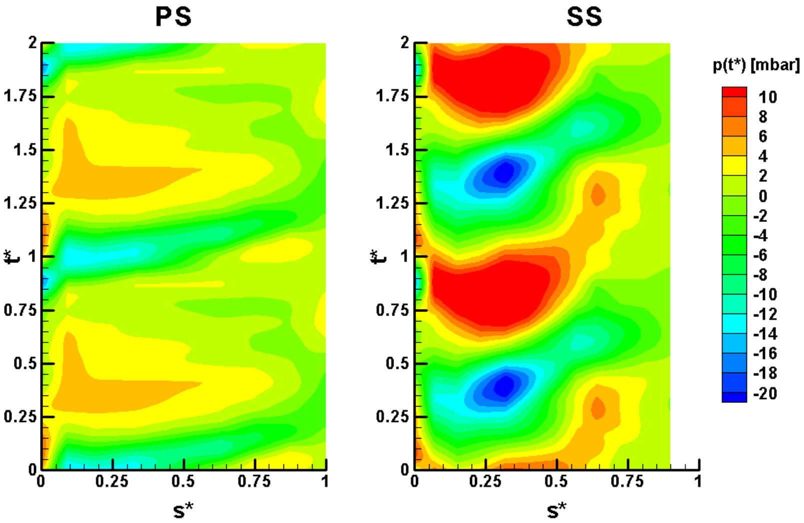

FIGURE 70. time-resolved pressures, simultaneous GR & CV measurements, subsonic test case, EO 13, f=265 [Hz], A=0.316 [°], IBPA = 180 [°], Φ = 161.7 [°]

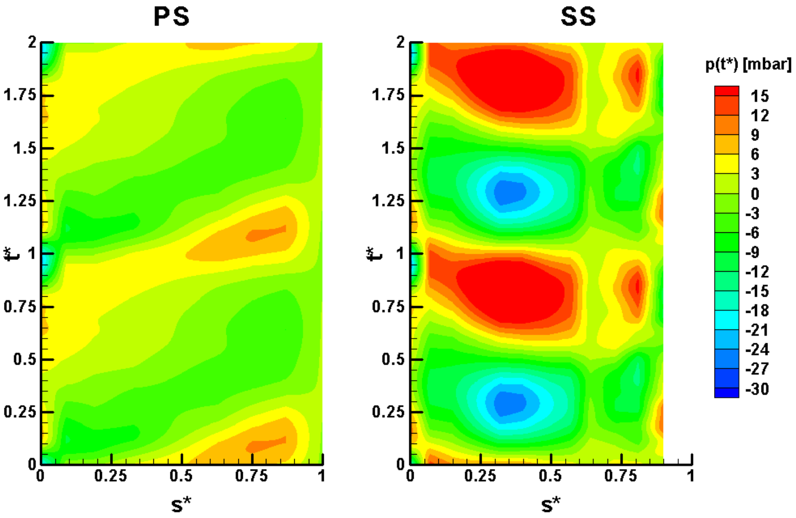

FIGURE 71. time-resolved pressures, simultaneous GR & CV measurements, transonic test case, EO 22, f=265 [Hz], A=0.316 [°], IBPA = 180 [°], Φ = 175.3 [°]

5.6 Evaluation of the Linear Superposition Principle

This important section addresses the validity of the linear superposition principle of the blade surface time-dependent pressure distribution due to upstream passing wakes and due to the cascade's vibration mode. In other words, that the local forcing-function due to upstream generated wakes can be linearly combined with the aeroelastic characteristics of the cascade (aerodynamic damping and aerodynamic coupling effects).

This section starts with a qualitative comparison between the simultaneous controlled vibration and gust response examples presented in the previous section with the corresponding linear combination of controlled-vibration only results (section 5.3 on page 94) and gust-response only measurements (section 5.4 on page 99). It is followed by the analysis of the difference between the simultaneous and combined cases using both local error spectrum plots and local cross-correlation plots as defined in section 5.1. Finally, a statistical analysis is used to isolate the effects of the different variables on the validity of this linear superposition principle of unsteady pressure.

Figure 72 to Figure 75 present the combined results from separated controlled vibration and gust response results corresponding to the simultaneous measurements shown in Figure 68 to Figure 71 (p. 109 and p. 110), respectively. The combined cases correspond to adding the controlled-vibration only pressure disturbances, delayed with the gust vibration phase angle Φ, to the gust-response only time-dependent pressure signals. The time reference is therefore the same as for gust response measurements, whose definition is given in Figure 48 on page 89. At first glance, all four examples compare well between simultaneous and combined results. The overall patterns, as well as the peak's locations and amplitudes closely match between simultaneous and reconstructed results. One exception to this rule is the presence of important discrepancies in the transonic region of the blade (SS, $0.6<s^*<0.9$, Figure 69 and Figure 73; Figure 71 and Figure 75). In this region, dominated by non-linear aerodynamic effects, important variations can be observed, particularly on the phase of the pressure perturbations that are swapped by almost 180 [°]. Looking more closely at $s^*=0.9$ shows that, at this location (SS 10), the comparison is valid again with no more phase shift effects. This is most likely due to the variation of the shock's mean position between gust-response only and controlled-vibration only measurements. In addition, both shocks can oscillate over several captors considering their important unsteady behavior. It is most probable that mainly the displacement of the shocks between individual cases has an effect on the validity of the superposition principle and that it is still valid in the supersonic flow region. This feature is further analyzed in the following pages. Beside discrepancies in the shock region, slight differences can be observed on the local amplitudes in regions where the time-dependent pressure variations are small. For example, for the subsonic test case with an engine order of 13 presented in Figure 70 and Figure 74, the SS data compare better than the PS data, which have smaller overall amplitude variations. This is believed to be due to the lower precision of the data acquisition as further described in the quantitative evaluation.

As illustrated by these time-resolved contour plots, and confirmed by the other results gathered for the current study, the linear superposition of unsteady pressures due to upstream passing wakes and due to the cascade's vibration mode is qualitatively representative of simultaneous measurements, except in the transonic region where important discrepancies appear, particularly near the shock's location, as indicated by important phase shifts.

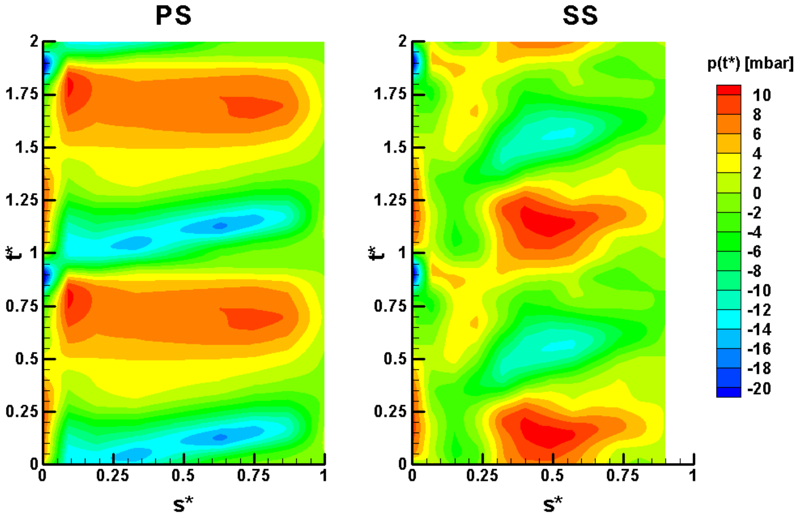

FIGURE 72. time-resolved pressures, combined GR + CV measurements, subsonic test case, EO 13, f=265 [Hz], A=0.316 [°], IBPA = 180 [°], Φ = 0.7 [°]

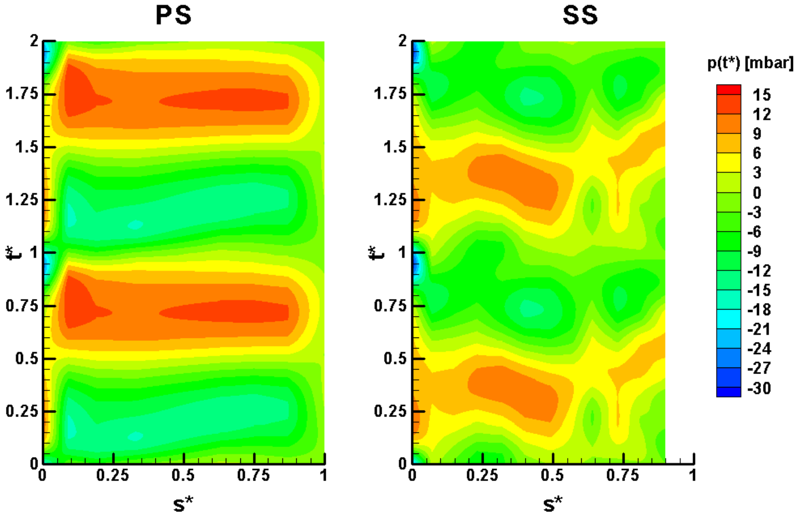

FIGURE 73. time-resolved pressures, combined GR + CV measurements, transonic test case, EO 22, f=265 [Hz], A=0.316 [°], IBPA = 180 [°], Φ = 358.3 [°]

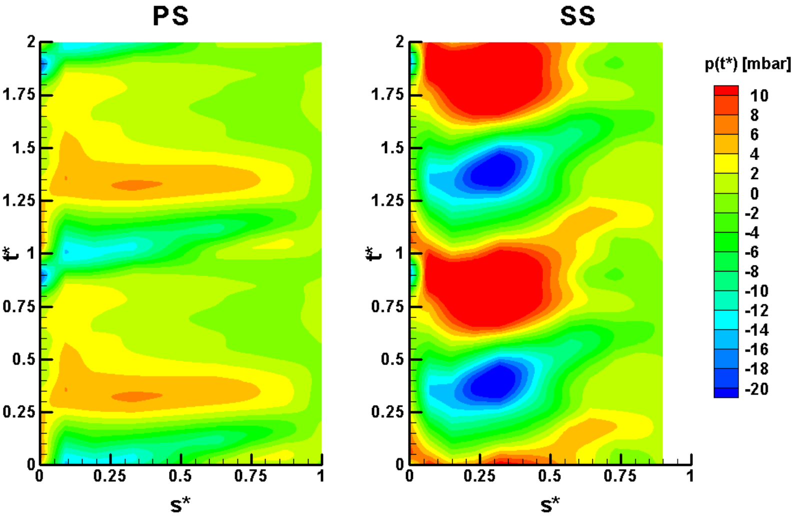

FIGURE 74. time-resolved pressures, combined GR + CV measurements, subsonic test case, EO 13, f=265 [Hz], A=0.316 [°], IBPA = 180 [°], Φ = 161.7 [°]

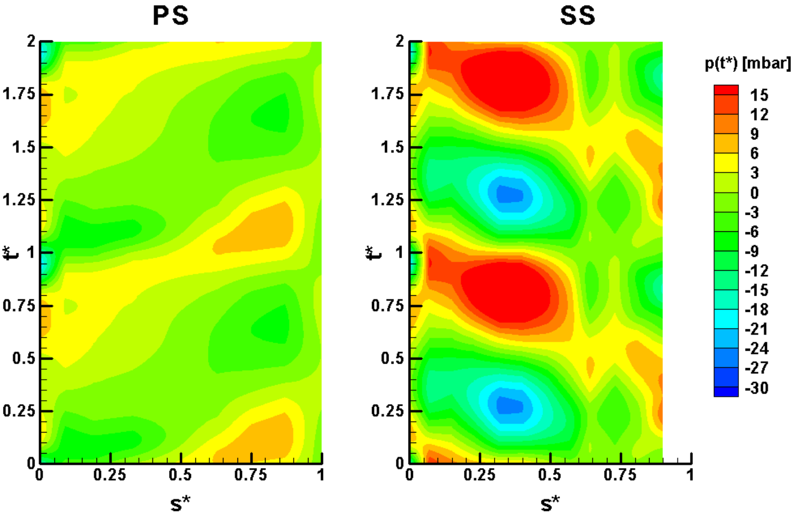

FIGURE 75. time-resolved pressures, combined GR + CV measurements, transonic test case, EO 22, f=265 [Hz], A=0.316 [°], IBPA = 180 [°], Φ = 175.3 [°]

Figure 76 to Figure 79 present the relative error spectrum plots between the simultaneous and combined measurement examples given in the previous figures. Additional examples with a different cascade vibration mode (IBPA =90 [°]) are given in Figure 80 and Figure 81.

In most cases the relative error is less than 5% as shown by blue regions in the relative error contour plots. Relative error peaks of up to 30% are represented with red zones and can be found in the transonic flow region of the SS (Figure 77, Figure 79 and Figure 80), as well as at the TE location (on PS plots) for both flow conditions. Regions with intermediate relative error (5 to 12%) are represented in green and can be seen near the TE, especially on the SS.

As previously seen in the amplitude spectra of the simultaneous measurements, the overall amplitude of the pressure disturbance fades out near the TE and is specially weak on the SS. Since the amplification of the time-dependent pressure signals has the same settings for all measurements and measurement locations, the precision of the data acquisition drops with diminishing signal amplitude, which is the case near the TE. As expected from the definition of the relative error (equation (6.2) on page 91) and from the amplitude spectra plots of the simultaneous gust response and controlled vibration measurements, the relative error generally diminishes with increasing frequency, such that secondary peaks appear at the higher harmonic frequencies.

The transonic test cases presented in Figure 77, Figure 79 and Figure 80 are representative of all the transonic measurements conducted in this study (137 cases). In the first case the maximum relative error in the transonic flow region (27%) is found on two neighboring unsteady pressure transducer SS 13 and SS 14. The error then drops down to 10% as the measuring location approaches the TE. This is most likely due to the variation of shock position between controlled-vibration only, gust-response only and simultaneous measurements. As seen in the previous chapter, small differences in the main flow conditions and in the steady blade surface pressure distributions cannot be avoided between test configurations with rotor and without rotor. Considering the sensitivity of shocks to these types of variations, it is likely that the shock position varies over one or two measuring locations between these three configurations. Of course, on should also consider the important unsteady nature of the shock, especially regarding the complexity of boundary-layer shock interactions on vibrating blades in the presence of gusts and important unsteady secondary flow effects. These two different effects probably cumulate over the SS 13 and SS 14 captors and their influence is less perceptible as one approaches the TE.

In Figure 79, the maximum relative error in the transonic flow region (28%) is this time found at the SS 13 and SS 11 location with a drop to 14% at SS 12. Therefore, it is also possible that the shock oscillates between SS 13 and SS 11 with a rapid crossing over the mid-location SS 12, but it is not possible to affirm it without using a more detailed measuring technique (in time and space), which is beyond the scope of the current study.

In Figure 80 the maximum relative error in the transonic region (23%) occurs at the SS 12 location with decreasing values as the measuring location approaches the TE. In all three cases it is not possible to distinguish shock position effects and transonic flow effects on the validity of the superposition principle studied in this dissertation, primarily for two reasons:

first of all, the spatial resolution isn't fine enough considering the small size of the transonic region. Furthermore, the assumed shock's oscillation and location variations between test configurations seem to affect a large zone that varies between measurements.

With the current measurements it is not possible to determine precisely the different shock positions resulting from the different test configurations and further analyze the effect of their locations on the validity of the linear superposition principle.

Nevertheless, it can be affirmed that in the region where shocks appear the superposition principle isn't valid mainly because the mean localization of the shock varies between the simultaneous gust response and controlled vibration, controlled-vibration only and gust-response only measurements.

The other large discrepancies observed at the TE location are expectable considering the dominant viscous effects at this discrete location and possible interactions with passing wakes, moving blades, secondary flow effects and small changes in main flow conditions, phenomena which they are sensitive to. Nevertheless, this particular zone has negligible effect on the overall aerodynamic excitation of the blade since the time-dependent pressure levels are comparably small and only acting on a reduced area with very small moment arm around the torsional axis.

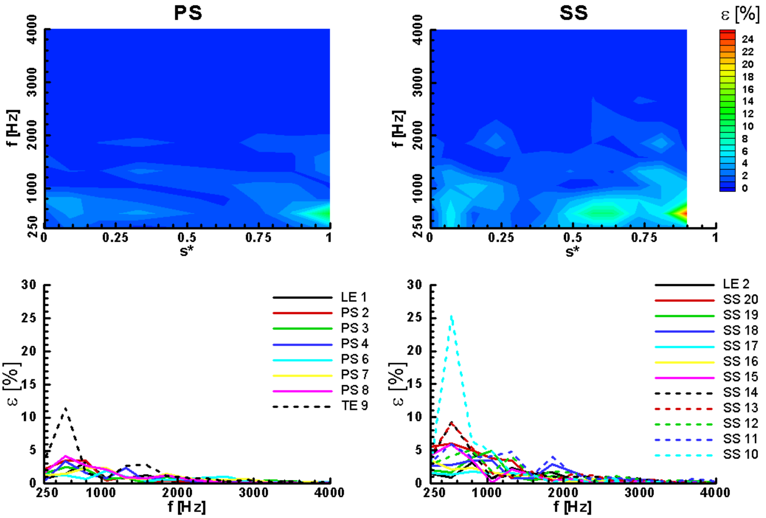

FIGURE 76. error spectrum plots between simultaneous and combined measurements, subsonic test case, EO 13, f=265 [Hz], A=0.316, IBPA = 180, Φ = 0.7 [°]

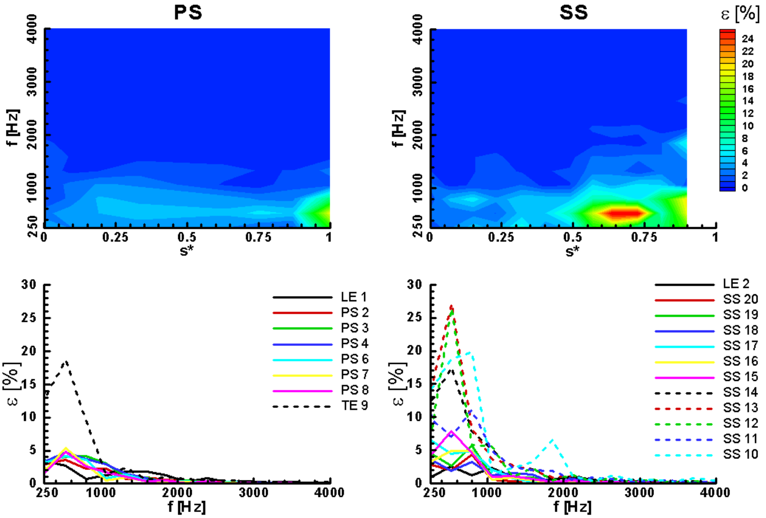

FIGURE 77. error spectrum plots between simultaneous and combined measurements, transonic test case, EO 22, f=265 [Hz], A=0.316, IBPA = 180, Φ = 358.3 [°]

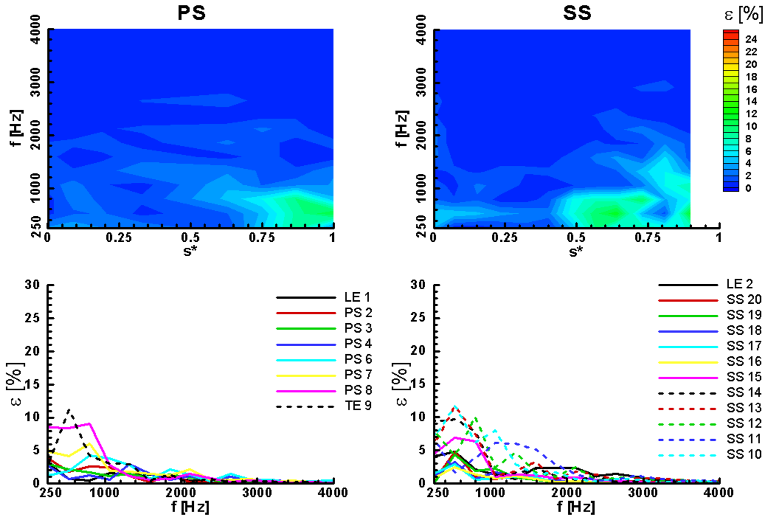

FIGURE 78. error spectrum plots between simultaneous and combined measurements, subsonic test case, EO 13, f=265 [Hz], A=0.316, IBPA = 180, Φ = 161.7 [°]

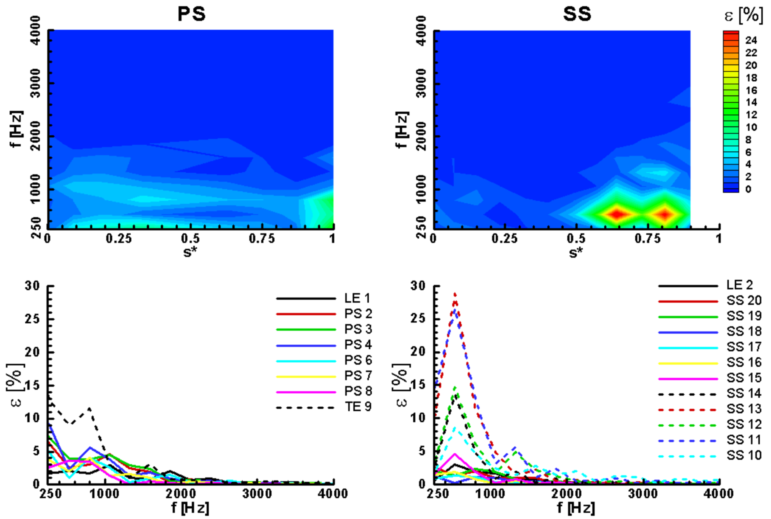

FIGURE 79. error spectrum plots between simultaneous and combined measurements, transonic test case, EO 22, f=265 [Hz], A=0.316, IBPA = 180, Φ = 175.3 [°]

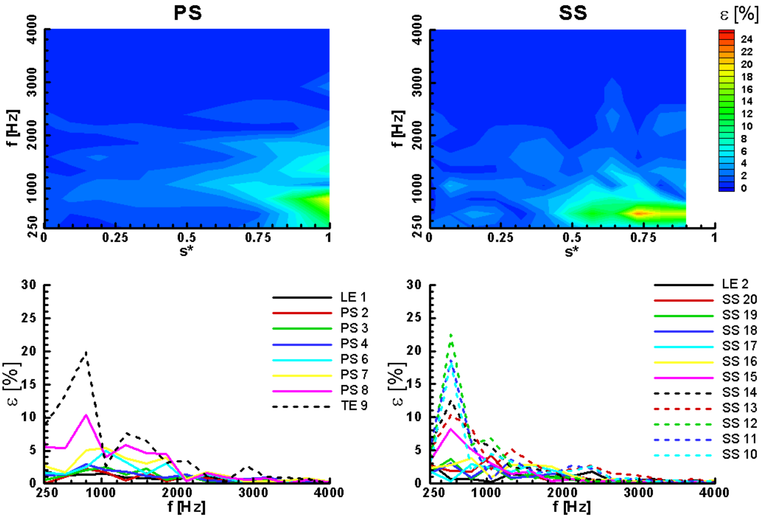

FIGURE 80. error spectrum plots between simultaneous and combined measurements, transonic test case, EO 13, f=265 [Hz], A=0.316, IBPA = 90, Φ = 227.9 [°]

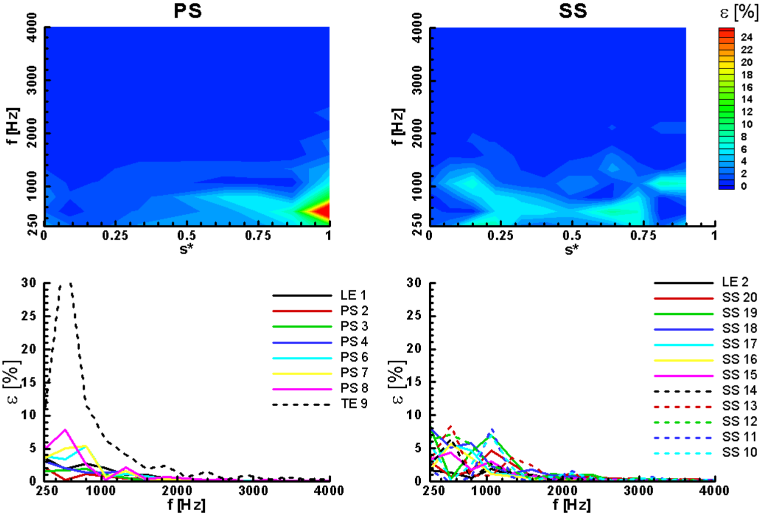

FIGURE 81. error spectrum plots between simultaneous and combined measurements, subsonic test case, EO 22, f=265 [Hz], A=0.316, IBPA = 90, Φ = 7.7 [°]

Figure 82 and Figure 84 present the averaged error spectra for the subsonic and transonic measurements, respectively. Similarly, Figure 83 and Figure 85 show the corresponding standard deviations associated with the previous averaged data; these averages are based on 115 and 137 measurements, respectively, both including the variation of engine order (13 and 22), cascade's controlled vibration mode (IBPA = 0, 90, 180, 270 [°]) and gust-vibration phase angle (around twenty different Φ values).

As observed previously with the error spectrum examples, simultaneous and linearly-combined gust response and controlled vibration measurements have excellent overall agreement, except in the transonic flow region and at the TE where discrepancies appear. The averaged relative errors are particularly low (<3%) for the subsonic test case and on the PS surface near the LE. Furthermore, they are associated with remarkably low relative error dispersion since the standard deviations are less than 1% in this region.

The relative error augments slightly as one approaches the TE on the PS surface. SS surface results shown the same behavior as on the PS but with a general rise of the relative error levels and the related standard deviations. This effect is mainly due to the constant amplification settings used throughout all unsteady pressure measurements conducted in this work. Since the random errors (see section 3.5 p. 62) are quasi-constant as opposed to the overall time-dependent pressure signal amplitude that diminishes as one approaches the TE, the relative error and its standard deviations rise accordingly. In other words, the evolution of relative error on the blade surface can be directly linked to the first harmonic amplitude of the pressure disturbance, the overall dominant amplitude influencing the signal-to-noise ratio of the data acquisition.

As seen in the previous sections, the gust has a dominant effect at the LE and its amplitude diminishes as it is convected towards the TE. The SS is also less affected by the gust than the PS as this later surface faces the gust and shades the SS. It is, therefore, the measurement errors based on the ratio between constant noise and variable overall pressure disturbance amplitude that mainly affects the quality of the superposition principle studied in this dissertation and not a physical effect. Besides a slight general augmentation of the averaged relative error values and associated standard deviations, the transonic results exhibit large discrepancies in the transonic flow region.

As one can observe in the SS results of Figure 84, the averaged relative errors are low in the first portion of the blade (<4%), but a sudden rise of up to a factor of five is observable in the second part of the blade, near the TE. Furthermore, a general error peak is present at location SS 13 and SS 12 (~15%), in the region where shock effects have been observed in the relative error plots. In these examples, the maximum relative errors were of up to 25%. Since these values are lower (15%) in the averaged transonic data and that the level of standard deviation are high at these location, the averaging process show that there are variations on the localization of the shock effects between all the different transonic test cases, as shown previously with the individual transonic examples. Of course, the time-averaging process as a similar dispersion effect on the results since the shock probably oscillates at higher frequencies than they are sampled or oscillates stochastically. In other words, both averaging processes will disperse errors if a discrete peak is present but moves in time and between runs. Therefore, it is not possible to examine the effect of the supersonic flow region on the linear superposition principle but one can still conclude that in the region influenced by shocks this assumption is not valid at all.

In summary, the averaged relative error results show that very good quantitative agreement is obtained between simultaneous and linearly-combined gust response and controlled vibration measurements except in the region influenced by shocks and at the TE, where discrepancies occur. In these regions, the average errors rise by a factor of five discrediting the linear superposition principle of unsteady pressures, especially considering the dispersion of errors due to the averaging processes.

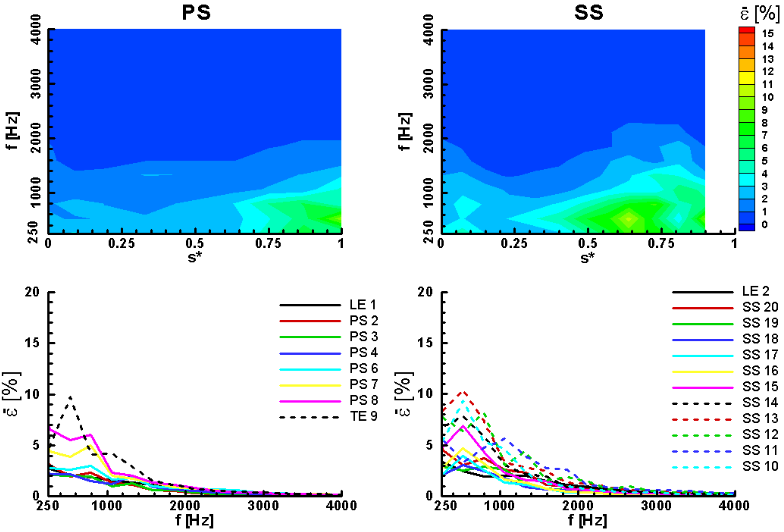

FIGURE 82. averaged error spectrum plots between simultaneous and combined measurements, subsonic test cases (115 samples)

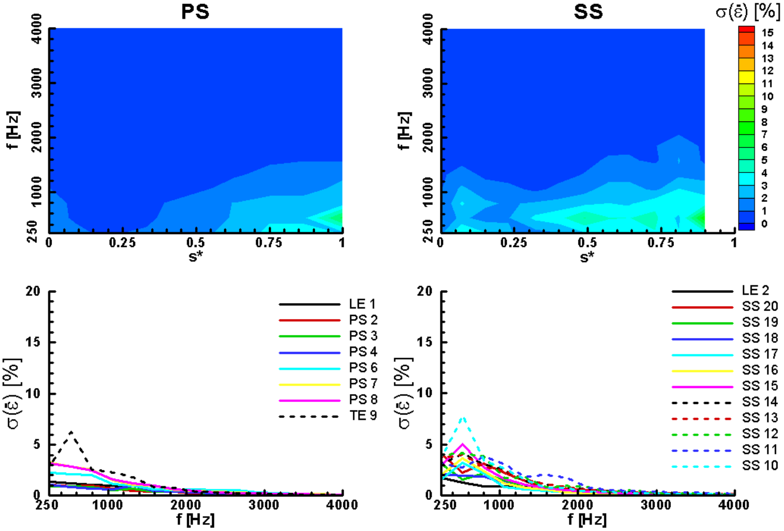

FIGURE 83. standard deviation on error spectrum plots between simultaneous and combined measurements, subsonic test cases (115 samples)

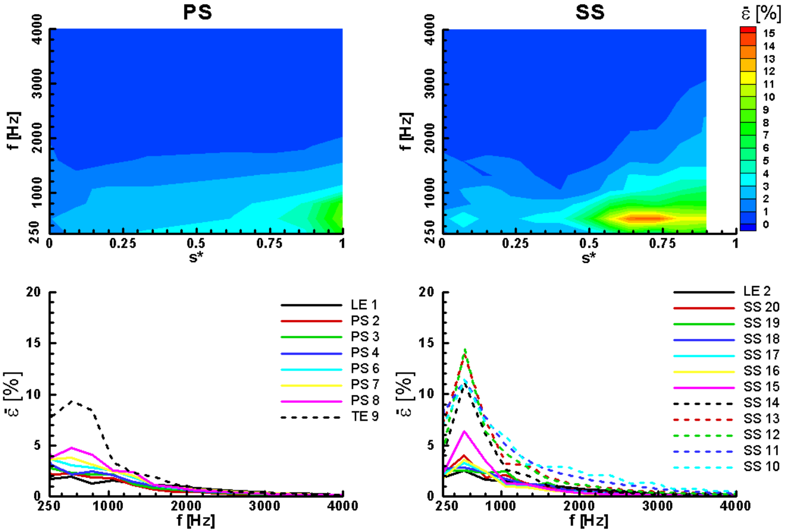

FIGURE 84. averaged error spectrum plots between simultaneous and combined measurements, transonic test cases (137 samples)

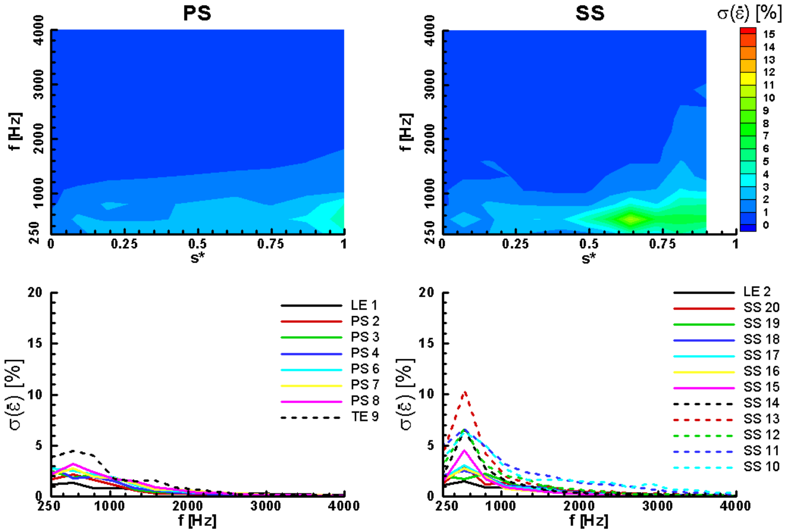

FIGURE 85. standard deviation on error spectrum plots between simultaneous and combined measurements, transonic test cases (137 samples)

Figure 86 to Figure 91 present the time-dependent signal's cross-correlation curves defined in equation (6.5) on page 91 for the six relevant examples showed previously as relative error plots. These figures composed of cross-correlation curves and contour plots allow to compare simultaneous and linearly-combined GR & CV results on phase effects by determining the peak correlation value and its associated optimal time-lag. The optimal correlation value gives a more precise indication of the phase shift between simultaneous and combined signals since the resolution on k is limited by the sampling rate to increments of approximately 4 [°]. The overall cross-correlation curves permit to check the uniqueness of the optimal cross-correlation.

As revealed by the examples presented, the overall agreement regarding the phase is excellent, except at the TE and in the transonic flow region. In the contour plots, a horizontal red line at 0 [°] indicate that simultaneous and combined GR & CV signals are in phase to a high precision as shown by peak values of cross-correlation between 0.9 and 1.

As observed in the previous sections, the quality of the results fades out towards the TE and is higher on the PS surface than the SS surface. Again this effect is attributed to the combination of quasi-constant measurement errors with reduced measurement signal levels and the induced augmentation of measurement uncertainty.

In general the level of the cross-correlation diminishes slightly towards the TE but the optimal time-lag parameter stays close to zero. The transonic flow region and the TE location exhibit different effects and much larger discrepancies. The TE location has either very low correlation values and/or important phase-shift values k. In some case there are even two major peaks with +/- 180 [°] k values (Figure 91), indicating that the main harmonic component is in phase opposition between simultaneous and linearly-combined measurements. As previously stated, this location doesn't show any relevant physical interest besides pointing out the peculiar unsteady behavior at this discrete location.

The transonic flow region, presented in Figure 87, Figure 89 and Figure 90, as an important effect on the cross-correlation between simultaneous and combined GR & CV signals. In this region, represented by dashed lines in the SS cross-correlation plots, the cross-correlation peak values drop and have important phase-shifts of up to 90 [°]. This effect is particularly visible between location SS 13 and SS 11 and fades out at the SS 10 location, close to the TE.

This shows that shocks have different effects between simultaneous and combined GR & CV measurements. Since all acquired signals are time-averaged over one period, it is not possible to state which signal between simultaneous and linearly-combined measurements leads the other, but that an important phase shift is present and it can be attributed to the variation of the shock's mean location and its physical behavior between the simultaneous and the separated measurements.

As discussed previously, a supersonic flow region cannot be dissociated from the region influenced by the shocks that spreads over a large portion of the SS blade surface near the TE. It can nevertheless be concluded that the shock effects differ between simultaneous and combined GR & CV experiments and therefore discredit the linear superposition principle studied in this work where they are present.

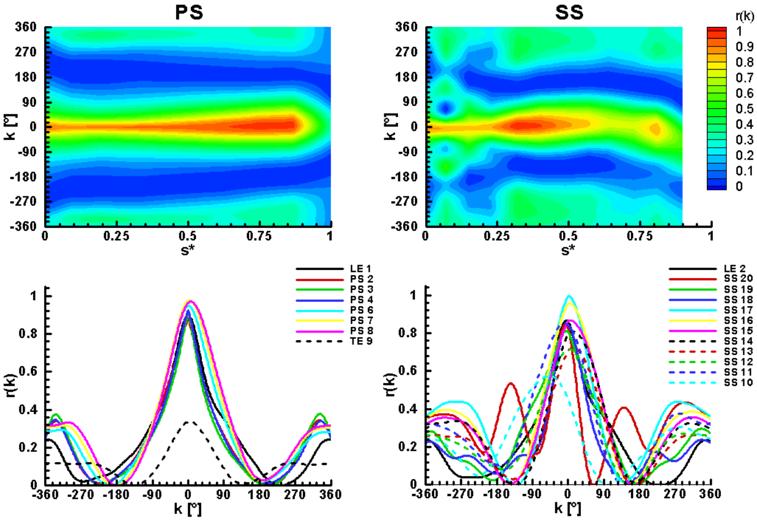

FIGURE 86. cross-correlation plots between simultaneous and combined measurements, subsonic test case, EO 13, f=265 [Hz], A=0.316, IBPA = 180, Φ = 0.7 [°]

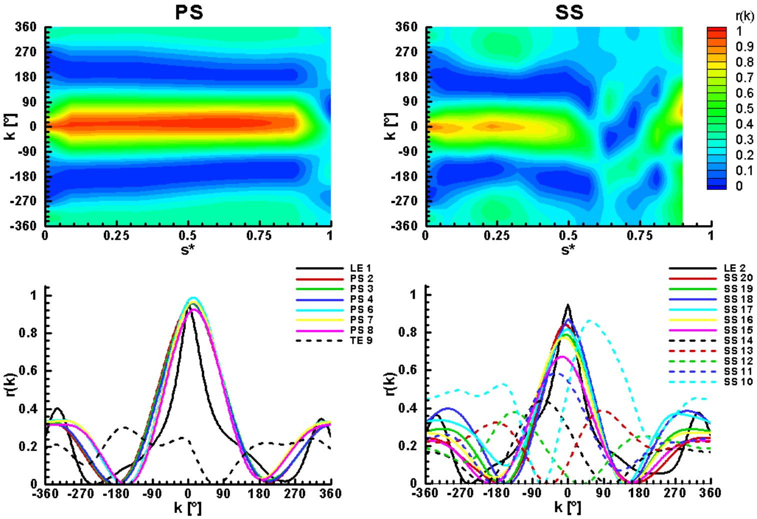

FIGURE 87. cross-correlation plots between simultaneous and combined measurements, transonic test case, EO 22, f=265 [Hz], A=0.316, IBPA = 180, Φ = 358.3 [°]

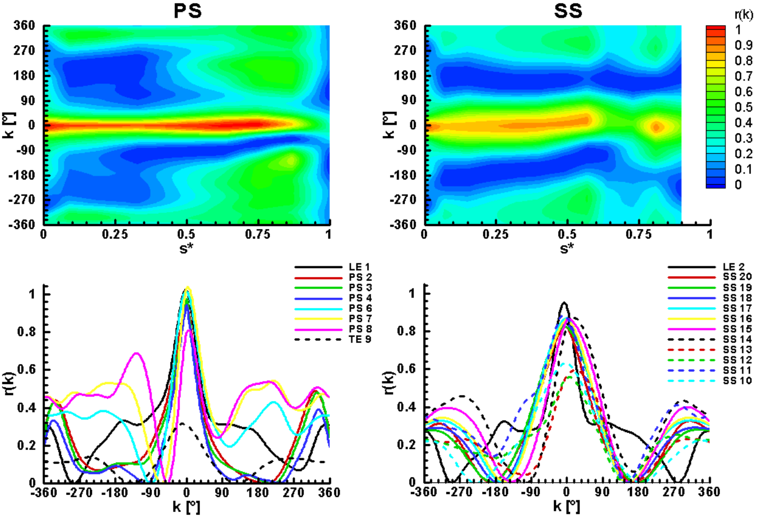

FIGURE 88. cross-correlation plots between simultaneous and combined measurements, subsonic test case, EO 13, f=265 [Hz], A=0.316, IBPA = 180, Φ = 161.7 [°]

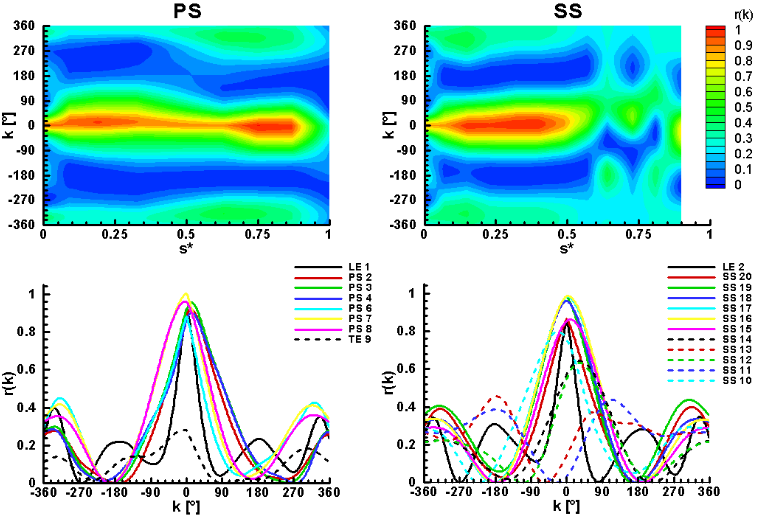

FIGURE 89. cross-correlation plots between simultaneous and combined measurements, transonic test case, EO 22, f=265 [Hz], A=0.316, IBPA = 180, Φ = 175.3 [°]

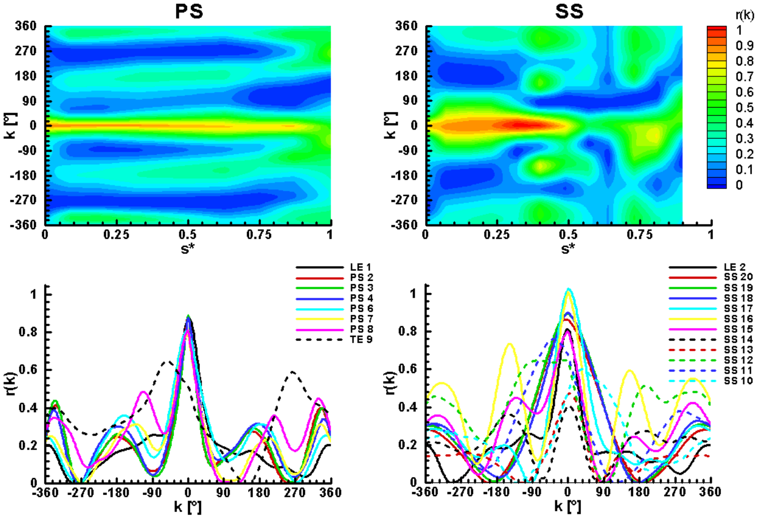

FIGURE 90. cross-correlation plots between simultaneous and combined measurements, transonic test case, EO 13, f=265 [Hz], A=0.316, IBPA = 90, Φ = 227.9 [°]

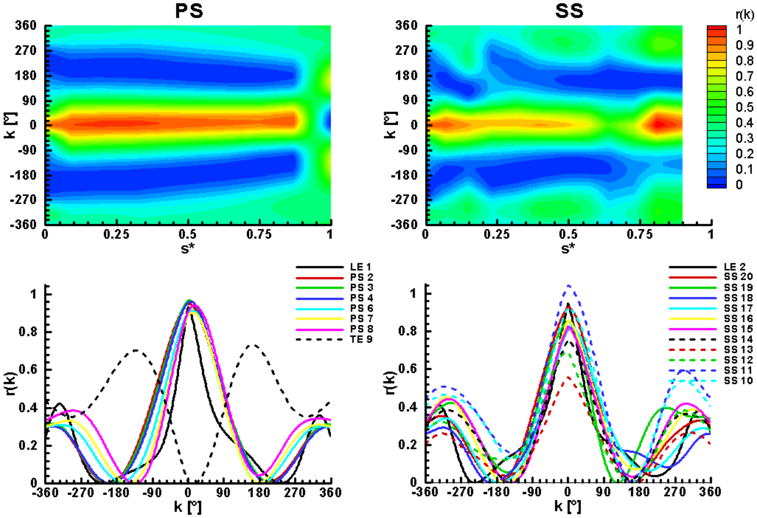

FIGURE 91. cross-correlation plots between simultaneous and combined measurements, subsonic test case, EO 22, f=265 [Hz], A=0.316, IBPA = 90, Φ = 7.7 [°]

In the current work, a statistical approach has been carried out on the cross-correlation results in order to isolate the effect of the numerous test parameters varied in this study (flow conditions, engine order, cascade's vibration mode, gust-vibration phase angle).

Besides the previously observed effects between subsonic and transonic flow regime, one other dominant effect has been identified. For practically all measuring locations and every test case (combination of EO, IBPA and flow conditions) a strong dependency has been observed between the cross-correlation peak values and the gust-vibration phase angle Φ.

Two examples of such effects are given in Figure 92 for the subsonic test case, location SS 13 and for two different cascade vibration mode (IBPA = 180, 270 [°]). Both examples exhibit a quasi-sinusoidal variation of the cross-correlation peak values (represented with dots in Figure 92) as a function of the gust-vibration phase angle Φ. These measurements are compared with the first harmonic amplitude variation of the combined gust response and controlled vibration results for the same location and test case. Represented with continuous lines, these curves have been reconstructed from the first harmonic component of the gust-response only measurement and adding the first harmonic component of the controlled-vibration only measurement but with a variable gust-vibration phase angle Φ.

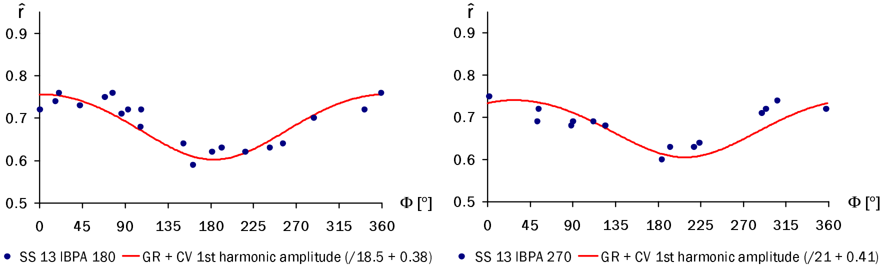

FIGURE 92. effect of gust-vibration phase angle Φ on cross-correlation peak values, subsonic measurement, engine order 13, location SS 13

In order to compare both results (with different units), the first harmonic amplitude plots have been scaled on the x-axis to match the overall variation of cross-correlation peaks.

These two figures show that a direct relation can be found between the overall amplitude of the acquired signal and the corresponding cross-correlation peak values. For example if the dominant harmonic signal of gust-response only measurements and the controlled-vibration only signal are in phase, they interact constructively such that a peak on the amplitude appears. On the contrary, if these two signals interact destructively, or in other words are in phase opposition, the overall amplitude will drop.

Considering the constant unsteady pressure signal amplification and the quasi-constant measurement errors, the relative data acquisition error will augment if the unsteady pressure signal's overall amplitude drops, and diminish if its overall amplitude rises.

As shown in Figure 92, the cross-correlation peak value variation follows the overall time-dependent pressure variations indicating a direct dependency between the quality of the optimal cross-correlation values and the precision of the time-dependent data acquisition.

Therefore, the effects of the gust-vibration phase angle Φ on the quality of the cross-correlation between simultaneous and linearly-combined GR & CV measurements is mainly due to relative measurement error variations and not due to physical effects that would discredit to some extent the linear superposition principle of unsteady pressures studied in this dissertation.

The same effect has been observed on the averaged relative error contour plots from LE to TE and between the PS surface and the SS surface, as previously stated in this section. Similarly, slight differences have been observed between engine order 13 and 22 averaged cross-correlation values. As previously described in section section 5.4 on page 99, the overall gust amplitude is higher for an engine order of 13 since the wake passing frequency is kept constant. Again, the overall quality on simultaneous and linearly-combined results augments for an engine order of 13 as the ratio between overall time-dependent pressure amplitude and measurement error, or noise, rises.

In summary, the quasi-constant measurement noise levels (for a given flow condition), in combination with variable overall unsteady pressure amplitudes on a fixed data acquisition range, has an important influence on the precision of the time-dependent pressure measurement and, therefore, on the relative error between simultaneous and linearly-combined GR & CV results. Depending on a constructive or destructive combination of the dominant first harmonic pressure signal of controlled-vibration only and gust-response only measurements, the precision of the simultaneous signal will vary significantly.

Furthermore, the general trend of diminishing time-dependent pressure from the LE to the TE and from PS surface to the SS surface has an additional relative measurement error effect. Similarly, the reduction of the gust's amplitude due to a higher engine order and/or lower inflow Mach number will augment again the relative measurement error in a cumulative manner.

Besides in the transonic flow region and at the TE location, the total relative error between simultaneous and linearly-combined results is, in the worst case scenario, always less than 10%. In fact, the majority of results have a relative error comprised between 2 to 5% with best cases having less than 2% relative error. Considering the total measurement error on time-dependent pressures of ±1% (see section 3.4 p. 56), that are cumulated for combined measurements, the qualitative agreement between simultaneous and combined measurements is generally very good to excellent (near the LE).

Since the relative error is mainly dependant on the data acquisition process and not on the different parameters varied in this study, the linear superposition principle of unsteady pressures between gust response and controlled vibration measurements can be considered qualitatively valid for all varied quantities except in the transonic flow region, where significant discrepancies appear.

5.7 Executive Summary

The controlled-vibration only measurements have shown that the blade surface time-dependent pressures induced by the cascade's travelling wave vibration mode have only one significant harmonic for all measured flow conditions, IBPA and blade surface location. The Fourier analysis carried on the time-dependent signals revealed excellent signal-to-noise ratio for all test cases and locations, including at the TE. An aerodynamic stability analysis has been carried out showing that the cascade is aerodynamically stable in torsion and for the two flow conditions tested (see APPENDIX B on page 151). This analysis has also shown that the aerodynamic coupling only involves three to four neighboring blades in this vibration mode and cascade configuration.

The gust-response only measurements have shown that the blade surface time-dependent pressures induced by the gusts generators have four and six significant harmonics for an engine order of 22 and 13, respectively. The Fourier analysis carried on the time-dependent signals revealed excellent signal-to-noise ratio for all test cases and locations, including at the TE, giving great confidence in the newly developed data acquisition technique and harmonic signal analysis. Since the wake passing frequency is kept constant between both engine orders[1], It has been observed that the differences in wake profiles impinging on the blade is mainly a higher velocity defect and narrower wake profile for an engine order of 13. In both cases, the wake-induced pressure disturbance on the blade surface fades out rapidly from LE to TE, indicating the dominant potential effect of the generated wakes. These disturbances are weaker on the SS than on the PS as this latter surface faces the gust and shades the SS. The comparison between the subsonic and transonic results, for each engine order, shows that generally the pressure levels augment slightly in the transonic case, except in the transonic flow region where higher amplification and important phase effects are present.

The unsteady wake measurements, conducted with Oxford's unsteady wedge probe, have demonstrated the high level of flow periodicity between two blade passages. These results, presented in APPENDIX C on page 157, have also pointed out an important potential effect of the measuring cascade.

Simultaneous gust response and controlled vibration measurements have shown that the blade surface time-dependent pressures induced by both excitation sources have four and six significant harmonics for an engine order of 22 and 13, respectively, just like gust-response only measurements. The Fourier analysis carried on the time-dependent signals revealed excellent signal-to-noise ratio for most test cases and locations. The simultaneous measurements have demonstrated the important influence of the gust-vibration phase angle Φ on the blade surface time-dependent pressure distribution and has identified it as the key parameter. For a given test configuration and flow condition, the selection of the gust-vibration phase angle allows a local constructive or destructive interaction between the main harmonics of both excitation sources. Furthermore, the simultaneous results have demonstrated that this effect can be extended to either the PS or SS surface for the given test configuration and flow conditions. Generally, this suggests that the gust-vibration phase angle has an important effect on the time-dependent pressure distribution for simultaneous GR & CV measurements and, therefore, on the excitation levels and excited modes. In other words, it is more than

---

[1] *Both wake generators are equipped with the same type of elliptical struts (see section 2.3 on page 35).*

likely that the judicious choice of a gust-vibration phase angle can significantly diminish the aerodynamic excitation levels for a given cascade vibration mode, flow condition, and test configuration of a single stage.

The comparison between simultaneous and linearly-combined gust response and controlled vibration measurements has demonstrated that the linear superposition principle of unsteady pressures is qualitatively and quantitatively valid for all varied quantities except in the transonic flow region. In this reduced zone, the effects of shocks and the transonic pocket could not be dissociated since the influence of the shocks on the measurements spread over a relatively large region for two main reasons: first of all, the location of the shock varies significantly between gust-response only, controlled-vibration only and simultaneous measurements, as slight differences in blade surface steady pressure distributions are unavoidable considering the differences in test configurations (presence of different strutted rotors). The second reason is related to the unsteady nature of the shock and to the data acquisition technique used in the current study. Considering the complexity of boundary-layer shock interactions in an unsteady environment with vibrating blades, in the presence of gusts and important unsteady secondary flow effects; the shock impinging on the blade SS surface has surely a non-periodic high frequency motion. On the other hand, the data acquisition technique has been specially developed for a precise detection of periodic signals with a maximum frequency of 8.5 [kHz] with a limited spatial resolution. Therefore, the nature of the shock is most likely truncated by the limited bandwidth, spatial resolution and the time-averaging process. Nevertheless, important discrepancies remain in the region influenced by the different shocks and discredit the local validity of the superposition principle in their presence. This effect has been further demonstrated with an analysis of the cross-correlation between simultaneous and linearly-combined measurements, pointing out prominent phase shifts in this region. On the other hand, the limited transonic zone and the wide region influenced by shocks could not allow an evaluation of the validity of the linear superposition principle in the supersonic regime.

The comparison of simultaneous and linearly-combined measurements has also shown that the relative error between them is highly dependent on the overall amplitude of the simultaneous measured pressure disturbance. Since either a constructive or destructive interaction can occur between the dominant harmonics of controlled-vibration only and gust-response only measurements, the overall time-dependent pressure amplitudes of the simultaneous case will vary greatly. It has also been shown that the precision on the unsteady pressure measurement is highly dependant on the overall pressure amplitude, as constant noise levels become relatively more important if this signal’s amplitude diminishes and vice-versa.

Finally, it has been pointed out that the linear superposition principle of unsteady pressures between gust response and controlled vibration experiments holds locally for all quantities varied in this study (cascade vibration mode, engine order, flow conditions), except in the transonic region, and that the relative error variations are only due to measurement errors.

CHAPTER 6 Summary and Conclusions

This chapter summarizes the key findings gathered in the current study and discusses the validity of the linear superposition principle of unsteady pressures due to upstream generated gusts and due to the cascade's vibration mode.

The first section presents the main conclusions drawn from steady-state results and addresses the validity of this basis for the unsteady measurement comparisons. It is followed by a summary of the key findings of the time-dependent results in the following order: controlled-vibration only, gust-response only, simultaneous and linearly combined gust response and controlled vibration results. Furthermore, this section addresses the validity of the linear superposition of unsteady pressures for all tested configurations and flow conditions.

The following section discusses the overall validity of the linear superposition principle by enumerating the possible extensions of this principle on each quantity varied in this study.

Finally, the last section summarizes the main conclusions of this dissertation and points out the practical advantages of this principle.

6.1 Steady-State Results

The steady probe and blade surface measurements have shown a high level of steady flow periodicity over the blade passages and quasi-constant inflow conditions. They have also revealed the presence of secondary flow effects constituted mainly of a tip gap vortex and leakage flows through the labyrinth seals of the blade bases. The effect of each is clearly visible near the casing and near the hub, respectively, but they do not contaminate the measurements conducted in the mid-channel region, where unsteady measurements are conducted as well. In this region, the quasi-two-dimensional flow assumption is considered valid for both studied flow conditions.

The steady-state results for the different test configurations exhibit very good agreement among them for both flow cases, ensuring almost identical steady flow conditions between cases where the superposition of unsteady pressures are to be studied. Small differences cannot be avoided considering the three different test configurations (no rotor EO 13, EO 22) and the presence of different gust profiles in the time-averaging process of the two engine orders. It is believed that the presented results are an optimal compromise between differences observed at the LE and at the TE, so that the overall steady loadings of the blades are identical for the three test configurations.

The transonic test case is characterized by a supersonic flow region on the second-half of the suction side of the blades and greater secondary flow effects than for the subsonic test case. It has been shown that the quasi-two-dimensional flow assumption is still valid around the mid-channel height measuring location, where the linear superposition principle of unsteady pressures has been studied.

Considering that, for both flow conditions and all the different test configurations, the quasi-two-dimensional flow assumption is valid around the mid-channel height, and since the blade surface steady pressure distributions is quasi-identical for each flow conditions, the basis of the unsteady flow comparisons can be considered constant enough for a precise two-dimensional time-dependent surface pressure analysis. Therefore, the steady-state results should not significantly affect the time-dependent results. Consequently, the validation of the linear superposition principle studied in this dissertation should not be influenced by the steady flow conditions.

6.2 Time-Dependent Results

The controlled-vibration only measurements have shown that the blade surface time-dependent pressures induced by the cascade's travelling wave vibration mode have only one significant harmonic for all measured flow conditions, IBPA and blade surface location. The Fourier analysis carried on the time-dependent signals revealed excellent signal-to-noise ratio for all test cases and locations, including at the TE. An aerodynamic stability analysis has been carried out showing that the cascade is aerodynamically stable in torsion and for the two flow conditions tested (see APPENDIX B on page 151). This analysis has also shown that the aerodynamic coupling only involves three to four neighboring blades in this vibration mode and cascade configuration.

The gust-response only measurements have shown that the blade surface time-dependent pressures induced by the gusts generators have four and six significant harmonics for an engine order of 22 and 13, respectively. The Fourier analysis carried on the time-dependent signals revealed excellent signal-to-noise ratio for all test cases and locations, including at the TE, giving great confidence in the newly developed data acquisition technique and harmonic signal analysis. Since the wake passing frequency is kept constant between both engine orders[1], It has been observed that the differences in wake profiles impinging on the blade is mainly a higher velocity defect and narrower wake profile for an engine order of 13. In both cases, the wake-induced pressure disturbance on the blade surface fades out rapidly from LE to TE, indicating the dominant potential effect of the generated wakes. These disturbances are weaker on the SS than on the PS as this latter surface faces the gust and shades the SS. The comparison between the subsonic and transonic results, for each engine order, shows that generally the pressure levels augment slightly in the transonic case, except in the transonic flow region where higher amplification and important phase effects are present.

The unsteady wake measurements, conducted with Oxford's unsteady wedge probe, have demonstrated the high level of flow periodicity between two blade passages. These results, presented in APPENDIX C on page 157, have also pointed out an important potential effect of the measuring cascade.

Simultaneous gust response and controlled vibration measurements have shown that the blade surface time-dependent pressures induced by both excitation sources have four and six significant harmonics for an engine order of 22 and 13, respectively, just like gust-response only measurements. The Fourier analysis carried on the time-dependent signals revealed excellent signal-to-noise ratio for most test cases and locations. The simultaneous measurements have demonstrated the important influence of the gust-vibration phase angle Φ on the blade surface time-dependent pressure distribution and has identified it as the key parameter. For a given test configuration and flow condition, the selection of the gust-vibration phase angle allows a local constructive or destructive interaction between the main harmonics of both excitation sources. Furthermore, the simultaneous results have demonstrated that this effect can be extended to either the PS or SS surface for the given test configuration and flow conditions. Generally, this suggests that the gust-vibration phase angle has an important effect on the time-dependent pressure distribution for simultaneous GR & CV measurements and, therefore, on the excitation levels and excited modes. In other words, it is more than

---

[1] *Both wake generators are equipped with the same type of elliptical struts (see section 2.3 on page 35).*

likely that the judicious choice of a gust-vibration phase angle can significantly diminish the aerodynamic excitation levels for a given cascade vibration mode, flow condition, and test configuration of a single stage.

The comparison between simultaneous and linearly-combined gust response and controlled vibration measurements has demonstrated that the linear superposition principle of unsteady pressures is qualitatively and quantitatively valid for all varied quantities except in the transonic flow region. In this reduced zone, the effects of shocks and the transonic pocket could not be dissociated since the influence of the shocks on the measurements spread over a relatively large region for two main reasons: first of all, the location of the shock varies significantly between gust-response only, controlled-vibration only and simultaneous measurements, as slight differences in blade surface steady pressure distributions are unavoidable considering the differences in test configurations (presence of different strutted rotors). The second reason is related to the unsteady nature of the shock and to the data acquisition technique used in the current study. Considering the complexity of boundary-layer shock interactions in an unsteady environment with vibrating blades, in the presence of gusts and important unsteady secondary flow effects; the shock impinging on the blade SS surface has surely a non-periodic high frequency motion. On the other hand, the data acquisition technique has been specially developed for a precise detection of periodic signals with a maximum frequency of 8.5 [kHz] with a limited spatial resolution. Therefore, the nature of the shock is most likely truncated by the limited bandwidth, spatial resolution and the time-averaging process. Nevertheless, important discrepancies remain in the region influenced by the different shocks and discredit the local validity of the superposition principle in their presence. This effect has been further demonstrated with an analysis of the cross-correlation between simultaneous and linearly-combined measurements, pointing out prominent phase shifts in this region. On the other hand, the limited transonic zone and the wide region influenced by shocks could not allow an evaluation of the validity of the linear superposition principle in the supersonic regime.

The comparison of simultaneous and linearly-combined measurements has also shown that the relative error between them is highly dependent on the overall amplitude of the simultaneous measured pressure disturbance. Since either a constructive or destructive interaction can occur between the dominant harmonics of controlled-vibration only and gust-response only measurements, the overall time-dependent pressure amplitudes of the simultaneous case will vary greatly. It has also been shown that the precision on the unsteady pressure measurement is highly dependant on the overall pressure amplitude, as constant noise levels become relatively more important if this signal’s amplitude diminishes and vice-versa.

Finally, it has been pointed out that the linear superposition principle of unsteady pressures between gust response and controlled vibration experiments holds locally for all quantities varied in this study (cascade vibration mode, engine order, flow conditions), except in the transonic region, and that the relative error variations are only due to measurement errors.

6.3 Validity of the Superposition Principle

In the current study, it has been demonstrated that the linear superposition principle of unsteady pressures due to upstream generated gusts and due to the cascade's vibration mode is locally valid, on the blade surface, for various test configurations and flow conditions with one exception being the region influenced by shocks for the transonic test case.

Four different IBPA were selected for the cascade's controlled vibration mode in the simultaneous measurements without discrediting the linear superposition principle. Since all possible IBPA for the travelling wave mode (20) were tested in the controlled-vibration only measurements and did exhibit a similar physical behavior (single sine tones, linear superposition principle of unsteady pressure due to vibrating blades valid, see APPENDIX B on page 151), there is great confidence in concluding that the linear superposition principle holds for all IBPA.

Similarly, two different engine orders (13 and 22) were tested and have both confirmed the validity of the superposition principle for a lower and higher engine order than the number of blades (20). Besides differences in total velocity defect and wake thickness due to rotor speed variation, the spatial separation of the wakes differs between both engine orders, while the temporal separation remains the same (same frequency). It is most likely that the superposition principle holds for a wider range of engine orders considering the physical nature of the generated gusts, found to have dominant potential effects. Nevertheless, It is possible that very high engine orders will discredit the validity of the superposition principle as neighboring wakes will interact in blade-to-blade passages, but it is very likely that this principle holds for all lower engine orders than 22.

Previous controlled vibration results showed that the blade surface time-dependent pressures induced by the controlled vibration of a cascade assembly in the travelling wave mode have a direct relation with the movement of a reference blade to some extend (quasi-steady behavior). This implies that the validity of the superposition principle is surely valid for a range of vibration amplitudes, especially for lower vibration amplitudes. For higher torsion amplitudes than the one tested (0.6 [°] peak-to-peak) a probable physical limitation is the appearance of a separation bubble on the SS surface near the LE. Buffum & al [12] have shown that the dynamic triggering of a separation bubble occurs at higher torsion amplitudes than static flow separation. It is therefore probable that the validity of the superposition principle can extend to higher torsion amplitudes than given by the appearance of static flow separation.

Controlled vibration experiments were conducted on the same measuring cascade and flow conditions but with a bending setup. Unfortunately, simultaneous GR & CV measurements could not be performed due to the incapacity of the blade vibration control system to damp its movement and stabilize the cascade's vibration mode. Nevertheless, controlled vibration measurements showed a similar relationship between the cascade's vibration mode and the induced blade surface time-dependent pressures as for the torsion mode (quasi-steady behavior, linear superposition principle of unsteady pressure due to vibrating blades valid). It is therefore very likely that the superposition principle holds for a bending motion or any combination of bending and torsion movement with limitations on movement amplitudes.

Since the validity of the linear superposition principle of time-dependent pressures due to upstream generated gusts and due to the cascade's vibration has been demonstrated locally for subsonic flow regions, its validity can be straight forward generalized to the overall effect of the time-dependent pressure distribution on the blade, i.e.: the overall moment coefficient. Furthermore, since the influence of the transonic region is localized, the overall moment coefficient obtained from combined GR & CV measurements is a good indication of the simultaneous effects of GR & CV experiments, as localized differences are spread in the integration process.

6.4 Final Conclusions

For the first time, an experimental approach has been carried out to investigate the complete aerodynamic forced response problem on an annular turbine cascade, including effects related to the incoming aerodynamic gusts, as well as the vibration of the turbine cascade in the travelling wave mode. The local aerodynamic excitations of the blades due to these two sources of unsteady flow fields have been studied separately and simultaneously in order to investigate their local contributions to the aerodynamic excitation of the blades and their interactions in the simultaneous case. The final conclusions of this investigation are the following:

- the simultaneous measurements have demonstrated the important influence of the gust-vibration phase angle Φ on the blade surface time-dependent pressure distribution and has identified it as the key parameter. For a given test configuration and flow condition, the selection of the gust-vibration phase angle allows a local constructive or destructive interaction between the main harmonics of both excitation sources. Generally, this suggests that the gust-vibration phase angle has an important effect on the excitation levels and excited modes of the cascade. The practical implication of this phenomenon is that the judicious choice of a gust-vibration phase angle can significantly diminish the aerodynamic excitation levels for a given cascade vibration mode, flow condition and test configuration of a single stage. It is even possible that certain periodic variations of this phase angle produces another excitation source in turbomachinery.
- the simultaneous vibrating cascade and upstream generated aerodynamic gusts excitations can be accurately predicted by the linear superposition of the individual gust-induced and vibration-induced unsteady flow fields. This principle was shown to be applicable locally for various test configurations, including different engine orders, inter-blade phase angles, gust-vibration phase angles, and flow conditions. The only significant discrepancies were observed in the presence of shocks, but these were limited to a localized region reducing their importance in terms of the overall unsteady aerodynamic loading of the blade. It has been shown that these discrepancies were mainly due to the variation of the shock's mean location between gust-response only, controlled-vibration only and simultaneous measurements. The main practical advantage of this linear superposition principle is that the numerical and experimental investigation of the aerodynamic forced response problem can be separated into: (1) the identification of the local forcing-function due to upstream generated gusts only, (2) a local aerodynamic stability analysis of the cascade alone.
- the simultaneous measurements have shown that measurement errors vary significantly as the local pressure disturbance contributions due to the gusts and the cascade's vibration mode interact constructively or destructively. Particular attention is needed in simultaneous measurements in order to separate measurement error effects and physical phenomena.

CHAPTER 7

Bibliography & References

[1] Ainsworth, R. W., Allen, J. L., Batt, J. J. M., 1995, *"The Development of Fast Response Aerodynamic Probes for Flow Measurements in Turbomachinery"*, Journal of Turbomachinery, Vol. 117, pp. 625-634.

[2] Ainsworth, R. W., Miller, R. J., Moss, R. W., Thorpe, S. J., 2000, *"Unsteady Pressure Measurement"*, Measurement Science & Technology, Vol. 11, pp. 1055-1076.

[3] Ainsworth, R. W., 2001, private communication.

[4] Armstrong, E. K., and Stevenson, R. E., 1960, *"Some Practical Aspects of Compressor Blade Vibration"*, Journal Royal Aero. Soc., Vol. 64, No. 591, March, pp. 117-130.

[5] Bisplinghoff, R. L., Ashley, H., Halfman, R. L., 1955, *"Aeroelasticity"*, Addison-Wesley Publishing Company, ISBN 0-201-00595-6.

[6] Bölcs, A., 1983, *"A Test Facility for the Investigation of Steady and Unsteady Transonic Flows in Annular Cascades"*, ASME Paper 83-GT-34.

[7] Bölcs, A., and Schläfli, D., 1984, *"Flutter Phenomena in a Transonic Turbine Cascade"*, Proceedings of the Unsteady Aerodynamics of Turbomachines and Propellers Symposium, Cambridge, England, September, pp. 411-425.

[8] Bölcs, A., and Fransson, T. H., 1986, *"Aeroelasticity in Turbomachinery: Comparison of Theoretical and Experimental Cascade Results"*, Air Force Office of Scientific Research, AFOSR-TR-87-0605.

[9] Bölcs, A., Fransson, T. H., and Schläfli, D., 1989, *"Aerodynamic Superposition Principle in Vibrating Turbine Cascades"*, AGARD, 74th Specialists' Meeting of the Propulsion and Energetics Panel on Unsteady Aerodynamic Phenomena in Turbomachines, Luxembourg, August 28 - September 1.

[10] Buffum, D. H., and Fleeter, S., 1988, *"Investigation of Oscillating Cascade Aerodynamics by an Experimental Influence Coefficient Technique"*, AIAA Paper 88-2815.

[11] Buffum, D. H., and Fleeter, S., 1991, *"Wind Tunnel Effects in a Linear Oscillating Cascade"*, ASME Paper 91-GT-133.

[12] Buffum, D. H., Capece, V. R., King, A. J., El-Aini, Y. M., 1998, *"Oscillating Cascade Aerodynamics at Large Mean Incidence"*, Journal of Turbomachinery, Vol. 120, pp. 122-130.

[13] Campbell, W., 1924, *"Protection of Steam Turbine Disc Wheels from Axial Vibration"*, ASME Paper No. 1920.

[14] Capece, V. R., and Fleeter, S., 1988, *"Experimental Investigation of Multistage Interaction Gust Aerodynamics"*, ASME Paper 88-GT-56.

[15] Capone, C., 2000, *"Programme et coefficients d'étalonnage pour sondes aérodynamiques à 5 trous"*, Internal Report, LTT-2000-06.

[16] Capone, C., 2001, *"Modification du programme de dépouillement pour sondes aérodynamiques à 5 trous"*, Internal Report, LTT-2001-01.

[17] Carta, F. O., 1978, *"Aeroelasticity and Unsteady Aerodynamics"*, Chapter 22 in The Aerothermodynamics of Aircraft Gas Turbine Engines, AFAPL-TR-78-52, G. C. Oates, ed.

[18] Carta, F. O., 1982, *"Unsteady Gapwise Periodicity of Oscillating Cascaded Airfoils"*, ASME Paper 82-GT-286.

[19] Collar, A. R., 1946, *"The Expanding Domain of Aeroelasticity"*, Journal of the Royal Aeronautical Society, Vol. 50, pp. 613-636, August.

[20] Davies, M. R. D., and Whitehead, D. S., 1984, *"Unsteady Aerodynamic Moment Measurements in a Transonic Annular Cascade"*, Proceedings of the Unsteady Aerodynamics of Turbomachines and Propellers Symposium, Cambridge, England, September, pp. 487-502.

[21] Dominy, R. G., Hodson, H. P., 1992, *"An Investigation of Factors Influencing the Calibration of 5-Hole Probes for 3-D Flow Measurements"*, ASME Paper 92-GT-216.

[22] Dorney, D. J., and Verdon, J. M., 1994, *"Numerical Simulations of Unsteady Cascade Flows"*, Transactions of the ASME, Journal of Turbomachinery, Vol. 116, No. 4, pp. 665-675, October.

[23] Dring, R. P., Joslyn, H. D., Hardin, L. W., and Wagner, J. H., 1981, *"Research on Turbine Rotor-Stator Aerodynamic Interaction and Rotor Negative Incidence Stall"*, Final Report, AFWAL-TR-81-2114.

[24] Ewins, D. J., 1988, *"Structural Dynamic Characteristics of Bladed Assemblies"*, in the AGARD Manual on Aeroelasticity in Axial-Flow Turbomachines, Vol. 2, Structural Dynamics and Aeroelasticity, AGARD-AG-298, pp. 15-1 to 15-21.

[25] Ewins, D. J., and Henry, R., 1988, *“Structural Dynamic Characteristics of Individual Blades”*, in the AGARD Manual on Aeroelasticity in Axial-Flow Turbomachines, Vol. 2, Structural Dynamics and Aeroelasticity, AGARD-AG-298, pp. 14-1 to 14-27.

[26] Feieresen, J. M., Montgomery, M. D., and Fleeter, S., 1993, *“Unsteady Aerodynamic Forcing Functions: A Comparison Between Linear Theory and Experiment”*, ASME Paper 93-GT-141.

[27] Feireisen, J., and Fleeter, S., 1994, *“Low Solidity Vane Unsteady Aerodynamic Response to Combined Vortical-Potential Forcing Functions”*, AIAA Paper 94-2974.

[28] Fleeter, S., Novick, A. S., Riffel, R. E., and Caruthers, J. E., 1976, *“An Experimental Determination of the Unsteady Aerodynamics in a Controlled Oscillating Cascade”*, ASME Paper 76-GT-17.

[29] Fleeter, S., 1979, *“Trailing Edge Conditions for Unsteady Flows at High Reduced Frequency”*, AIAA Paper No. 70-0152.

[30] Försching, H. W., 1974, *“Grundlagen der Aeroelastik”*, Springer-Verlag, Berlin, Germany, ISBN 3-540-06540-7.

[31] Fransson, T. H., and Verdon, J. M., 1993, *“Panel Discussion on Standard Configurations for Unsteady Flow Through Vibrating Axial-Flow Turbomachine Cascades”*, Unsteady Aerodynamics, Aeroacoustics, and Aeroelasticity of Turbomachines and Propellers, H. M., Atassi, ed., Springer-Verlag, New York, pp. 859-889.

[32] Fransson, T. H., Jöcker, M., Bölcs, A., and Ott, P., 1998, *“Viscous and Inviscid Linear/Nonlinear Calculations Versus Quasi 3D Experimental Cascade Data for a New Aeroelastic Turbine Standard Configuration”*, ASME Paper 98-GT-490.

[33] Fung, Y. C., 1969, *“An Introduction to the Theory of Aeroelasticity”*, Dover Publications, Inc., New York, USA, Second Edition (First Edition 1955), ISBN 486-62433-1.

[34] Giles, M. B., 1988, *“Calculation of Unsteady Wake Rotor Interaction”*, AIAA Journal of Propulsion and Power, Vol. 4, No. 4, pp. 356-362.

[35] Giles, M. B., 1991, Unpublished Communication with Manwaring and Wisler.

[36] Grüber, B., and Carstens, V., 1996, *“Computation of the Unsteady Transonic Flow In Harmonically Oscillating Turbine Cascades Taking Into Account Viscous Effects”*, ASME Paper 96-GT-338.

[37] Jay, R. L., and Fleeter, S., 1987, *“Unsteady Aerodynamic Measurements in Forced Vibration Research”* in the AGARD Manual on Aeroelasticity in Axial-Flow Turbomachines, Vol. 1, Unsteady Turbomachinery Aerodynamics, AGARD-AG-298, pp. 9-1 to 9-38.

[38] Ji, S., and Liu, F., 1997, *“Computations of Unsteady Flows Around Oscillating Blades and Aeroelasticity Behavior”*, 35th Aerospace Sciences Meeting and Exhibit, AIAA-97-0161, Jan. 6-10.

[39] Hall, K. C., and Crawley, E. F., 1989, *“Calculation of Unsteady Flows in Turbomachinery Using the Linearized Euler Equations”*, AIAA Journal, Vol. 27, No. 6, pp. 777-787, June.

[40] Hall, K. C., and Lorence, C. B., 1993, *“Calculation of Three-Dimensional Unsteady Flows in Turbomachinery Using the Linearized Harmonic Euler Equations”*, ASME Journal of Turbomachinery, Vol. 115, pp. 800-809, October.

[41] He, L., 1990, *“An Euler Solution for Unsteady Flows Around Oscillating Blades”*, ASME Journal of Turbomachinery, Vol. 112, pp. 714-722.

[42] He, L., and Denton, J. D., 1994, *“Three-Dimensional Time Marching Inviscid and Viscous Solutions for Unsteady Flows Around Vibrating Blades”*, Transactions of the ASME, Journal of Turbomachinery, Vol. 116, No. 3, pp. 469-476, July.

[43] Henderson, G. H., and Fleeter, S., 1992, *“Forcing Functions Effects on Unsteady Aerodynamic Gust response Part 1: Forcing Functions”*, ASME Paper 92-GT-174.

[44] Holmes, D. G., and Chuang, H. A., 1993, *“2D Linearized Harmonic Euler Flow Analysis for Flutter and Forced Response”*, in “Unsteady Aerodynamics, Aeroacoustics, and Aeroelasticity of Turbomachines and Propellers”, H. M. Atassi, ed., Springer-Verlag, New York.

[45] Holmes, D. G., Mitchell, B. E., and Lorence, C. B., 1997, *“Three-Dimensional Linearized Navier-Stokes Calculations for Flutter and Forced Response”*, in “Unsteady Aerodynamics and Aeroelasticity of Turbomachines: Proceedings of the 8th International Symposium held in Stockholm, Sweden, 14-18 September 1997", Torsten H. Fransson, ed., Kluwer Academic Publishers, Dordrecht, The Netherlands, ISBN 0-7923-5040-5.

[46] Kahl, G., 2002, *“Aeroelastic Effects of Mistuning and Coupling in Turbomachinery Bladings”*, Communication du Laboratoire de Thermique Appliquée et de Turbomachines de l'Ecole Polytechnique Fédérale de Lausanne, No. 36.

[47] Kay S. M., 1988, *“Modern Spectral Estimation”*, Prentice-Hall, ISBN 0-13-598582-X.

[48] Kielb, R. E., 1997, *“Introduction to Aeroelastic Blade Design”*, A Three Day Intensive Course during the 8th International Symposium on Unsteady Aerodynamics and Aeroelasticity in Turbomachines, Stockholm, Sweden, September 11-13.

[49] Kim-Frey, K., 1996, *“Combined/Simultaneous Gust and Oscillating Blade Unsteady Aerodynamics”*, Ph.D. Dissertation, Purdue University.

[50] Kim-Frey, K., and Fleeter, S., 1999, *“Combined-Simultaneous Gust and Oscillating Compressor Blade Unsteady Aerodynamics”*, ASME Paper 99-GT-414.

[51] Körbächer, H., and Bölcs, A., 1994, *“Experimental Investigation of the Unsteady Behavior of a Compressor Cascade in an Annular Ring Channel”*, Paper presented at the 7th ISUAAT Conference in Fukuoka, Japan, September.

[52] Koughan, J., 1996, *“The Collapse of the Tacoma Narrows Bridge, Evaluation of Competing Theories of its Demise, and the Effects of the Disaster of Succeeding Bridge Designs”*, http://www.firebirdz.net/tnb/failure/failure-temp.htm.

[53] Lane F., 1956, *“System Mode Shapes in the Flutter of Compressor Blade Row”*, Journal of the Aeronautical Sciences, Vol. 23, No. 1, pp. 54-66.

[54] Laumert, B., Martensson, H., Fransson, T. H., 2002, *“Investigation of Unsteady Aerodynamic Blade Excitation Mechanisms in a Transonic Turbine Stage-Part I: Phenomenological Identification and Classification”*, Journal of Turbomachinery, Vol. 124, pp. 410-418.

[55] Laumert, B., Martensson, H., Fransson, T. H., 2002, *“Investigation of Unsteady Aerodynamic Blade Excitation Mechanisms in a Transonic Turbine Stage-Part II: Analytical Description and Quantification”*, Journal of Turbomachinery, Vol. 124, pp. 419-428.

[56] Lehr, A., 1996, *“Preliminary Design Calculations for the Prediction of the Aerodynamic Parameters in the RGP Test Facility with the Program UNSTREST 13”*, Internal Report, LTT-96-28.

[57] Manwaring, S. R., and Wisler, D. C., 1992, *“Unsteady Aerodynamics and Gust Response in Compressors and Turbines”* ASME Paper 92-GT-422.

[58] Manwaring, S. R., Rabe, D. C., Lorence, C. B., and Wadia, A. R., 1996, *“Inlet Distortion Generated Forced Response of a Low Aspect Ratio Transonic Fan”*, ASME Paper 96-GT-376.

[59] Ni, R. H., and Sisto, F., 1976, *“Numerical Computation of Nonstationary Aerodynamics of Flat Plate Cascades in Compressible Flow”*, ASME Journal of Engineering for Power, pp. 165-170, April.

[60] Nowinski, M., 1999, *“Experimental Investigation of an Oscillating Airfoil in the Presence of Downstream Generated Gusts”*, Communication du Laboratoire de Thermique Appliquée et de Turbomachines de l'Ecole Polytechnique Fédérale de Lausanne, No. 30.

[61] O'Brien, W. F., Cousins, W. T., and Sexton, M. R., 1980, *“Unsteady Pressure Measurements and Data Analysis Techniques in Axial-Flow Compressors”*, ASME Joint Fluids Engineering and Gas Turbine Conference, New Orleans, pp. 195-202.

[62] Oppenheim, A. V., Schafer, R. W., Buck, J. R., 1999, *“Discrete-Time Signal Processing”*, Prentice-Hall, ISBN 0-13-083443-2.

[63] Ostdiek, F. R., 1976, *“A Cascade in Unsteady Flow”*, AFAPL-TR-76-115.

[64] Ott, P., 1992, *“Oszillierender Senkrechter Verdichtungsstoss In Einer Ebenen Düse”*, Communication du Laboratoire de Thermique Appliquée et de Turbomachines de l'Ecole Polytechnique Fédérale de Lausanne, No. 18.

[65] Panovsky, J., Nowinski, M., and Bölcs, A., 1997, *“Flutter of Aircraft Engine Low Pressure Turbine Blades: Oscillating Cascade Experiments and Analysis”*, in “Unsteady Aerodynamics and Aeroelasticity of Turbomachines: Proceedings of the 8th International Symposium held in Stockholm, Sweden, 14-18 September 1997”, Torsten H. Fransson, ed., Kluwer Academic Publishers, Dordrecht, The Netherlands, ISBN 0-7923-5040-5.

[66] Panovsky, J., Carson, S., M., 1998, *“Prediction of Turbine Blade Vibratory Response Due to Upstream Vane Distress”*, Journal of Turbomachinery, Vol. 120, pp. 515-521.

[67] Platzer, M. F., and Carta, F. O., 1987, *“AGARD Manual on Aeroelasticity in Axial-Flow Turbomachines”*, Vol. 1, Unsteady Turbomachinery Aerodynamics, AGARD-AG-298.

[68] Platzer, M. F., and Carta, F. O., 1988, *“AGARD Manual on Aeroelasticity in Axial-Flow Turbomachines”*, Vol. 2, Structural Dynamics and Aeroelasticity, AGARD-AG-298.

[69] Poensgen, C. A., and Gallus, H. E., 1991, *“Experimental Investigation on the Unsteady Pressure Field on a Vibrating Cascade in Unsteady Flow”*, presented at Unsteady Aerodynamics of Turbomachines and Propellers, University of Notre Dame, Indiana, September 15-19, pp. 583-601.

[70] Rottmeier, F. A., Muellhaupt, Ph., Bölcs, A., 2002, *“Precise & Rapid Unsteady Pressure Transducer Signal Processing using a Transfer Function Modeling Technique”*, presented at The 16th Symposium on Measuring Techniques in Transonic and Supersonic Flow in Cascades and Turbomachines, Cambridge, UK, september 23 & 24, 2002.

[71] Sisto, F., 1995, *“Aeroelasticity in Turbomachines”*, Chapter 8 in A Modern Course in Aeroelasticity, E. H. Dowell, ed., Kluwer Academic Publishers, The Netherlands, ISBN 0-7923-2789-6.

[72] Smith, S.N., 1972, *“Discrete Frequency and Sound Generation in Axial Flow Turbomachines”*, ARC Reports and Memoranda, No. 3709.

[73] Sturm, W., Fottner, L., 1985, *“The High-Speed Cascade of the German Armed Forces University Munich”*, 8th Symposium on Measuring Techniques for Transonic and Supersonic Flows in Cascades and Turbomachines, Genoa.

[74] Széchényi, E., and Girault, J. P., 1980, *“Aeroelastic Testing in a Straight Cascade Wind Tunnel”*, Proceedings of the Symposium “Aeroelasticity in Turbomachines”, Lausanne, Switzerland, pp. 143-149.

[75] Verdon, J. M., and Caspar, J. R., 1984, *“A Linearized Unsteady Aerodynamic Analysis for Transonic Cascades”*, Journal of Fluid Mechanics, Vol. 149, pp. 403-429.

[76] Verdon, J. M., 1987, *“Linearized Unsteady Aerodynamic Theory”*, in the AGARD Manual on Aeroelasticity in Axial-Flow Turbomachines, Vol. 1, Unsteady Turbomachinery Aerodynamics,” AGARD-AG-298, pp. 2-1 to 2-31.

[77] Verdon, J. M., 1989, *“Unsteady Aerodynamics for Turbomachinery Aeroelastic Applications”*, Chapter 7 in Unsteady Transonic Aerodynamics, D. Nixon, ed., The American Institute of Aeronautics and Astronautics, Inc., Washington, D.C., USA, ISBN 0-930403-52-5.

[78] Weaver, M., and Fleeter, S., 1994, *“Turbine Rotor Generated Forcing Functions For Flow Induced Vibrations”*, ASME Paper 94-GT-328.

[79] Whitehead, D. S., 1982, *“The Calculation of Steady and Unsteady Transonic Flow in Cascades”*, Cambridge University Engineering Department Report CUED/A-Turbo/TR 118.

[80] Whitehead, D. S., 1987, *“Classical Two-Dimensional Methods”*, in the AGARD Manual on Aeroelasticity in Axial-Flow Turbomachines, Vol. 1, Unsteady Turbomachinery Aerodynamics, AGARD-AG-298, pp. 3-1 to 2-30.

APPENDIX A

Precise & Rapid Unsteady Pressure Transducer Signal Processing Using a Transfer Modeling Technique

This paper was presented at the *"16th Symposium on Measuring Techniques in Transonic and Supersonic Flow in Cascades and Turbomachines"* in Cambridge, UK, on September 23rd 2002. It was written in collaboration with Dr. Phillipe Muellhaupt from the Automation Laboratory of the Swiss Federal Institute of Technology in Lausanne (EPFL).

PRECISE & RAPID UNSTEADY PRESSURE TRANSDUCER SIGNAL PROCESSING USING A TRANSFER FUNCTION MODELING TECHNIQUE

Rottmeier F.
Tel: + 41 21 693 73 23
Fabrice.Rottmeier@epfl.ch
Fax: + 41 21 693 35 02
LTT-ISE-STI, EPFL

Mullhaupt Ph.
Tel: + 41 21 693 38 38
Philippe.Muellhaupt@epfl.ch
Fax: + 41 21 693 25 74
LA-I2S-STI, EPFL

Swiss Federal Institute of Technology
CH-1015 Lausanne
Switzerland

ABSTRACT

The authors have applied a transfer function modeling technique to the calibration of unsteady pressure transducers used for unsteady flow measurements in turbomachinery. This modeling technique has shown to be faster and more precise than previously used curve fitting techniques. In this article, the authors present the theory applied for this identification and give an explicit example of its application and advantages.

INTRODUCTION

Transfer Functions have been used since the beginning of the 19th century to model various systems for stability analysis, prediction, simulation and control purposes. Applied first to mechanical systems, it is now a common modeling technique used in numerous fields such as electronics, chemistry, economics, and neural networks.

Unsteady pressure measurements in turbomachinery are commonly conducted with the use of unsteady pressure transducers. The signals delivered by these piezo-resistive sensors require amplification to meet the range of the data acquisition devices. In order to do so, analog electronic amplifiers are mostly used. Often combined with other signal conditioning features such as filtering (notch, low-pass), the effect of this electronic conditioning on the input signal varies in the frequency domain. In order to reconstruct precisely the true pressure signal from the acquired signal, an accurate description of the transducer's signal amplification chain is necessary.

This identification can be conducted by feeding a generated sine sweep signal, with the desired bandwidth and amplitude into the electronic amplification system and measuring the frequency response of the output with a dynamic signal analyzer (Periodic Chirp Response Measurement).

Traditional techniques used to account for the effect of the amplifiers on the source signal consist of extracting the main harmonics (harmonic signal analysis) and getting the corrections corresponding to these discrete frequencies by interpolation on the Periodic Chirp Response results (amplitude and phase versus frequency).

As part of the Brite-Euram "Aeromechanical Design of Turbine Blades" project (ADTurB I), unsteady blade surface measurements were conducted on an axial turbine cascade in the Non-Rotating Annular Test Facility of the "Laboratoire de Thermique Appliquée et de Turbomachines" (LTT) of the Swiss Federal Institute of Technology in Lausanne (EPFL). Two main sources of unsteady pressures in turbomachinery were studied separately and then in combination for different configurations and flow conditions:

(1) The influence of blade motion (Controlled Vibration Measurements).
(2) The influence of upstream generated gusts (Gust Response Measurements)

NOMENCLATURE

DAQ	Data Acquisition
TF	Transfer Function
a,b,c,d,e,f	complex parameters
$\tilde{a},\tilde{b},\tilde{c},\tilde{d},\tilde{e},\tilde{f}$	complex parameters
f	frequency
$G(s)$	transfer function
$g(t)$	impulse response
i	index
j	$j=\sqrt{-1}$
$\mathcal{L}$	Laplace transform
n	number of samples
s	complex variable
$u(t)$	input time signal
$\mathbf{R}$	regression matrix
U	input (frequency domain)
$\mathbf{U}$	input Vector
v	degree of TF numerator
w	degree of TF denominator
$y(t)$	output time signal
Y	output (frequency domain)
$\hat{Y}$	output estimator
$\mathbf{Y}$	output vector
$\hat{\mathbf{Y}}$	output estimator vector
ε	absolute error vector
ϑ	parameter vector
ϑ^*	optimal parameter vector
ω	pulsation
$*$	convolution

SYSTEM IDENTIFICATION

Both aerodynamic excitation sources presented in the introduction were tested with a common excitation frequency of 276 [Hz]. Traditional testing of (1) yields in most cases sinusoidal pressure fluctuations requiring only the characterization of the unsteady pressure transducer's amplification chain around a single frequency. On the other hand, the newly installed gust generator consisting of rotating elliptical struts involve four to seven harmonics requiring the same identification for a bandwidth of 250 to 2500 [Hz].

This characterization has been conducted using a 10 [mV] sine sweep input signal generated by a HP35660A dynamic signal analyzer. The frequency response of the system consists of 400 samples from 75 to 3275 [Hz] (every 8 [Hz]) and is represented in figure 1. The effect of the 4 [kHz] low-pass filter is clearly visible and shows the need for a precise identification of the system, especially if one considers the importance of the phase lag introduced over the whole measured bandwidth.

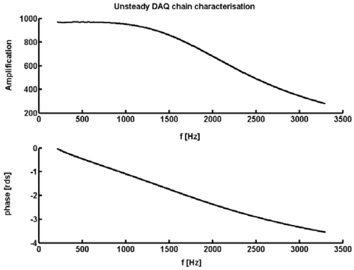

Figure 1 Unsteady DAQ chain characterization

TRANSFER FUNCTION MODELING

Let us consider the unsteady pressure transducer DAQ chain has a single input, *u(t)*, single output, *y(t)*, system. If we suppose small excitations around a nominal frequency (linear system hypothesis) we can write the output *y(t)* as a function of the input signal *u(t)* and of the impulse response *g(t)* as:

$$y(t) = g(t) * u(t) = \int u(t)\cdot g(t-\tau)\,d\tau \qquad \textbf{(1)}$$

Taking the Laplace Transform of (1) will allow a considerable simplification of the mathematical operations:

$$\mathcal{L}\left[y(t)\right] = \mathcal{L}\left[u(t)\right]\cdot\mathcal{L}\left[g(t)\right] \qquad \textbf{(2)}$$

Where $G(s)=\mathcal{L}\left[g(t)\right]$ is known as the transfer function of the system. (2) becomes:

$$Y(s)=U(s)\cdot G(s) \quad \Rightarrow \quad G(s)=\frac{Y(s)}{U(s)} \qquad \textbf{(3)}$$

G(s) is always a rational fraction in s where the degree of the denominator w is greater than the degree of the numerator v in order to have a causal transfer function. Several combinations of v and w have been tested starting with low values. The first qualitatively representative combination of v and w are values of 2 and 3 respectively, giving the following model:

$$G(s)=\frac{\tilde{a}s^2+\tilde{b}s+\tilde{c}}{s^3+\tilde{d}s^2+\tilde{e}s+\tilde{f}} \qquad \textbf{(4)}$$

Where $\tilde{a}, \tilde{b}, \tilde{c}, \tilde{d}, \tilde{e}$ and $\tilde{f}$ are the complex parameters of *G(s)* to be determined.

If we consider only harmonic inputs and neglect the transient behavior of the system (i.e.: after the transient response has damped out) then the harmonic response is sufficient for this study. We can therefore replace s by $j\omega$ in (4), where $\omega = 2\pi f$ is a given pulsation and f the corresponding frequency:

$$G(j\omega) = \frac{\tilde{a}(j\omega)^2 + \tilde{b}(j\omega) + \tilde{c}}{(j\omega)^3 + \tilde{d}(j\omega)^2 + \tilde{e}(j\omega) + \tilde{f}} \qquad \textbf{(5)}$$

To avoid numerical instability due to large pulsation values ω, (5) can be rewritten as:

$$G(j\omega_i) = \frac{\tilde{a} + \dfrac{\tilde{b}}{j\omega} + \dfrac{\tilde{c}}{(j\omega)^2}}{j\omega + \tilde{d} + \dfrac{\tilde{e}}{j\omega} + \dfrac{\tilde{f}}{(j\omega)^2}} \qquad \textbf{(6)}$$

Defining the new complex parameters *a, b, c, d* and f by dividing the numerator and the denominator by $\tilde{d}$ yields the final form of the model to be used:

$$G(j\omega) = \frac{a + \dfrac{b}{j\omega} + \dfrac{c}{(j\omega)^2}}{1 + d \cdot j\omega + \dfrac{e}{j\omega} + \dfrac{f}{(j\omega)^2}} \qquad \textbf{(7)}$$

Where:

$$\begin{aligned} a &= \frac{\tilde{a}}{\tilde{d}}; \quad b = \frac{\tilde{b}}{\tilde{d}}; \quad c = \frac{\tilde{c}}{\tilde{d}}; \\ d &= \frac{1}{\tilde{d}}; \quad e = \frac{\tilde{e}}{\tilde{d}}; \quad f = \frac{\tilde{f}}{\tilde{d}} \end{aligned} \qquad \textbf{(8)}$$

The parameters appear linearly in the input-output relationship. Only the coefficients vary nonlinearly with respect to the frequency (i.e. it is a linear combination of non-linear functions). Let us proceed with the following regrouping:

Using equation (3), (7) becomes:

$$\begin{aligned} Y(j\omega) &= -d \cdot (j\omega) \cdot Y(j\omega) - \frac{e}{j\omega} \cdot Y(j\omega) \\ &- \frac{f}{(j\omega)^2} \cdot Y(j\omega) + a \cdot U(j\omega) + \\ &\frac{b}{j\omega} \cdot U(j\omega) + \frac{c}{(j\omega)^2} \cdot U(j\omega) \end{aligned} \qquad \textbf{(9)}$$

Let us introduce the estimated Y value based on this relationship:

$$\begin{aligned} \hat{Y}(j\omega) &= -d \cdot (j\omega) \cdot Y(j\omega) - \frac{e}{j\omega} \cdot Y(j\omega) \\ &- \frac{f}{(j\omega)^2} \cdot Y(j\omega) + a \cdot U(j\omega) + \\ &\frac{b}{j\omega} \cdot U(j\omega) + \frac{c}{(j\omega)^2} \cdot U(j\omega) \end{aligned} \qquad \textbf{(10)}$$

During the identification of the unsteady pressure transducer DAQ chain, we collected measured values for n different frequencies. Therefore we can gather all input and output signals in vectors:

$$\boldsymbol{Y} = \begin{bmatrix} Y(j\omega_1) \\ \vdots \\ Y(j\omega_i) \\ \vdots \\ Y(j\omega_n) \end{bmatrix} \qquad \boldsymbol{U} = \begin{bmatrix} U(j\omega_1) \\ \vdots \\ U(j\omega_i) \\ \vdots \\ U(j\omega_n) \end{bmatrix} \qquad \textbf{(11)}$$

Equation (10) can be rewritten for all samples using matrix algebra:

$$\hat{\boldsymbol{Y}} = \boldsymbol{R} \cdot \boldsymbol{\vartheta} \qquad \textbf{(12)}$$

Where $\boldsymbol{R}$ is the regression matrix and ϑ the vector of parameters defined as follows:

$$\begin{aligned} \boldsymbol{R} = \Bigg[\boldsymbol{U} \quad & \frac{\boldsymbol{U}}{j\omega_i} \quad \frac{\boldsymbol{U}}{(j\omega_i)^2} \quad \cdots \\ & \cdots \quad -\boldsymbol{Y} \cdot j\omega_i \quad -\frac{\boldsymbol{Y}}{j\omega_i} \quad -\frac{\boldsymbol{Y}}{(j\omega_i)^2} \Bigg] \end{aligned} \qquad \textbf{(13)}$$

$$\vartheta = \begin{bmatrix} a & b & c & d & e & f \end{bmatrix}^T \qquad \textbf{(14)}$$

It is clear that there exists a mismatch between the estimated values $\hat{\boldsymbol{Y}}$ and the measured ones $\boldsymbol{Y}$. A good model (i.e. good parameter vector ϑ) should reduce this mismatch as much as possible. Therefore let us introduce the optimal parameter vector ϑ^* based on a least square criterion and defined as:

$$\vartheta^* = \arg\min_{\vartheta} \left(\boldsymbol{Y} - \hat{\boldsymbol{Y}}(\vartheta)\right)^T \left(\boldsymbol{Y} - \hat{\boldsymbol{Y}}(\vartheta)\right) \quad \textbf{(15)}$$

The optimum is easily computed using (12), see (Kay 1988):

$$\vartheta^* = \left(\boldsymbol{R}^T \boldsymbol{R}\right)^{-1} \boldsymbol{R}^T \boldsymbol{Y} \quad \textbf{(16)}$$

The estimated values can be computed if $\boldsymbol{R}^T \boldsymbol{R}$ is invertible. The absolute error between the prediction model and the measured values can be written as:

$$\varepsilon = \left|\boldsymbol{Y} - \hat{\boldsymbol{Y}}\right| \quad \textbf{(17)}$$

For the example given in figure 1, the above explained technique applied to the model of (7) yields the following results using Matlab® 6.1:

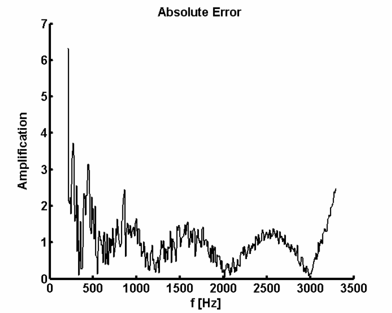

Figure 2 Absolute error of TF model in ‰

This error is based on a nominal amplification of 1000 and represents less than 0.3 % error on the desired bandwidth. Compared to previous methods based on polynomial curve fitting of figure 1 results, this technique and model order turns out to be five times more precise. Furthermore, the measured unsteady pressure signal can be corrected directly by multiplication with the inverse of the transfer function model allowing rapid corrections, especially if the signal's noise isn't filtered through harmonic signal analysis.

A further advantage of this modeling technique is that in similar conditions the same model can be used again and the parameters quickly computed using for example matrix algebra in Matlab®.

Difficulties may arise during the inversion of $\boldsymbol{R}^T \boldsymbol{R}$. In our example this matrix was close to singular (inversion may be inaccurate) but the parameters found produced the results of figure 2. In cases where $\boldsymbol{R}^T \boldsymbol{R}$ can not be inverted, it is possible to introduce a positive definite scaling matrix Σ in equation (15):

$$\vartheta^* = \arg\min_{\vartheta} \left(\boldsymbol{Y} - \hat{\boldsymbol{Y}}(\vartheta)\right)^T \Sigma \left(\boldsymbol{Y} - \hat{\boldsymbol{Y}}(\vartheta)\right) \quad \textbf{(17)}$$

(16) becomes:

$$\vartheta^* = \left(\boldsymbol{R}^T \Sigma \boldsymbol{R}\right)^{-1} \boldsymbol{R}^T \Sigma \boldsymbol{Y} \quad \textbf{(18)}$$

A judicious choice of the eigenvalues of Σ can enable the inversion of $\boldsymbol{R}^T \Sigma \boldsymbol{R}$, allowing the computation of the estimators.

Other difficulties may appear for low frequencies where the phase angles become negative. In this case, instabilities are produced probably due to the violation of the linearity assumption. This problem can be avoided by rejecting these low frequencies data samples.

CONCLUSIONS

The use of transfer functions for the modeling of commonly used unsteady pressure transducer amplification chain has been a success. It has been shown that this technique is faster and more precise than previously used methods and is particularly well suited for on-line corrections on digitized unsteady pressure signals.

REFERENCES

Kay S. M., 1988, *"Modern Spectral Estimation"*, Prentice Hall, ISBN 0-13-598582-X.

Nowinski, M., 1999, *"Experimental Investigation of an Oscillating Airfoil in the Presence of Downstream Generated Gusts"*, Communication du Laboratoire de Thermique Appliquée et de Turbomachines de l'EPFL, No. 30.

Oppenheim, A. V., Schafer, R. W., Buck, J. R., 1999, *"Discrete-Time Signal Processing"*, Prentice-Hall, ISBN 0-13-083443-2.

APPENDIX B

Aerodynamic Stability Analysis of EPFL’s “ADTurB” Cascade

This appendix summarizes the aerodynamic stability analysis of the EPFL “ADTurB” cascade in the first torsion mode and carried out during the Brite-Euram “Aeromechanical Design of Turbine Blades” project. This analysis consist of studying the aerodynamic damping and coupling features of the measuring cascade from controlled vibration experiments, in certain flow conditions. The first part gives an overview of the needed definitions. It is followed by the presentation of the local and global aerodynamic damping as a function of the cascade vibration mode for the subsonic test case. Examples of the application of the influence coefficient technique is presented to conclude this section.

Considering a two dimensional harmonic pitching movement of a rigid blade around a discrete torsion center C_t at a frequency of ω, the angular deflection $\alpha(t)$ can be written as:

$$\alpha(t) = \alpha \sin(\omega t) \tag{B.1}$$

The excitation effect of the time-dependent blade surface pressure distribution $\tilde{p}(s, t)$ on a pure pitching movement is reduced to the overall blade surface torque. This driving source is conventionally written as the non-dimensional unsteady moment coefficient $\tilde{c}_M(t)$ (per unit span):

$$\tilde{c}_M(t) = \frac{\int \{\vec{R} \otimes \tilde{p}(s, t)\vec{e}_p\} ds \bullet \vec{e}_j}{\alpha(p_{T1} - p_1)} \tag{B.2}$$

where, for a given curvilinear location s on the blade surface, $\vec{R}$ is the vector from the center of torsion C_t to s, $\vec{e}_p$ is the unit vector drawn in the direction of the pressure force (normal to the surface) and $\vec{e}_j$ the unit vector along the z-axis as schematically represented in Figure 93.

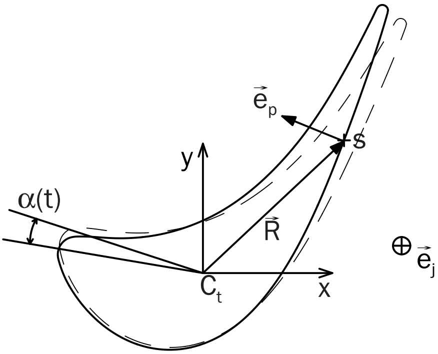

FIGURE 93. schematic representation of unsteady torque

The most important parameter for an aerodynamic stability analysis is the aerodynamic work. It can be shown that for the case of a single-degree-of-freedom torsion movement with the assumption of harmonic moment response, the aerodynamic work depends only on the out-of-phase component of the moment coefficient. This important parameter is commonly expressed in the normalized form as the aerodynamic damping coefficient Ξ, defined as, (see Carta [18]):

$$\Xi = -\mathrm{Im}[\tilde{c}_M(t)] = -\mathrm{Im}\left|\frac{\int\{\vec{R} \otimes \tilde{p}(s,t)\vec{e}_p\}ds \bullet \vec{e}_j}{\alpha(p_{T1} - p_1)}\right| \qquad \text{(B.3)}$$

The normalized aerodynamic damping coefficient Ξ is defined as positive if the flow damps the blade and negative if the flow tends to excite the blade. This parameter, that varies with the cascade’s vibration mode (IBPA), allows to determine the IBPA for which the aerodynamic damping is minimum, and therefore when the risk of flutter is maximum.

In order to investigate further the aerodynamic coupling effects, it is convenient to use the influence coefficient technique, which is based on the linear superposition principle of unsteady pressures. This principle states that the local blade surface unsteady pressure for a cascade vibrating in the travelling wave mode can be summed up linearly from influence coefficients obtained during single blade measurements:

$$\tilde{c}_p^{\,i} = \sum_{k=1}^{N} L_k^i \cdot \alpha_k \qquad \text{(B.4)}$$

where N is the total number of blades of the blade row, $\tilde{c}_p^{\,i}$ is the non-dimensional unsteady pressure coefficient at location i, α_k the harmonic movement of blade k and L_k^i the influence coefficient of the movement of blade k on the unsteady pressure coefficient at location i. $\tilde{c}_p^{\,i}$, α_k and L_k^i are all complex variables and commonly represented as amplitude and phase.The influence coefficients can be directly measured using single blade vibration experiments or computed from the series of linear equations (B.4) applied to the traveling wave mode measurements if, of course, the number of equations is at least equal to the number of unknown influence coefficients. Comparing influence coefficients from both methods allows the validation of the linear superposition principle of unsteady pressures.

Figure 94 and Figure 95 present the local aerodynamic damping results for the subsonic and the transonic test case, respectively. These plots correspond to the local aerodynamic work on the blade surface as a function of the cascade vibration mode (IBPA) presented separately for the pressure side and the suction side of the blade. Red regions correspond to an excitation effect of the flow on the blade vibration, as indicated by negative aerodynamic damping values. Similarly, blue regions show a local damping effect of the flow on the movement of the blade since Ξ is positive in these regions. As one can observe from these two figures, the main effect of outlet Mach number on the local aerodynamic damping is an augmentation of its range with increasing outlet velocity. In most cases for a given cascade vibration mode, damped and excited regions co-exist on the blade surface.

Integrating the local aerodynamic damping over the blade surface allows to study the global balance between locally excited or damped regions. The overall aerodynamic damping is the ultimate indicator of the aerodynamic stability analysis.

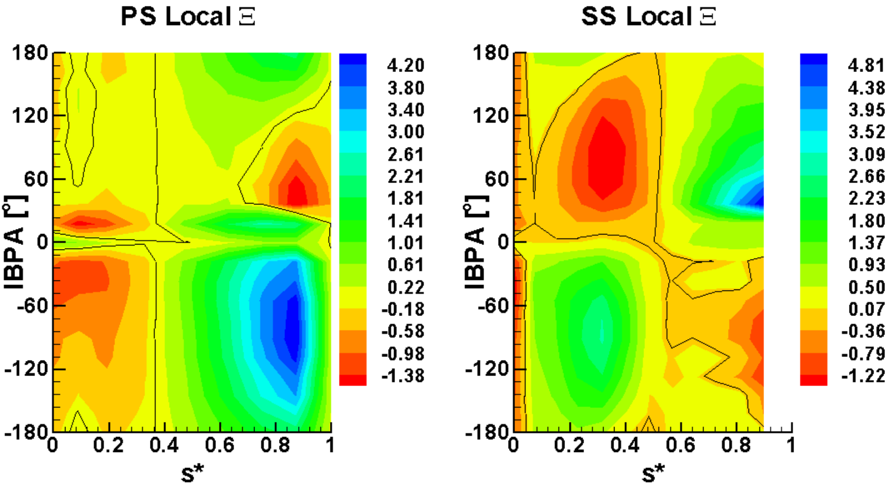

FIGURE 94. local aerodynamic damping, subsonic test case, torsion

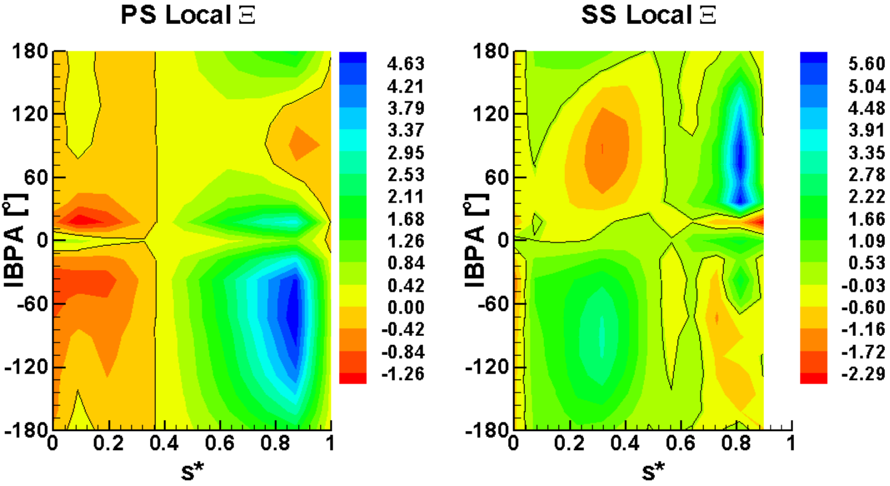

FIGURE 95. local aerodynamic damping, transonic test case, torsion

Figure 96 presents the overall aerodynamic damping results for the subsonic and transonic test cases for torsion. These curves, characterizing the aeroelastic properties of the cascade, indicate that for both cases and all IBPA the overall aerodynamic damping is always positive. In other words the cascade is aerodynamically stable in torsion. Both plots exhibit a sinusoidal shape with an additional drop around 0 [°] IBPA. The main difference between them is a rise in the overall aerodynamic damping range as observed previously with the local aerodynamic damping results of Figure 94 and Figure 95.

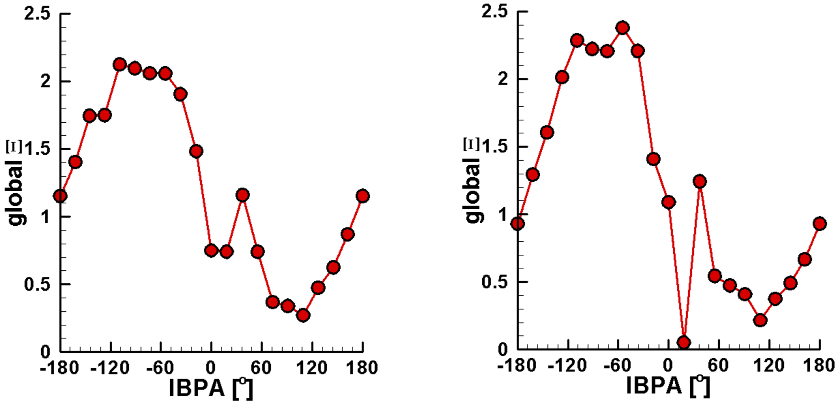

FIGURE 96. overall aerodynamic damping for torsion, (left: subsonic test case; right: transonic test case)

Both drops observed on the global aerodynamic damping around 0 to 18 [°] IBPA are attributed to an acoustic resonance phenomenon (see Smith [72]). The sinusoidal shape of the plots give an indication that the aerodynamic coupling effects involve only a limited number of neighboring blades. This is confirmed by using the influence coefficient technique described earlier in this section.

The influence coefficients obtained from single blade measurements and the ones computed from the travelling wave measurements can be compared locally. Examples of such comparisons for the subsonic test case are given for a pressure side location (PS 3) and a suction side location (SS 17) in Figure 97 and Figure 98, respectively. The first observation is that travelling wave mode measurements and single blade measurements yield extremely close results both on amplitude and phase. Therefore, the linear superposition principle holds and single blade measurements are sufficient to study the aerodynamic stability of the cascade in torsion. Blade number 5 and 6 correspond to the pressure side measuring blade and the suction side measuring blade, respectively. In Figure 97, one can observe that the main contribution of the unsteady pressure at location PS 03 is due to the movement of the blade on which the unsteady transducer sits and that the aerodynamic coupling at this location only involves a couple of neighboring blades with proportionally low contributions. In Figure 98, one can observe that the main contribution of the unsteady pressure at location SS 17 is due this time to the movement of the neighboring blade (on the same side as the captor) but that the movement of the blade on which the unsteady transducer sits contributes to a third in the measured unsteady pressures.

In general, for all measured locations, the aerodynamic influence coefficients show that only three to four neighboring blades contribute significantly to the aerodynamic coupling.

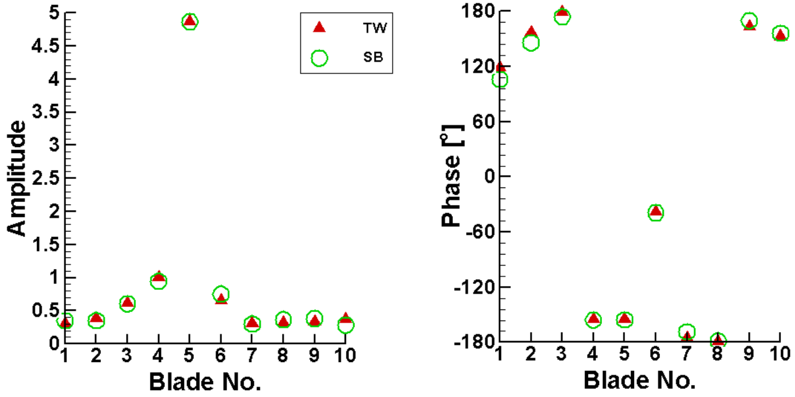

FIGURE 97. influence coefficients, transducer PS 3 (on blade 5), subsonic test case

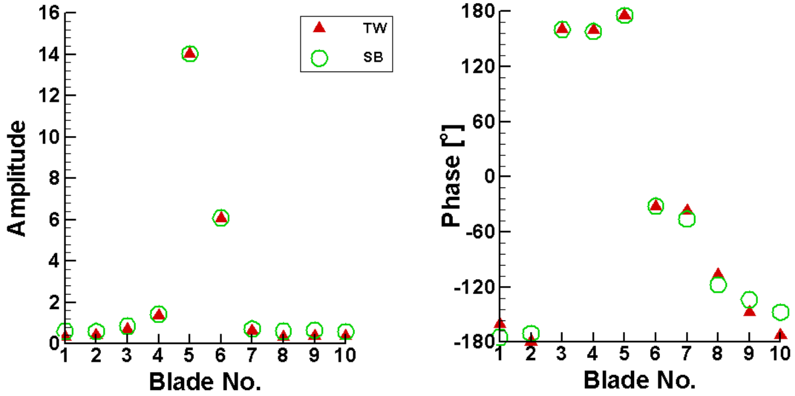

FIGURE 98. influence coefficients, transducer SS 17 (on blade 6), subsonic test case

APPENDIX C Unsteady Wake Measurements

This appendix presents the unsteady wake measurements conducted in collaboration with Prof. Roger Ainsworth of Oxford University using their in-house designed unsteady wedge probe (see Figure 16 on page 45). These measurements were conducted for the subsonic test case and an engine order of 22 with the same measuring technique and time resolution as for gust response measurements (see section 3.3 on page 51). The unsteady probe was placed at mid-channel height and at mid axial distance between the strut's TE and blade's LE. These measurements include the indexing of the measuring cascade at twenty-four equidistant positions over two blade passages in order to study the cascade's potential effect and verify the periodicity of the unsteady flow.

Figure 99 to Figure 102 present in the following order: the isentropic Mach, the relative flow angle, the total pressure and the static pressure as three-dimensional contour plots over two blade passages (36 [°]) and over one non-dimensional wake passing period. 1024 consecutive periods where acquired, with 64 samples per period, and averaged over the single period presented.

The total pressure results of Figure 101 exhibit quasi-constant level prior to the passage of the wake at t*=0.9. In fact a slight decrease in total pressure level can be seen as θ augments. This effect has been observed several times in the past on other long measurement series. It is believed that the air supply compressor has a very low frequency speed variation producing this total pressure drift of several millibars. As one would expect the total pressure drop, or losses, due to the wake is important. A slight potential effect of the cascade can be seen in the wake region but the periodicity isn't in good agreement. On the contrary, isentropic Mach number, relative flow angle and static pressure plots exhibit important potential effects of the cascade with excellent periodicity at every instant of time. For example, the relative flow angle between wakes (0<t*<0.75) varies like a sine wave with an amplitude of 10 [°]. The relative flow angle is augmented near the SS of the blade and diminished near the PS as one would expect from potential effects of the blade. The static pressure exhibit a similar variation of about 25 [mbars]. The cascade's potential effect and the wake seem to interact at t*=0.9 as shown by an amplification of the flow deviations in Figure 100 and an amplification of the static pressure variations in Figure 102. These observations could also be due to the presence of the probe and its interaction with the cascade's potential field for example. An unsteady flow visualization technique would be necessary to address this issue.

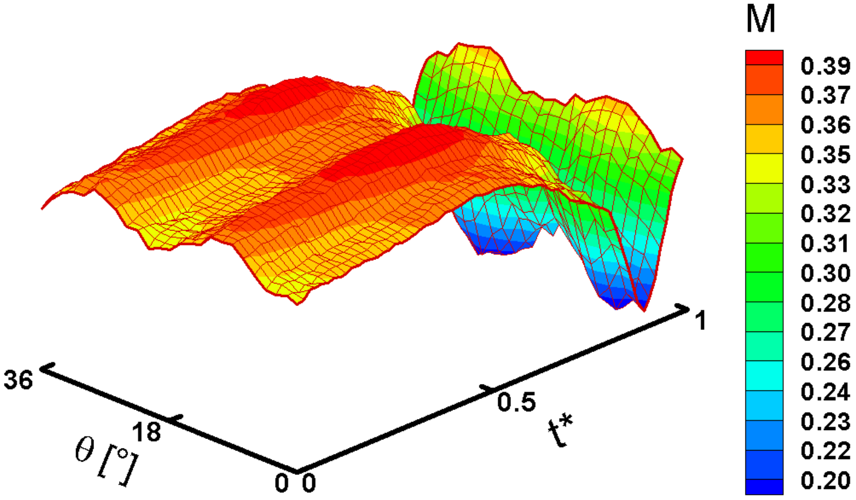

FIGURE 99. unsteady wedge probe measurements, mid-channel isentropic Mach versus cascade angular position, subsonic test case, EO 22, f=265 [Hz].

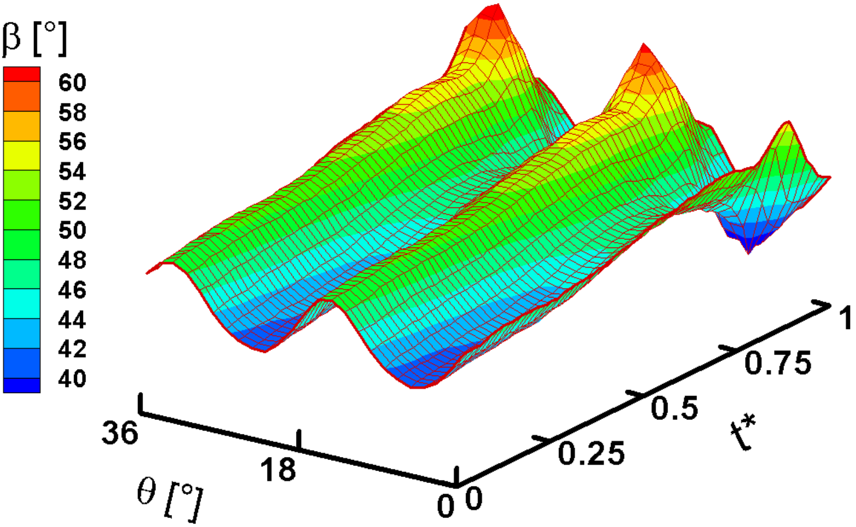

FIGURE 100. unsteady wedge probe measurements, mid-channel relative flow angle versus cascade angular position, subsonic test case, EO 22, f=265 [Hz].

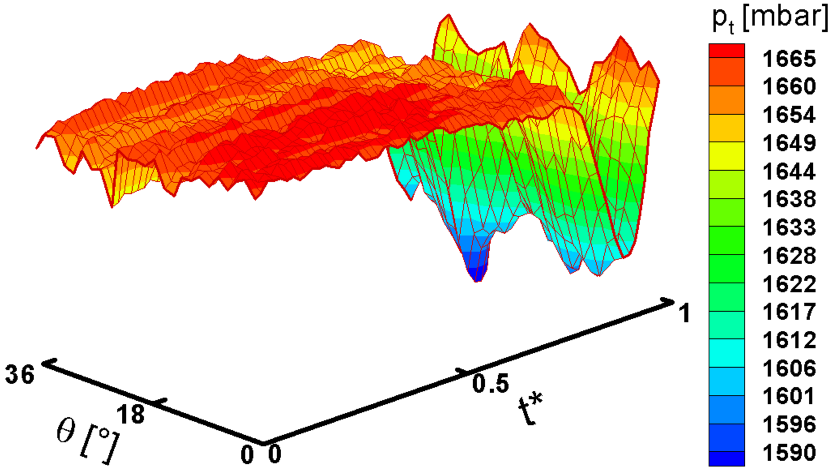

FIGURE 101. unsteady wedge probe measurements, mid-channel total pressure angle versus cascade angular position, subsonic test case, EO 22, f=265 [Hz].

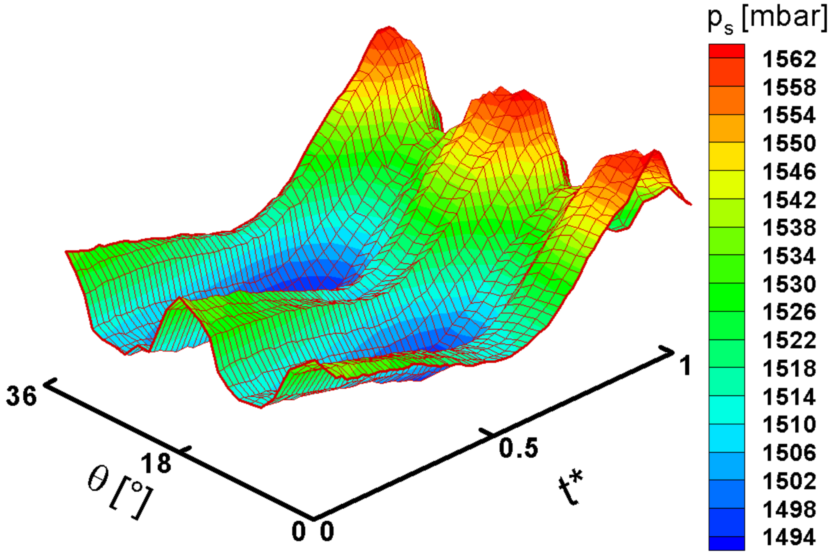

FIGURE 102. unsteady wedge probe measurements, mid-channel relative flow angle versus cascade angular position, subsonic test case, EO 22, f=265 [Hz].

Fabrice Rottmeier
Rue du Centre 52
CH – 1025 Saint-Sulpice

Home +41 (0)21 691 14 18
Mobile +41 (0)79 310 14 75
Email Fabrice@Rottmeier.ch

Born on October 5th 1968 in Pully, Vaud.
Swiss citizenship, maried with one child.

EXPERIENCE

1996 - present

Swiss Federal Institute of Technology-Lausanne (EPFL),
“Laboratoire de Thermique Appliquée et de Turbomachines” (LTT),
Mechanical Engineering Department: *Research Engineer*

Task leader for the Brite-Euram “ADTurB” European project at LTT (budget: 720 k€).

- Responsible for the upgrade of the non-rotating annular test facility:
  Design, fabrication, assembly, testing and integration of:
  - A turbine cascade with blade suspension systems and instrumentation.
  - A co-axial drive system with control and synchronization.
  - Aerodynamic probe-holders with position control.
- Managed and organized sub-contracted and in-house tasks:
  - In-house: machining, assembly, low & high voltage electrical installations.
  - Sub-contracted: co-axial drive design, electrical motors and command installation, special machining and processes (12 sub-contractors).
- Managed the work of a dozen technicians & engineers:
  (3 mechanics, 2 electricians, 2 electronics & 2 mechanical engineers...).
- Responsible for the “ADTurB” and “DLR” measurement campaigns at LTT.
- Biannually presented work progress and results to the European partners:
  (Alstom, Rolls-Royce (UK & D), SNECMA, Turbomeca, ITP, Fiat Avio, DLR, ONERA, Uni. of Oxford, KTH, Uni. of Limerick).

1994- 1995

EPFL, LTT, Mechanical Engineering Department: *Student*

Diploma project:

Performed tests to validate Rolls-Royce’s “UNSFLO” program for a Vibrating Compressor Cascade and wrote a user’s guide for this program.

Summer 1994

Georgia Tech Research Institute, Atlanta, USA: *Research Assistant*

Research in Numerical Aeroacoustics:

Programmed a Multi-Grid Generator with non-reflective boundary conditions.

1991 - 1992

Junior Enterprise: *Student*

Technical advisor for the Mechanical Engineering Department:

Supervised ME projects for local firms, managed project teams.

EDUCATION

2000 - present	EPFL, LTT Ph. D. on the fluid-structure interactions in axial turbomachinery (experimental approach), scheduled in March 2003.
1990 - 1995	EPFL Master's degree in Mechanical Engineering. *Areas of concentration:* Turbomachinery & Computational Fluid Dynamics.
1992 - 1993	Georgia Institute of Technology, Atlanta USA One year exchange program with the Aerospace Engineering School. *Honors:* Full Scholarship paid by EPFL; two quarters on the Dean's list.
1985 - 1988	Gymnase "CESSNOV" Baccalaureate type C (mathematics & science).

MILITARY

2001 - present	Swiss Air Force, Mission Control Chief, Payerne Air Force Base.
1990 - 2001	Swiss Air Force, Fighter Maintenance Platoon Leader, managed 35 people.

LANGUAGES

French	Native.
English	fluent, lived 4 years in the US.
Swiss-German	Good oral knowledge.
German	Functional knowledge.

COMPUTER SKILLS

- *Operating Systems:* DOS, Windows 95 to XP pro, & Unix.
- *Programming Skills:* Fortran 77, LabVIEW 6i, Matlab 6.0; Frontpage…
- *Software:* MS Office, Framemaker, Photoshop, Illustrator, Tecplot, IDEAS…

ACTIVITIES & HOBBIES

- Member of Saint-Sulpice municipal council.
- "Chez Les Copains" association, founding member.
  Association for the creation and the management of a child day care center.
- Swiss Air-Club, pilot.
- Ski instructor for teenagers and foreign students.
- "AMPA" association for the preservation of vintage aircraft, volunteer worker.

Sports	Badminton, mountain bike, jogging, telemark & traditional skiing
Other	Aviation, photography, traveling & fishing